



Assessment of the Hydrological Effect of Drought and Fire Events on Evapotranspiration at a Regional Scale

Melanie Häusler

SCIENTIFIC ADVISORS: Prof. José Miguel Oliveira Cardoso Pereira
PhD João Manuel das Neves Silva
PhD Thorsten Warneke

THESIS PRESENTED TO OBTAIN THE DOCTOR DEGREE IN
FORESTRY ENGINEERING AND NATURAL RESOURCES

2019

Assessment of the Hydrological Effect of Drought and Fire Events on Evapotranspiration at a Regional Scale

Melanie Häusler

SCIENTIFIC ADVISORS: Prof. José Miguel Oliveira Cardoso Pereira
PhD João Manuel das Neves Silva
PhD Thorsten Warneke

THESIS PRESENTED TO OBTAIN THE DOCTOR DEGREE IN
FORESTRY ENGINEERING AND NATURAL RESOURCES

JÚRI:

Presidente: Doutora Maria Teresa Marques Ferreira, Professora Catedrática
Instituto Superior de Agronomia, Universidade de Lisboa.

Vogais: Doutor Jorge Manuel Martins Soares David, Professor Catedrático
Instituto Superior de Agronomia, Universidade de Lisboa;
Doutor Thorsten Warneke, Senior Researcher
Institute of Environmental Physics, Universität Bremen, Alemanha;
Doutor Jan Jacob Keizer, Investigador Principal
Centro de Estudos do Ambiente e do Mar, Universidade de Aveiro;
Doutora Maria Teresa Gomes Afonso do Paço, Professora Auxiliar
Instituto Superior de Agronomia, Universidade de Lisboa;
Doutora Ana Paula Soares Marques de Carvalho, Professora Auxiliar
Instituto Superior de Agronomia, Universidade de Lisboa;
Doutora Teresa Maria Santana Barreto Soares David, Investigadora Auxiliar
Instituto Nacional de Investigação Agrária e Veterinária.

Instituições Financiadoras e âmbito:
Programa de doutoramento FCT (Sustainable Forests and Products, SUSFOR)
bolsa PD/BD/52698/2014

2019

Contents	i
Abstract	iii
Resumo	v
Resumo (estendido)	viii
Dedication	ix
Acknowledgements	xii
Citation	xiii
Contributions	xvi
Abbreviations	xvii
Symbols and variables	xxi
1 Introduction	1
1.1 Background: determination of evapotranspiration	1
1.2 Energy balance models and their concepts	2
1.3 Wildfires and their effect on the water cycle	4
1.4 Fire danger rating	5
2 Objectives and structure	7
3 Estimation and partitioning of actual daily evapotranspiration at an intensive olive grove using a simplified two-source energy balance model, (Article I)	9
4 Assessment of the indirect impact of wildfire (severity) on actual evapotranspiration in eucalyptus forest based on the surface energy balance estimated from remote sensing techniques, (Article II)	21
5 A promising new approach to estimate drought indices for fire danger assessment using remotely sensed data (Article III)	49
6 Conclusion	65
References	67

A	Model assessment over grassland	73
B	Influence of tree height	75
C	Estimation of the water stress coefficient of <i>E. globulus</i>	77
D	Classifier retrieval at the example of Indonesia	81

Abstract

Until today, there is only little knowledge about the behavior of actual evapotranspiration (ET_a) before and after wildfires in Portugal, which can be estimated from remote sensing techniques.

In this thesis, an existing Simplified Two-Source Energy Balance model (STSEB) was adapted, based on moderate resolution imagery to estimate ET_a and its contributing parts of transpiration and evaporation. The study served to test the model and its precision. A bias of about $\pm 1 \text{ mm d}^{-1}$ for the estimated ET_a was observed, where evaporation was regularly overestimated and transpiration underestimated. This error is acceptable for two-layer models based on satellite imagery, but estimates cannot be used for irrigation management.

The evolution of the estimated ET_a after wildfires (up to four years) was analyzed at eucalypt stands at the Caramulo mountain range in Portugal. By investigating the recovery of ET_a after wildfire, the difference between burnt and unburnt stands was mainly related to fire severity and stand characteristics. Two to three years after the fire events, the difference between burnt and unburnt stands became non-significant for all severity classes.

At the same region, the prediction of soil moisture deficit from drought indices was tested. The drought indices empirically estimate the dryness of an area and are directly related to fire danger. They are based on a simple water balance equation where effective rainfall and ET_a are the only input and output, respectively. In this work the empirical equation of (ET_a) was substituted by the estimated ET_a from STSEB, which enhanced the spatial resolution of the drought indices, being regularly interpolated from point estimates. Spatial patterns of soil moisture deficit were predicted, which indicated a relationship to fire occurrences.

To conclude, the ET_a estimated by the remote sensing based STSEB model, was used to make observations of the water cycle on a regional scale. In contrast to other post-fire studies, eucalypt stands in Portugal were found to be subject to a smaller hydrological impact after wildfires. This implies a fast recovery and a smaller influence on streamflow and groundwater resources. Furthermore, the drought indices, using the ET_a from STSEB, identified areas with higher proneness to drought, by improving the spatial resolution, using satellite imagery compared to traditional interpolation techniques. The results support fire danger rating and might help to improve fire regime and forest management.

Keywords: energy balance equation, evaporative fraction method, Normalized Burn Ratio, Keetch-Byram Drought Index, Drought Code

Resumo

O conhecimento sobre o comportamento da evapotranspiração real (ET_a), antes e depois dos incêndios florestais, especialmente pelo uso da detecção remota, é limitado.

No presente trabalho foi adaptado um modelo simplificado de equilíbrio de energia de duas fontes (STSEB), usando imagens de resolução moderada para estimar a ET_a e as suas componentes: transpiração e evaporação. O enviesamento da ET_a foi de $\pm 1 \text{ mm d}^{-1}$, onde a evaporação foi regularmente sobrestimada e a transpiração subestimada.

Foi observado o comportamento da ET_a estimada após incêndios florestais (até quatro anos depois), em eucaliptais da Serra do Caramulo, em Portugal. Investigando a recuperação da ET_a após um incêndio, a diferença observada entre áreas ardidas e não ardidas deveu-se principalmente a diferentes características da floresta e à severidade do fogo. Dois a três anos após o fogo, a diferença entre áreas ardidas e não ardidas tornou-se não significativa para todas as classes de severidade.

Além disso, foram testados índices de seca baseados num balanço hídrico simples, usando a ET_a estimada. Foram estimados padrões espaciais de défice de água no solo, que se relacionaram com a ocorrência de fogo.

Para concluir, o modelo STSEB permite estimar a ET_a a uma escala regional, e acompanhar o ciclo da água em áreas florestais usando técnicas da detecção remota. Em comparação com outros estudos dos efeitos do fogo, o impacto hidrológico após incêndios florestais em eucaliptal foi menor neste estudo. Isto revela uma recuperação rápida e um menor impacto nos recursos hídricos de superfície e subterrâneos. Além disso, o modelo STSEB, juntamente com os índices de seca, identificaram áreas com maior propensão à seca. Os resultados apoiam a cartografia de perigosidade de incêndio e podem ajudar a melhorar a gestão florestal.

Palavras chave: equação de balanço de energia, método da fração evaporativa, Normalized Burn Ratio, Keetch-Byram Drought Index, Drought Code

Resumo (estendido)

O conhecimento sobre o comportamento da evapotranspiração real (ET_a), antes e depois dos incêndios florestais, especialmente pelo uso da detecção remota, é limitado. Com as alterações climáticas e uma ocorrência crescente de desastres ambientais, nomeadamente incêndios florestais, torna-se necessário estudar a relação entre o balanço hídrico e ocorrência de secas e incêndios florestais, a uma escala regional.

Para atingir este objetivo, este estudo aplicou um modelo simplificado de balanço de energia de duas fontes (STSEB), usando imagens de resolução moderada (Landsat 5 e 8 com 30 m e MODerate-resolution Imaging Spectroradiometer, MODIS com 500 m de resolução espacial). Primeiramente, o modelo foi testado para estimar a ET_a e as suas componentes: transpiração e evaporação. Foram utilizados dados de campo (medições de fluxo de seiva e da evaporação com lisímetros), e método das flutuações instantâneas (eddy covariance, EC) num olival. O enviesamento da ET_a foi de $\pm 1 \text{ mm d}^{-1}$, onde a evaporação foi regularmente sobrestimada e a transpiração subestimada. A introdução no modelo da correcção dos factores beta levou uma melhoria das estimativas da ET_a .

Em segundo lugar, a recuperação da ET_a estimada após incêndios florestais (até quatro anos) foi observada, comparando povoamentos de eucalipto ardidos e não ardidos localizados na Serra do Caramulo, do centro-norte de Portugal. As áreas ardidas foram classificadas de acordo com a severidade do fogo, utilizando índice espectral Normalized Burn Ratio. A diferença absoluta de ET_a entre áreas ardidas e não ardidas foi usada para identificar mudanças provocadas pelo fogo e acompanhar a sua magnitude ao longo do tempo. Investigando a recuperação da ET_a após um incêndio, a diferença observada entre áreas ardidas e não ardidas deveu-se principalmente a diferentes características da floresta e à severidade do fogo. Logo após os incêndios, o solo contribuiu com cerca de 70% da densidade de fluxo de calor latente (LE , W m^{-2}) enquanto a vegetação apenas 30% de LE . Pelo contrário, em áreas não ardidas estes valores foram de 20% e 80% de LE , respectivamente. Dois a três anos após o fogo, a diferença entre florestas ardidas e não ardidas tornou-se não significativa para todas as classes de severidade do fogo (baixa, moderada, severa).

Em terceiro lugar, foi testada a previsão do défice de água no solo a partir de índices de seca na mesma área de estudo. De modo a estudar a influência da ET_a antes dos incêndios florestais, foram aplicados índices de seca usando a ET_a estimada pelo STSEB. Índices como o Drought Code (DC) ou o Índice de Seca Keetch-Byram (KBDI) baseiam-se numa versão simplificada da equação do balanço hídrico, em que a evapotranspiração é considerada como o único termo de perda. As equações empíricas incluem a evapotranspiração de referência (ET_o , na maioria dos estudos recentes ainda denominada evapotranspiração potencial, ET_p), a partir da qual a evapotranspiração foi estimada. Essas abordagens empíricas foram substituídas, no trabalho presente, pela ET_a estimada a partir do STSEB, produzindo também informação espacial sobre o conteúdo de água do solo e resultando em uma resolução espacial mais alta da cartografia de perigosidade de incêndio em comparação com as abordagens tradicionais

de interpolação. Foram estimados padrões espaciais de déficit de água no solo, que se relacionaram com a ocorrência de fogo. Foi encontrado um valor-limite, classificando as áreas como tendo menor ou maior propensão à seca, e relacionando-as com a ocorrência de incêndios florestais. Com o aumento das condições de seca, por ex. em julho, a classificação, usando o KBDI, permitiu identificar cerca de 75% dos incêndios que ocorreram na área de estudo numa área pré-definida. Desta área predefinida, 57% da área foi classificada como propensa ao fogo e incluiu 75% da área ardida.

Além disso, foram testadas e utilizadas duas abordagens diferentes de coeficientes para estimar a ET_a em dias em que as imagens de satélite não estão disponíveis: o coeficiente cultural ajustado ($K_{c,adj}$), que combina o efeito da transpiração da cultura, a evaporação do solo e o stresse hídrico; e o coeficiente cultural basal (K_{cb}), que representa apenas o efeito da transpiração da cultura. O valor do K_{cb} é igual ao da ET_a quando não há stresse hídrico e o efeito da evaporação do solo é nulo. Estes coeficientes foram usados para estimar continuamente o teor de água no solo através de índices de seca (por exemplo, KBDI e DC), para estimar a ET_a como producto da ET_o do dia com o coeficiente retirado da última imagem de satélite disponível, que entram seguidamente nas equações simplificadas de balanço hídrico. Este processo é repetido até à data em que estão disponíveis observações de satélite, que permitiam obter uma nova estimativa da ET_a a partir do STSEB e consequentemente novos coeficientes.

Esta investigação fornece uma compreensão das mudanças no balanço de energia e na ET_a , e das suas componentes numa região extensa de floresta no centro-norte de Portugal. Através da aplicação do modelo STSEB sobre as áreas afectadas pelo fogo, foi obtida uma boa concordância entre estimativas do modelo e os fluxos de balanço de energia medidos (densidade de fluxo de radiação líquida, R_n ; densidade de fluxo de calor sensível para o solo, G ; densidade de fluxo de calor sensível para a atmosfera, H ; e LE) e, consequentemente, da ET_a diária. Em comparação com outros estudos dos efeitos do fogo, o impacto hidrológico após incêndios florestais em eucaliptal foi menor neste estudo, e isso deveu-se à fraca severidade do fogo, já que a maioria deles foi classificada como fogo de gravidade baixa a moderada. Isto revela uma recuperação rápida e um menor impacto nos recursos hídricos de superfície e subterrâneos. Além disso, substituindo as estimativas da evapotranspiração nos índices de seca (KBDI e DC) pela estimativa de ET_a pelo modelo STSEB, áreas com maior propensão à seca foram identificadas, sendo fortemente relacionadas com a ocorrência de incêndios florestais. A melhor distinção destas áreas foi alcançada através da maior resolução espacial devida ao uso de imagens de satélite, pois os métodos convencionais ainda dependem da interpolação entre as estações meteorológicas. Além do mais, o modelo STSEB, juntamente com os índices de seca, permitiram a identificação de áreas com maior propensão à seca. Os resultados apoiam a cartografia de perigosidade de incêndio e podem ajudar a melhorar a gestão florestal. Num trabalho futuro, a aplicação dos índices de seca, KBDI e DC, em combinação com a ET_a do modelo STSEB, será testada para outras regiões, por ex. Indonésia, usando diferentes observações por satélite (por ex., Landsat, Sentinel). A este respeito a identificação de áreas com maior propensão ao fogo será melhorada usando abordagens de classificação mais sofisticadas.

Palavras chave: equação de balanço de energia, método da fração evaporativa, Normalized Burn Ratio, Keetch-Byram Drought Index, Drought Code

Dedication

This work is dedicated to my creator, life saver, supporter and faithful friend who should get all the credit of this work. Without him I would not have been able to become who I am today.

But blessed is the one who trusts in the LORD, whose confidence is in him. They will be like a tree planted by the water that sends out its roots by the stream. It does not fear when heat comes; its leaves are always green. It has no worries in a year of drought and never fails to bear fruit.

Jeremiah 17.7 and 8

Acknowledgements

My gratitude goes to:

Prof. José Miguel Cardoso Pereira, who despite his tight work schedule, always found a time slot to communicate or send data. I would also like to thank him for helping me with bureaucratic matters in addition to supervising my scientific work.

Dr. João N. Silva whom I am forever indebted for believing in me becoming a researcher and that all this can be done with a calm attitude. Thank you for being my adviser, my teacher, my colleague and also my friend. “Hakuna matata!”

Dr. Juan Sanchnéz, whom I will not be able to repay someday soon for the time, effort and patience he put in me to understand and use his “simplified two-source energy balance model”. He is the cornerstone of this work and I appreciate him as my role model being a professional, well-organized, and successful researcher, but also a kind and humbled human being to the ones who get to know him.

Prof. Dr. Isabel Ferreira who started guiding me from my master studies on and hopefully continues to be in my life till the end! I am in her debt in so many ways and thankful for always being there for me – professionally and personally – that it would be hard to start a list here. Let me tell you that Portugal and my memories connected to this country could not be so bright, sunny and lovely without her!

Dr. Thorsten Warneke who found me at the secretary’s office and really wanted to have me on board! Thank you for your support and the valuable time we spent talking about my research. I do hope that we will continue working together.

Dr. Nuno Conceição who taught me how hard a researchers life can be in the field. He is one of the hardest working and most dedicated persons I have ever met.

Dr. Gunnar Spreen, Prof. Dr. Georg Heygster and Prof. Dr. Justus Notholt who integrated me into their research group (PHAROS) during my stay at the Institute of Environmental Physics in Bremen. I am especially thankful to the regular group meetings where I could practice to talk and partly defend my research in front of other researchers.

Dr. Christian Melsheimer who read and corrected my work, discussed certain matters of my research and always contributed by either explaining certain issues or asking questions at the group meetings.

Dr. Jacob Keizer and Dr. João Nunes who provided valuable data sets, established professional connections, and offered personal guidance without this work could have never been originated.

André Garcia who started with me the Master programme and will finish with me the SUSFOR PhD programme. He was always there for me answering all my bureaucratic questions, when my Portuguese was not sufficient to understand certain procedures.

Dr. Paula Soares who also provided to me data sets and helped me getting connected to the people I needed for my research. She lectured me in forest fire management, but also was always there for a private chat.

Dr. Teresa Scholz my friend, who supported me at the end of the thesis to keep a good spirit and who gave me some valuable advice to put the finishing touch to the manuscript.

Dr. Andreas Häusler my dear husband without whom I could not have finished my thesis. He did not only spend time with the kids when I had to work, or bring them to school so I could start earlier working at the university, he also pushed me to learn new technologies. Without his help I would have never learnt how to use Latex or (even less likely) a program language such as Python. Thanks for bringing out the best of me!

My parents, Lorenz and Karin, who have never liked much my path but always supported me a 100% of their power. Even though they cannot follow why this was important to me, I thank them for their constant prayers and taking care of my financial welfare.

My children, Anna and Maryam, who always believe in me and see the best of me as a mother. Their simple view of life took me always back to reality and to the important things of our being. It makes me wonder what my children will remember as grown-ups, when I see Maryam playing the mother role and leaving me as “the grandmother” at home to stay with her kid (baby doll), so she can go to work. Love you babes!

Hermes, certamente, deixou escapar o ento da mão.
Porque, agora, parece o Diabo à solta, qual tufão, E todos
os presentes, com baldes de água, como loucos,
Acorríamos, desesperadamente, aos focos de incêndio,
Que punham em risco a aldeia e a população.

Estávamos nesta aflição, sem tempo para pensar na morte,
Quando se forma um remoinho de fogo puxado a vento
norte, Que atirou uns contra as paredes, e outros pela ar. E
aí, todos pensámos que era chegada a hora do Juízo Final!

Mas graças a São Pedro, o padroeiro, tal não aconteceu.
Porque esse remoinho gigante de fogo que se formou,
Não durou mais que meio minuto a passar por cima da
aldeia, E a atravessar a Ribeira e seguir a rota de
destruição e morte. E essa, não haja dúvida, foi na
verdade, a nossa sorte!

Porque se durava dois minutos, ficávamos ali, todos
assados, E havia mais mortes a lamentar, do incêndio de
Pedrogão Grande, como aconteceu, infelizmente, pouco
tempo depois, Quando essa frente do fogo apanhou os
fugitivos do Incêndio, Quatro quilómetros à frente, na
fatídica "estrada da morte!" Na má hora em que,
possivelmente, fugiam do incêndio Que se aproximava,
sem terem tempo de se refugiar Na Praia da Roca, na vila
de Castanheira de Pêra, O mais próximo e seguro lugar,
para a população se refugiar.

João de Deus Rodrigues, Mosteiro (Pedrogão Grande)
As Cinzas e a Esperança

Journal papers

1. **M. Häusler**, N. Conceição, L. Tezza, J. M. Sánchez, M. L. Campagnolo, A. J. Häusler, J. M. N. Silva, T. Warneke, G. Heygster, M. I. Ferreira. 2018. Estimation and partitioning of actual daily evapotranspiration at an intensive olive grove using the STSEB model based on remote sensing, *Agr. Wat. Managm.*. 201:188 - 198. DOI: 10.1016/j.agwat.2018.01.027
(2018 impact factor: 2.848, 5-year impact factor: 3.366)
 2. **M. Häusler**, J. P. Nunes, P. Soares, J. M. Sánchez, J. M. N. Silva, T. Warneke, J. J. Keizer, J. M. C. Pereira. 2018. Assessment of the indirect impact of wildfire (severity) on actual evapotranspiration in eucalyptus forest based on the surface energy balance estimated from remote sensing techniques, *Int. J. Rem. Sen.*
(2016 impact factor: 1.724)
 3. **M. Häusler**, J. P. Nunes, J. M. N. Silva, J. J. Keizer T. Warneke, J. M. C. Pereira. 2018. A promising new approach to estimate drought indices for fire danger assessment using remotely sensed data, *Agr. For. Meteorol.*
(2018 impact factor: 3.887, 5-year impact factor: 4.753)
- Other articles were published that are not included in the work, but for which significant contributions were made, during the time as PhD student.
4. N. Conceição, **M. Häusler**, S. Lourenço, C. Pacheco, L. Tezza, M. I. Ferreira. 2017. Three year of monitoring evapotranspiration components and crop and stress coefficients in a deficit irrigated intensive olive orchard, *Agr. Wat. Managm.*. 191:138 - 152. DOI: 10.1016/j.agwat.2017.05.011
 5. **M. Häusler**, J. M. N. Silva, S. Cerasoli, G. L. Saldaña, and J. M. C Pereira. 2016. Modelling spectral Reflectance of open Cork Oak Woodlands: A Simulation Analysis of the Effects of Vegetation Structure and Background, *Int. J. Rem. Sen.*. 37(03):492 - 515. DOI: 10.1080/01431161.2015.1134847

Conference Proceedings

The professional exchange and presentation of ongoing research was regularly conducted on various occasions.

1. **M. Häusler**, J. M. N. Silva, P. Soares, J. Keizer, T. Warneke, J. M. C. Pereira. *Using actual evapotranspiration to estimate fire danger from MODIS satellite imagery: a case study in a Eucalyptus stand* EGU, 08.-13. Apr. 2018, Vienna, Austria.
2. **M. Häusler**, J. M. N. Silva, P. Soares, J. M. Sánchez, J. P. Nunes, J. J. Keizer, M. A. Cerqueira, F. Goes, T. Warneke, and J. M. C. Pereira. *Impact on the energy balance fluxes and the surface variables after wildfires: A case study in Eucalyptus stands in Portugal, based on remote sensing* AGU Virtual Poster Showcase. October 2017, DOI 10.13140/RG.2.2.17189.81128
3. **M. Häusler**, J. M. N. Silva, P. Soares, J. M. Sánchez, J. P. Nunes, J. J. Keizer, M. A. Cerqueira, F. Goes, T. Warneke, and J. M. C. Pereira. *Changes of daily evapotranspiration after wildfires using a simplified two-source energy balance (STSEB) model based on remote sensing* Ciência 2017, Lisbon, Portugal. 3-5 Jul. 2017.
4. **M. Häusler**, N. Conceição, L. Tezza, J. M. Sánchez, J. M. N. Silva, J. M. C. Pereira, M. I. Ferreira. *Application of a two-source energy balance (TSEB) model from remote sensing to estimate daily actual evapotranspiration at an intensive olive grove* Ciência 2016, Lisbon, Portugal. 4-6 Jun. 2016.
5. **M. Häusler**, J. M. N. Silva, J. P. Nunes, P. Soares, J. M. Sánchez, T. Warneke, J. J. Keizer, J. M. C. Pereira. *Assessment of the hydrological effect of fire-induced vegetation changes on evapotranspiration at a regional scale* DPG Tagung, Mar. 2017, Bremen, Germany.

API	Antecedent Precipitation Index
CFFWI	Canadian Forest Fire Weather Index
CWSI	Crop Water Stress Index
DC	Drought Code
EC	Eddy Covariance
EVI	Enhanced Vegetation Index
FC	Field Capacity
FWI	Canadian Forest Fire Weather Index
IC	Internal Calibration
iTDVI	Temperature Dryness Vegetation Index
KBDI	Keetch-Byram Drought Index
LAI	Leaf Area Index
METRIC	Mapping EvapoTranspiration at high Resolution using Internalized Calibration
MODIS	MODerate-resolution Imaging Spectroradiometer
NDTI	Normalized Difference Temperature Index
NBR	Normalized Burn Ratio
PE	Percentage Error
PWP	Permanent Wilting Point
REBM	Resistance Energy Balance Model
RMSE	Root Means Square Error
SMAP	Soil Moisture Active Passive radiometer
SMOS	Soil Moisture Ocean Salinity product
SMD	Soil Moisture Deficit
STSEB	Simplified Two-Source Energy Balance model
TSEB	Two-Source Energy Balance model
UAV	Unmanned Aerial Vehicle
WDI	Water Deficit Index

Symbols and variables

α	Albedo, adim.
α_v	Albedo from canopy, adim.
α_s	Albedo from pure soil, adim.
γ	Psychrometric constant, kPa, °C
Δ	Vapour pressure curve slope, kPa, °C
ΔSM	Change of soil water content with time, mm d ⁻¹
ε	Surface emissivity, adim.
ε_s	Emissivity of the pure soil, adim.
ε_v	Emissivity of the vegetation, adim.
L_{atm}^{\uparrow}	Up-welling sky irradiance, W m ⁻² sr ⁻¹ μm ⁻¹
L_{atm}^{\downarrow}	Down-welling sky irradiance, W m ⁻² sr ⁻¹ μm ⁻¹
δQ	Change of soil water (soil water depletion in mm) during a certain time
ρ	Air density kg m ⁻³
θ_{FC}	Water content at field capacity, m ³ m ⁻³
θ_{WP}	Water content at wilting point, m ³ m ⁻³
τ	Transmissivity, adim.
C_G	Coefficient between 0.15–0.4 to obtain G from R_n
C_p	Volumetric heat capacity of air at constant pressure, J K ⁻¹ m ⁻³
DP	Deep percolation, mm d ⁻¹
e_a	Actual vapour pressure, kPa
e_s	Saturation vapour pressure, kPa
ET_a	Actual evapotranspiration for individual crops, mm d ⁻¹
ET_c	Crop evapotranspiration under standard conditions, mm d ⁻¹
ET_p	Daily potential evapotranspiration, mm d ⁻¹
ET_o	Daily reference evapotranspiration, mm d ⁻¹
ER	Effective rainfall that is the actual water reaching and infiltrating the soil depths without interception for drought code, mm d ⁻¹
G	soil heat flux density, W m ⁻²
G_d	daily soil heat flux density, W m ⁻² d ⁻¹
g_s	daily stomata resistance, cm s ⁻¹
H	Sensible heat flux density, W m ⁻²
H_d	Daily value of sensible heat flux density, W m ⁻² d ⁻¹
H_i	Instantaneous value of sensible heat flux density, W m ⁻²
H_s	Sensible heat flux density of the soil, W m ⁻²
H_v	Sensible heat flux density of the vegetation, W m ⁻²

I	Irrigation, mm d^{-1}
K_c	Crop coefficient, adim.
$K_{c,adj}$	Adjusted crop coefficient, adim.
K_{cb}	Basal crop coefficient, adim.
K_e	Soil evaporation coefficient, adim.
K_s	Water stress coefficient, adim.
LE	Latent heat flux density, W m^{-2}
LE_v	Latent heat flux density of the vegetation, W m^{-2}
LE_s	Latent heat flux density of the soil, W m^{-2}
LE_d	Daily value of latent heat flux density, $\text{W m}^{-2} \text{d}^{-1}$
LE_i	Instantaneous value of latent heat flux density, W m^{-2}
Lf	Seasonal correction factor for day length, adim.
L_{sen}	Top of atmospheric radiance, i.e. the radiance measured by the sensor
L_{sky}	Incident long-wave radiation, $\text{W m}^{-2} \text{sr}^{-1} \mu\text{m}^{-1}$
MAR	Mean annual rainfall, mm y^{-1}
$NDVI$	Normalized Difference Vegetation Index, adim.
$NDVI_s$	Normalized Difference Vegetation Index of the soil, adim.
$NDVI_v$	Normalized Difference Vegetation Index of the vegetation, adim.
NIR	Near infrared reflectance, nm
NIR_s	Surface reflectance from the near infrared band coming from the soil, nm
NIR_v	Surface reflectance from the near infrared band coming from the vegetation, nm
P_v	Partial vegetation, adim.
p	Average fraction of the total available water in the root zone, adim.
P_{eff}	Effective rainfall that is the actual water reaching and infiltrating the soil depths without interception, mm d^{-1}
P_{daily}	The daily measured rainfall in the open, mm d^{-1}
RAW	Readily available soil water in the root zone, mm
RED	Surface reflectance from the red band, nm
R_n	Net radiation, W m^{-2}
R_{nv}	Net radiation of the vegetation, W m^{-2}
R_{ns}	Net radiation of the soil, W m^{-2}
R_{nd}	Daily value of of net radiation, $\text{W m}^{-2} \text{d}^{-1}$
R_{ni}	Instantaneous value of net radiation, W m^{-2}
r_a	Aerodynamic resistance, m s^{-1}
r_a^a	Aerodynamic resistance to heat transfer between level of apparent sink of momentum and the reference height, m s^{-1}
r_a^h	Aerodynamic resistance to heat transfer between the canopy and the reference height, m s^{-1}
r_a^s	Aerodynamic resistance to heat flow in the boundary layer immediately above the soil surface, m s^{-1}
RED_s	Surface reflectance from the red band originating from the soil, nm
RED_v	Surface reflectance from the red band originating from the vegetation, nm
RP	Moisture equivalent after rain, % of dry soil
RO	Runoff, mm d^{-1}

S	Gobal solar radiation, kJ m^{-2} or $\text{MJ m}^{-2} \text{d}^{-1}$
SF	subsurface flow, mm d^{-1}
S_i	Initial threshold separating a value range into two groups
$SWIR$	Shortwave infrared reflectance, nm
T_a	Temperature of the air, $^{\circ}\text{C}$, or K
TAW	Total available soil water in the root zone, mm
T_{max}	Maximum daily air temperature, $^{\circ}\text{C}$, or K
T_{mean}	Mean daily air temperature, $^{\circ}\text{C}$, or K
T_{min}	Minimum daily air temperature, $^{\circ}\text{C}$, or K
Tr	Transpiration, mm d^{-1}
T_{rad}	Radiometric surface temperature, K
Tr_{max}	Maximum relative transpiration, mm d^{-1}
Tr_{rel}	Relative transpiration, mm d^{-1}
T_s	Temperature of the soil, $^{\circ}\text{C}$, or K
T_v	Temperature of the vegetation, $^{\circ}\text{C}$, or K
Z_r	Rooting depth, m

This work is the interface between forest hydrology and forest management, where a Two-Source Energy Balance (TSEB) model from hydrological science is applied to forestry. The thesis is organized in three parts presenting three different specific study purposes.

First, the simplified TSEB (STSEB, Sánchez et al., 2008b) was intensively tested for partitioning ET_a into its components (i.e. transpiration and evaporation), which until then had not been done in detail. For this purpose data from a long-term water use study at an olive grove were used. Then, the new found results, concerning the partitioning of ET_a were transferred to burnt eucalypt forests to investigate the changes in ET_a , transpiration and evaporation after fire events. Finally, the remotely estimated ET_a from STSEB was incorporated into fire danger indices to improve fire danger rating in forest stands, using a novel methodology developed for this work.

1.1 Background: determination of evapotranspiration

The estimation of actual evapotranspiration (ET_a , evaporated amount of water under non-standard conditions, Allen et al., 1998) is highly important to water managers and land users as it is directly related to crop productivity, and allows to optimize for irrigation strategies. There are many studies on water use in agriculture (Green et al., 1989; Ferreira et al., 1996; Hugalde and Vila, 2014; Conceição et al., 2017). Also the hydrological cycle of forest areas has been extensively studied, (e.g. David et al., 1994; Wilson et al., 2001; Testi and Villalobos, 2009), where the evapotranspiration is often determined as a residual term of the water balance (e.g. Pereira de Almeida and Riekerk, 1990; Baldocchi and Ryu, 2011). These and studies about the variation of forest evapotranspiration with weather conditions and disturbances (Kang et al., 2006; Bond-Lamberty et al., 2009; Whelan et al., 2015), were typically done at the catchment scale in different ecosystems. As part of this work was done in eucalypt plantations, there was a particular interest in finding studies about this tree species. However, studies focusing on the water cycle in eucalypt forests have been mainly conducted in Australia (Langford, 1976; Watson et al., 1999; Nolan et al., 2014, 2015), that differed to Portugal in their soil properties and climatic conditions. Generally, water balance studies give estimates over long periods and are reliable in determining the main input (precipitation) and outputs (evapotranspiration, drainage and runoff, Monteith, 1994).

Another method to obtain evapotranspiration is the eddy covariance (EC) method, by measuring exchanges of heat, mass, and momentum. It emerged in the late 1950s (Schotland, 1955; Suomi, 1957), but only with the development of the current generation of sonic anemometers, the EC method became more widely spread, not just by micrometeorologists but also by ecologists (Foken et al., 2012). Meanwhile, it is often considered as the reference method in water use studies. However, the EC method, which operates well on a field-scale, cannot be easily applied over areas with rugged and/or mountainous surfaces. The processing and interpretation of the data requires extensively-trained personnel and is still very costly.

Typical water balance studies or the EC method do not provide information about the two separate

ET_a components i.e. transpiration and evaporation. Transpiration, which is the liquid water vaporization from plant tissues and its removal to the atmosphere (Allen et al., 1998), can be estimated from sap flow measurements, which require additional on-site measurements to obtain transpiration (David et al., 1997; Wilson et al., 2001, e.g. stand sapwood cross-sectional area). Evaporation is the process of converting liquid water to water vapour (vaporization) and removing it from the soil surface (Allen et al., 1998). It can be obtained by using weighing lysimeters (Conceição et al., 2017; Ferreira et al., 1996). Both on-site measurements have the disadvantage that they are intensive in highly-qualified labour and, therefore, costly and unfeasible over long time spans. With the emergence of remote sensing methods, it is possible to obtain information on heterogeneous vegetation surfaces at different spatial and temporal resolutions.

1.2 Energy balance models and their concepts

The idea of dividing the evapotranspiration from vegetated surface into its contributing parts of soil and canopy, considers partial vegetation cover conditions and is suitable to operate with Earth observation systems to work over extended areas. In comparison, many ground based methods exist that accurately measure the components of the water or energy balance at field-scale. The output of on-site measurements are indispensable for model adjustments. However, it is not practicable to simply interpolate between those field-scale measurements, as a high spatial variability of the different vegetation types and soil properties exist (Scott et al., 2000; Sánchez et al., 2008a). In fact, over extended areas, local measurements are only meaningful when the area is homogeneous. This is also applicable for the use of one-source models that simplify the surface layer to a homogeneous vegetation layer of a certain height. A more detailed description of point location measurements, their development, and the distinction from one-source to two-source models is given in the introduction of Chapter 3.

All models based on flux gradient relationships (single or multi-layer models), consider the soil-plant-atmosphere continuum as an electric circuit, where at least two resistances (i.e. stomata and boundary layer resistance) must be overcome. Two-source energy balance models originated in the 1980s (Shuttleworth and Wallace, 1985; Choudhury et al., 1987). These models consider the soil and the vegetation layer as separate sources. Shuttleworth and Wallace (1985) used the concept of bulk stomata resistance and aerodynamic resistance of the vegetation for the vertical transport (see Monteith, 1965). To that, they added the concept of surface resistance of the substrates surface (r_a^s , upper soil surface, Monteith, 1981) and the resistances in the canopy (r_a^h , mean canopy flow).

Norman et al. (1995) proposed a two-source energy balance model that includes brightness temperature from remote sensing, assuming that the sensible heat flux density can be estimated from the surface temperature (T_{rad}). The authors suggested to estimate the energy fluxes by the contribution of the soil and the vegetation separately. It is difficult to estimate the different temperatures for the components of soil and vegetation, when only one surface temperature is available. Several authors extract these temperatures by establishing a relationship between the surface temperature (e.g. from satellite brightness temperature) and vegetation indices and/or partial vegetation cover (Carlson et al., 2007; Yang et al., 2015; Kasim and Usman, 2016).

This study is based on a model by Sánchez et al. (2008b) who further developed the model of Norman et al. (1995) which has previously been validated (Zhan et al., 1996; Kustas and Norman, 1999). A general scheme of the model, describing its input variables, processes, intermediate results and output is shown in Fig. 1.1.

Until today there are few studies testing remote sensing based TSEB models to separate ET_a into

transpiration and evaporation. Colaizzi et al. (2014) only recently tested a TSEB model to calculate ET_a and its components at cotton fields. They requested researchers to conduct similar studies for different crops and different water supply conditions, suggesting remote sensing platforms, from ground-based to satellite scales (Colaizzi et al., 2016).

In Ortega-Farías et al. (2016) another TSEB model was tested for partitioning ET_a into its components. They obtained surface temperature at very high spatial resolution of 6×6 cm, using multispectral and infrared thermal cameras mounted to a helicopter-based unmanned aerial vehicle (UAV). Their results encouraged to estimate transpiration and evaporation from lower spatial resolution (e.g. brightness temperature from satellite product), applying TSEB models.

In this study the STSEB model that is designed to operate with remote sensing data to estimate ET_a over different crops, was applied to benefit from these advantages.

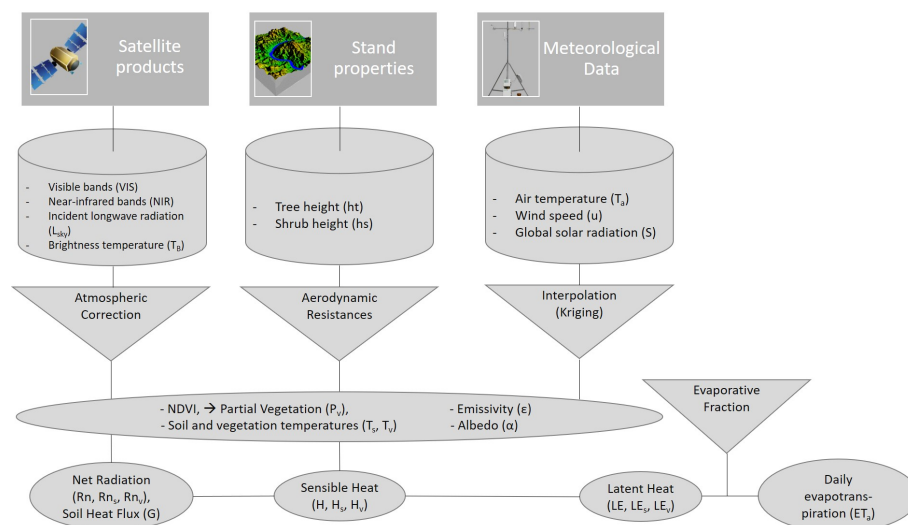


Figure 1.1: General overview of the input data (cylinders), processes (triangles) and generated output (ovals) by the two-source energy balance model inspired by Sánchez et al. (2008b)

The model was newly implemented in Python code and had first to be tested, even though the model's performance has already been studied over a variety of crops and forested areas (Sánchez et al., 2008b; Sanchez, 2008; Sánchez et al., 2009).

For testing the STSEB model, data from a long-term study at an olive orchard (WUSSIAAME – Water Use, Survival Strategies and Impact of Agrochemicals in Agricultural Mediterranean Ecosystems) were actively collected and further processed. This study provided high-quality data of ET_a and its components, by the means of different field measurement techniques (EC, lysimeter and sap flow measurements) over a period of three years. Long-term studies that provide own data for evaporation and transpiration from diverse on-site measurements are rare. The only ground-based technique for transpiration is to measure the sap flow, in which this research team has – as well as in other water use quantifications – several decades of experience.

Since the STSEB model can be adopted to any vegetation type, it has benefited from the existing datasets and the accumulated knowledge of the WUSSIAAME research team to explore the model for partitioning ET_a into its contributing parts, using remote sensing techniques. With this done, the model was applied to the olive grove with the aim of testing the agreement between measured and estimated ET_a , transpiration and evaporation as later described.

1.3 Wildfires and their effect on the water cycle

Wildfires disturb the terrestrial environment, the ecological aquatic processes and influence the water cycle in terms of the water quantity (e.g. stream flow) and water quality of streams (e.g. water pollution with nitrate inputs; increased water temperature by reduced tree shading, Hitt, 2003). They change the soils composition (e.g. pH, minerals) and porosity (e.g. soil texture), and thereby reduce the infiltration of the water into the soil. Hydrophobic substances lead to a higher water repellency (Nunes et al., 2016) that causes increased runoff, mudflows and soil erosion (Shakesby et al., 1993; Montes-Helu et al., 2009; Staley et al., 2017) especially in regions with steep slopes (e.g. Portugal, Prats et al., 2013). Wildfires, in particular crown fires, lead to a decrease of leaf area index (LAI) that is related to rainfall interception and vegetation transpiration (Mitchell et al., 2009). (Spracklen et al., 2012) observed a direct relationship between the change of vegetation cover and the local micro-climate (i.e. rainfall). In the case of Portugal, changes in ET_a are not related to changes of precipitation because the continental precipitation recycling ratio is extremely low, meaning there is no connection between these variables (Van der Ent et al., 2010).

Knowing the effects of fires on the water cycle, one becomes aware of the importance of determining its components such as the ET_a . No study was found local to Portugal, that deals with changes in ET_a after wildfires and its long-term recovery in eucalypt stands. This is important as recent literature investigated changes of ET_a that was up to double as high compared to ET_a from long unburnt forests. The differences lasted between 7 to 30 years (Nolan et al., 2014), affecting streamflow and consequently water supply in Australia. The increase of ET_a may be explained by fire induced epicormic resprouting, and together with an only partial defoliation, the overall leaf area might be temporarily higher than compared to unburnt stands.

Sánchez et al. (2015) studied changes in the energy flux patterns after wildfires that affected a pine and shrub area. For this purpose the STSEB model was applied using Landsat 5-TM and Landsat 7-EMT+ images, and meteorological data from the study site. The pine area mitigated differences in evapotranspiration between nine to eleven years, and the shrub area six to seven years after the fire.

In Portugal, only studies that investigated the effect of clear-cutting on the water cycle were found. Hawtree et al. (2015) analyzed time series of long-term hydrologic impacts of afforestation in the Águeda watershed that gave no implication of significant reductions in stream-flow. David et al. (1994) also studied streamflow after clear-cutting of *Eucalyptus globulus* in two watersheds 60 km north of Lisbon, Portugal. Only short-lived increases of streamflow were observed (about one to two years after clear-cutting).

The recovery time of ET_a to conditions before the fire breakout over a regional scale were investigated. Using the STSEB model provided the opportunity to do this also for the components of ET_a (transpiration and evaporation). In the literature, little is reported about the changes in transpiration and evaporation after wildfires. Nolan et al. (2014) observed tree and shrub transpiration and forest floor evaporation after wildfires at a re-sprouting mixed eucalypt forest. They showed that the contribution of the components to the total evapotranspiration was still different three years after the fire compared to unburned areas. The Australian study reported that the change in ET_a and its components was mainly influenced by the topography, through its effects on forest structure, the evaporative demand, and the fire severity.

However, in literature there are unburned forest studies that measured the transpiration of different tree species. Roberts (1983) compared several studies from northern European tree species. The listed studies lacked partly in description of the understory, but the forests covered a range of full canopy cover to open stands. They found no significant differences for annual transpiration. Benyon and Doody (2015) confirmed this finding for *Eucalyptus globulus* Labill. and *Pinus radiata*. As the ground-based data collection of transpiration is rather work intensive (Benyon and Doody, 2015; Sun et al., 2017),

only few studies exist, measuring the sap flow at forest stands. In Portugal David et al. (1997) measured transpiration with the *Granier* sap flow method (Granier, 1985) to understand the evolution of transpiration from *Eucalyptus globulus* canopies during drying periods, by assessing the role of the main controlling factors. They concluded that the long-term trend of transpiration during the dry spring-summer period was mainly controlled by the soil moisture deficit (SMD). The data of David et al. (1997) were also used to obtain a possible stress coefficient (K_s) for eucalypt stands. By knowing the soil water content, rainfall (input) and the estimated daily ET_a , it was possible to estimate when the soil water might be depleted (permanent wilting point, PWP).

1.4 Fire danger rating

For fire danger assessment, the fuel moisture content plays an important role of the potential of fire ignition and fire spread. According to Torres et al. (2018), only few studies link the soil moisture to fire danger. Possible reasons might be that the retrieval of on-site soil moisture measurements are rather work intensive and that they will only be valid on a field-scale (Brocca et al., 2007).

The estimation of SMD from space deal with other limitations. Many studies attempted to relate vegetation indices from remote sensing data to wildfire occurrences (Chuvieco et al., 2004; Bisquert et al., 2014). However, according to Qi et al. (2012) the soil moisture content has a much stronger correlation with live fuel moisture than with measures of photosynthetic activity e.g. Normalized Difference Vegetation Index (*NDVI*).

Another satellite data application is to retrieve soil moisture from microwave data, but the current satellite products have spatial and temporal restrictions. For example, the Soil Moisture Ocean Salinity product (SMOS; Level 3) is provided in 2-3 days interval with a pixel size of about 40 km, which in many cases is too coarse for the end-user. Lately, Sentinel-1 microwave data is used to retrieve soil moisture and is combined with other satellite products such as Landsat-7/8 for high spatio-temporal resolution (Amazirh et al., 2018). An overview of remotely sensed soil moisture data is given by Mohanty et al. (2017), listing the instruments and satellite platforms with their corresponding resolutions in time and space.

For the reasons just mentioned, the regional fire danger rating systems are still mainly based on local meteorological measurements. These measurements are used to estimate the moisture content of living and dead fuels and the water content of the soil, being reliable for the assessment of fire danger. The Drought Code (DC) is an index of the moisture content of deep, compact soil organic layers, closely correlated with seasonal drought effects on plant fuels. It belongs to the Canadian Forest Fire Weather Index (FWI), which is a fire danger rating system released in Canada in 1970. The FWI consists of six different subindices, where all are determined by daily meteorological recordings (e.g. temperature, wind speed, relative humidity and rain). Three of the indices represent the fuel moisture of soil, dead and living fuels. Another two subindices obtain the fuel consumption and the rate of spread, and a final index represents the fire intensity as energy output rate per unit length of fire front (Van Wagner, 1974).

The DC is based on a very simple water balance equation, where the only input is the effective rainfall (P_{eff}) and the output is the estimated ET_a by dividing the reference evapotranspiration ET_o by two (in the literature ET_o is often referred to as potential evapotranspiration, ET_p). The ET_o equation is based on the approach of Thornthwaite (1948), who suggested to estimate water requirements of plants by using air temperature (T_a) and day length. The equation estimates he obtained were very imprecise and only suitable for the region where the measurements were taken. Monteith (1994) cited Thornthwaite who

criticized his own equation by saying: "This mathematical development is far from satisfactory...it is completely lacking in mathematical elegance. It is very complicated and without nomograms and tables as computing aids would be quite unworkable. The chief obstacle at present to the development of a rational equation is the lack of understanding of why potential evapotranspiration corresponding to a given temperature is not the same everywhere." (Thornthwaite, 1948). Nevertheless, since decades in practice, but also for many research purposes the equation to retrieve ET_o from the DC stays unmodified.

The Keetch-Byram Drought Index (KBDI) is another fire danger index based on the water balance equation and often used to estimate SMD. The equation suggested by Keetch and Byram (1968) uses the mean annual rainfall and the maximum daily temperature (T_{max}) to compute the drought factor. It depends on several assumptions (i.e. arbitrary soil depth of 8 inches, evapotranspiration rate is a function of weather variables and vegetation density).

Once again, the actual removal of water vapor is based on an empirical equation of ET_o . For that reason, the research presented in this thesis uses the estimated ET_a from the STSEB model to improve the actual water balance and to obtain a better spatial resolution (500 m, MODerate-resolution Imaging Spectroradiometer, MODIS) for SMD estimation. This approach, its application, and the obtained results are given in Chapter 5.

Objectives and structure

This work is at the interface between water use and forest fire management, where traditional methods from hydrology science are applied to the science of forestry to studying the impact of wildfires on the hydrological water balance. Water relationships before and after fire outbreaks were investigated, concentrating on the ET_a estimated from remote sensing.

The research topic was divided into three main objectives:

- i testing the agreement between measured and estimated ET_a and its contributing parts of transpiration and evaporation from the STSEB model;
- ii analyzing the quantitative changes of the energy balance fluxes, and therefore daily ET_a after wild-fires; and
- iii identifying areas with higher proneness to fire, by the incorporation of estimated ET_a into drought indices.

Each objective of this list was dealt with in a research paper and published (or submitted) to *Scopus* indexed international journals, and are covered in chapters 3–5.

Chapter 3 describes the first study, where the STSEB model was tested for partitioning ET_a into transpiration and evaporation. For this work, the model was implemented in Python code (according to Sánchez et al., 2008b) and extended by the evaporative fraction method described by Gentine et al. (2007) to obtain daily values. The model's outputs were compared to field measurements of ET_a , transpiration and evaporation, respectively. To improve daily estimates the β -factor correction by Van Niel et al. (2011) was implemented.

In Chapter 4, the STSEB model was applied to burnt eucalypt forests at the Caramulo mountain range between Aveiro and Viseu. Fire-driven changes of the surface energy fluxes were investigated by comparing burnt areas with close-by unburnt tree stands. Hereby, the burnt areas were classified into their burn severity, resulting in information about changes in ET_a and the partitioning of transpiration and evaporation after fire events.

Chapter 5 explores the use of the estimated ET_a from STSEB for fire danger rating. For this reason drought indices based on the water balance equation were modified by substituting the empirical equations for evapotranspiration with ET_a from STSEB. A classifier was introduced to identify the minimum area prone to fire by including the maximum fire-affected regions. The basal crop coefficient (K_{cb}) and the adjusted crop coefficient ($K_{c,adj}$) approach to estimate ET_a for days with no satellite observations were applied.

Chapter 6 gives a general conclusion of the results and illustrates perspectives for follow-up projects.

Further methods and results, which have not been described or published yet, are included as supplemental material.

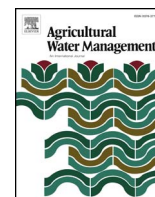
Estimation and partitioning of actual daily evapotranspiration at an intensive olive grove using a simplified two-source energy balance model, (Article I)

This paper describes the testing of the STSEB model in terms of estimating the components of ET_a , (i.e. transpiration and evaporation). For this reason, data from a long-term study at an olive grove was exploited, due to familiarity with the study site, and the associated data collection. Beta-factor corrections according to Van Niel et al. (2011) improved the model for ET_a estimations.

This chapter was originally published in *Agricultural Water Management*, 31 March 2018, ©Elsevier B.V., available online:

<https://doi.org/10.1016/j.agwat.2018.01.027>. The journal was rated with an impact factor of 3.182 and a 5-year impact factor of 3.565 in September 2018.

Melanie Häusler, Nuno Conceição, Luca Tezza, Juan M. Sánchez, Manuel L. Campagnolo, Andreas J. Häusler, João M. N. Silva, Thorsten Warneke, Georg Heygster, and M. Isabel Ferreira.



Estimation and partitioning of actual daily evapotranspiration at an intensive olive grove using the STSEB model based on remote sensing



Melanie Häusler^{a,*}, Nuno Conceição^c, Luca Tezza^d, Juan M. Sánchez^e, Manuel L. Campagnolo^{a,b}, Andreas J. Häusler^f, João M.N. Silva^a, Thorsten Warneke^g, Georg Heygster^g, M. Isabel Ferreira^{b,c}

^a Forest Research Centre, School of Agriculture, University of Lisbon, Tapada da Ajuda, 1349-017 Lisbon, Portugal

^b DCEB, Departamento de Ciências e Engenharia de Biosistemas, Instituto Superior de Agronomia, Universidade de Lisboa, Tapada da Ajuda, 1349-017 Lisboa, Portugal

^c LEAF, Linking Landscape, Environment, Agriculture and Food, Instituto Superior de Agronomia, Universidade de Lisboa, Tapada da Ajuda, 1349-017 Lisboa, Portugal

^d CIRVE, Interdepartmental Centre for Research in Viticulture and Enology, University of Padova, 31015 Conegliano, TV, Italy

^e IDR, Regional Development Institute, Applied Physics Department, University of Castilla-La Mancha, 02071 Albacete, Spain

^f Salt and Pepper Technology GmbH & Co. KG, Bremen, Germany

^g Institute of Environmental Physics, University of Bremen, 28359 Bremen, Germany

ARTICLE INFO

Keywords:

Landsat

Evaporation

Transpiration

Evaporative fraction method

ABSTRACT

This study is based on the application of an existing simplified two-source energy balance (STSEB) model, using medium-resolution satellite imagery (Landsat) to estimate instantaneous (at the satellite overpass time) and daily actual crop evapotranspiration (ET_a) over an intensive olive grove. Daily values were obtained by the use of the evaporative fraction method and corrected for latent heat, available energy, and evaporative fraction biases (beta-factor correction). Model estimates were compared to ground-based measurements. Heat flux densities (eddy covariance method) were recorded, and five Landsat images at approximately monthly intervals were used, covering our study site in 2011. Comparison with ground measurements showed a maximum difference of -0.6 mm day^{-1} before, and 0.2 mm day^{-1} after beta-factor correction for the main plot.

The experimental site consisted of a main plot exposed to deficit irrigation, and two small subplots where—during a limited period of time (six weeks)—one was temporarily not irrigated, and the other well-irrigated for reference. One Landsat image was available for this limited period of time.

Additionally, the STSEB algorithm was tested for partitioning evapotranspiration into its evaporation and transpiration components. Evaporation estimated from the STSEB model was compared with evaporation estimated from a model adjusted from local lysimeter measurements. Transpiration data obtained from calibrated sap flow measurements were, after local calibration, also compared to model estimates. Model results agreed with the measured data, showing) under- and overestimation for transpiration and evaporation, respectively.

1. Introduction

Over the last decade, more and more traditional olive orchards ($< 100 \text{ trees ha}^{-1}$) have been replaced by intensive to super-intensive ones ($> 2000 \text{ trees ha}^{-1}$), especially in the South of Portugal with Mediterranean climate conditions. This development demands improved water management and optimised irrigation practices in terms of quantifying olive water requirements. This study aims to estimate actual evapotranspiration (ET_a) and its contributing parts of canopy transpiration (LE_v) and soil water evaporation (LE_s), as the latter is often seen as water loss for irrigated crops. An existing simplified two-source energy balance model (STSEB) based on Norman et al. (1995) and further simplified by Sánchez et al. (2008b) has been, in

combination with satellite imagery, tested for separately estimating LE_s and LE_v on a daily basis.

To estimate the amount of water transferred to the atmosphere from different crops, various estimation approaches have been developed, in general using implicitly (or explicitly) the leaf surface conductance (bulk stomatal and leaf boundary layer). Due to the difficulty in obtaining this variable for every crop in any water status condition, simple semi-empirical models have been used to calculate ET_a for decades. The principle is based on the reference evapotranspiration (ET_0) estimated from on-site collected meteorological data, which then is multiplied by a crop coefficient, obtaining ET_m ($k_c = ET_m/ET_0$) and finally by a stress coefficient ($k_s = ET_a/ET_m$). In a well-known group of guidelines (FAO Irrigation and Drainage Paper 56), Allen et al. (1998) proposed

* Corresponding author.

E-mail address: aa18795@isa.utl.pt (M. Häusler).

estimating ET_0 based on the Penman-Monteith equation, which incorporates aerodynamic and physiological parameters of a previously defined reference grass to retrieve k_c and k_s coefficients.

An alternative approach to obtain ET_a and its contributing parts, LE_v and LE_s , was adopted from the energy balance equation (Eq. (A.1)). A distinction is drawn between one- and two-source models, to account for the different heat transfers from the soil surface and the plant canopy. One-source models assume one surface temperature and aerodynamic resistance for the zone of soil and vegetation cover while the two-source models identify soil and vegetation layers as separate sources of heat flux.

To date, many studies have been carried out over annual crops or uniform land covers (Tasumi et al., 2005; Agam et al., 2010; Hoffmann et al., 2016; Timmermans et al., 2007), and many studies have dealt with heterogeneous ground cover (Bastiaanssen et al., 1998; Colaizzi et al., 2016; Roerink et al., 2000), and only recently with tree crops (e.g. olive orchards; Cammalleri et al., 2012; Pôças et al., 2014; Ortega-Farías and López-Olivari, 2012).

Due to the accessibility of satellite data, remote sensing based estimations of ET_a (Sun et al., 2012; Peng et al., 2012; Minacapilli et al., 2016), combined with energy balance models (Du et al., 2013; Ruhoff et al., 2013), became more and more attractive, especially because only a few additional meteorological variables (e.g., air temperature, wind speed, global solar radiation) are needed, being regularly measured at meteorological stations. Yang et al. (2015a) made a comparison between three two-source remote sensing evapotranspiration models, where two of them were two-source energy balance models (TSEB) and the third was the MOD16 ET_a algorithm (algorithm according to Norman et al., 1995 and Nishida et al., 2003b,a). Results showed that MOD16 failed to reproduce spatial ET_a patterns over particularly dry environments, while the TSEB model was in agreement with the ET_a measurements.

Generally, TSEB models give reasonable results for ET_a , and are used for separately estimating LE_v and LE_s , which, based on remote sensing has not been tested yet, to its full extent. One reason might be that TSEB models tend to overestimate LE_s and underestimate LE_v (Colaizzi et al., 2014, 2016). Here, the STSEB model gives the opportunity to operate on a larger scale (e.g. field-scale), due to relatively few input variables, the use of standard meteorological data, and satellite imagery. Daily values of ET_a , LE_v , and LE_s were estimated using the Evaporative Fraction (EF) constant method. Correction factors (beta-factors), according to Van Niel et al. (2011), were tested to improve model estimations.

On this background, the objectives of this study were to:

- i estimate instantaneous ET_a in discontinuous vegetation e.g., for an olive grove;
- ii detect significant reductions in evapotranspiration due to the water status of the trees;
- iii test the performance of the model for partitioning evapotranspiration into its contributing parts (transpiration and evaporation); and
- iv evaluate the overall ground cover dynamics (effect of canopies and inter-row soil cover) affecting the use of satellite imagery.

On-site measurements of total ET_a , obtained with the eddy covariance (EC) method, and its contributing parts (LE_s and LE_v) were compared to the model estimates. Consequently, the sections highlighting the results of the research at hand, as well as the discussion of these results, are split in accordance with the aforementioned objectives.

2. Materials and methods

A detailed description of the experimental set-up, instrumentation and their specifications are given in Conceição et al. (2017).

2.1. Study site

This work is based on data obtained in an intensive olive grove in the southeast of Portugal, located in the region of Alentejo in 2011 (latitude: 38°1'15.90" N, longitude: 8°10'44.50" W, Datum WGS84, 97 m above sea level). In September 2004, a 10-ha olive grove (cv. *Arbequina*) with a tree spacing of 4.8 m, and a row spacing of 7 m was installed, where a continuous area of 434-ha was selected for taking measurements.

In 2010, the average height of the trees was 3.2 m, the average canopy projected area was 5.7 m², and the average leaf area index on a total area basis was 1.01 m² m⁻². Further biometric measurements were taken and are described in Häusler et al. (2014).

The climate in the region of Alentejo is temperate and is one of the Mediterranean types, Csa, characterized by mild and wet winters and very hot and dry summers (Köppen Geiger Classification Rubel and Kottek, 2010). The average annual rainfall is about 580 mm, with around 5% falling during summer time (<http://www.ipma.pt/>). The soil was classified as *Luvisol* (Food and Agriculture Organization of the United Nations (FAO), 2006) with a ApBtC profile.

The total olive orchard, with the exception of two subplots, during a limited stress period, was deficit-irrigated. Each tree row had a line of drippers spaced 0.75 m apart. The nominal flow for the deficit irrigation was 1.6 L h⁻¹, which corresponds to an irrigation flux density of 0.31 mm h⁻¹. During 2011 the deficit irrigation operated from 15 June to 26 September (103 days) with an average irrigation depth of 1.4 mm day⁻¹.

During six weeks, two subplots received different treatments. One received no water at all (Subplot 2) and the other was well-irrigated (Subplot 3; see also Section 2.2.3 and Conceição et al., 2017). Pre-dawn leaf water potential served to monitor and define the plant water status. According to Fernandes-Silva (2008) plants are in comfort between -0.4 MPa and -0.7 MPa. The observed values for the well-irrigated Subplot 3 were never below -0.5 MPa (Conceição et al., 2017). Trees with a pre-dawn leaf water potential of down to -0.5 MPa were therefore defined as being in comfort. Values below this point indicated water-stressed olive trees.

2.2. On-site measurements

2.2.1. Measurement of energy heat fluxes at the main plot

The installation of EC sensors allowed the measurement of the flux densities of latent heat flux density LE and sensible heat flux density H with a three-dimensional sonic anemometer and a krypton hygrometer (CSAT3-D and KH20, respectively, Campbell Scientific, USA), which were mounted on a metallic tower at the height of 4.5 m above ground and oriented into the dominant wind direction (Fig. 1). Raw fluxes (H and LE) were recorded by a data logger (CR10X, Campbell Scientific, USA), and 30 min averages were stored. Corrections for air density variations (WPL-correction, Webb et al., 1980), and oxygen cross sensitivity for krypton hygrometers (because of oxygen absorption, Tanner et al., 1993) were performed.

The net radiation R_n was measured with net radiometers (NR2 and NRLite, Kipp & Zonen, Netherlands) and the soil heat flux density G was recorded, using six heat flux plates (heat flux sensors HFP01 and HFT-3.1 manufactured by Hukseflux and Radiation and Energy Balance Systems, respectively) with known thermal conductivity. The heat flux plates were buried in the ground at a depth of 0.05 m, perpendicular to the flow direction. To quantify the heat stored in the soil layer between 0 and 0.05 m, copper-constantan thermocouples were used at 0.025 m soil depth (1/30 Hz, 10 min average). Further information about equipment and data processing, are described in Conceição et al. (2017).

A simplified footprint analysis (Schuepp et al., 1990) allowed the evaluation of the relative contribution of fluxes coming from different areas within the plot to the total measured flux. More than 85% of the

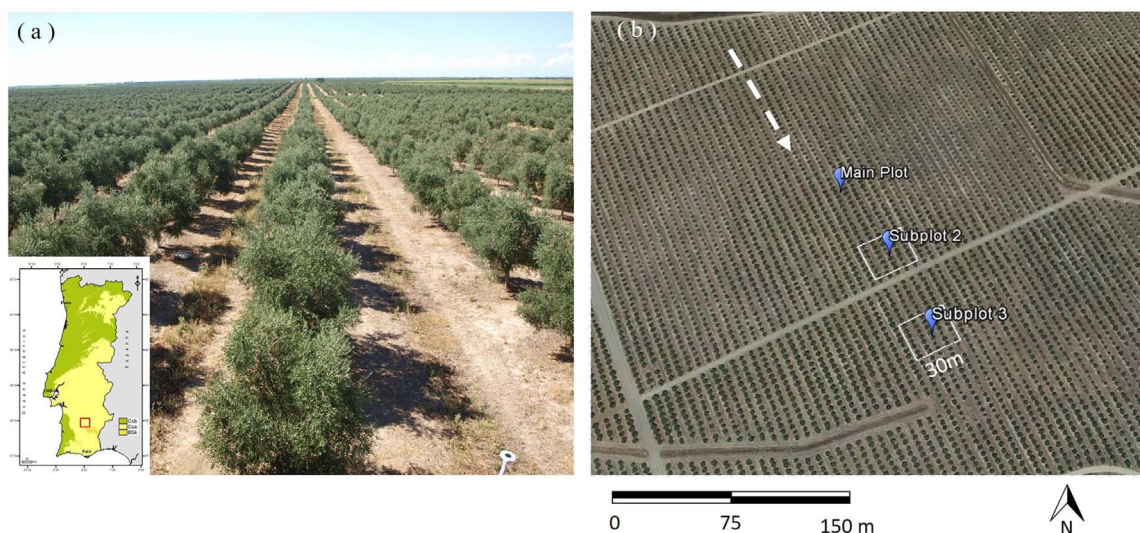


Fig. 1. Image (a) shows a seven-year old intensive olive grove (cv. *Arbequina*) with a tree spacing of 7×4.8 m. The location of the experimental site is marked by a red square in the map of Portugal (left corner, Köppen-Geiger Classification) Web references [1]. Image (b) gives an overview of the total test site with its numbered subplots (extracted pixels, 30 m, white squares) and the location of the eddy covariance tower (main plot). The main wind direction is illustrated by white dashed arrows. Web references [2]. (For interpretation of the references to color in this figure legend, the reader is referred to the web version of this article.)

measured LE came from an upwind area less than 140 m away from the measurements' point. LE and H fluxes were selected according to the wind direction, taking into consideration the outputs from the footprint analysis (Conceição et al., 2017) in relation to the fetch for each direction.

2.2.2. Transpiration and soil evaporation at the main plot

Using the thermal dissipation method (Granier, 1985), the sap flow was recorded for seven trees in the main plot. Measurements were taken every 60 s and averaged every 30 min by a data logger (CR3000, Campbell Scientific, USA; for details see also Conceição et al., 2017).

Measurements of LE_s with micro-lysimeters were taken. In total, ten lysimeters were installed. Here, six of them were along the tree line with a spacing of 0.75 m and another four near the line, where two of which were in the shade of the crown and two exposed to the sun (Tezza, 2014). The lysimeter measurements were used to model LE_s for the days where no measurements were taken, using locally adjusted model parameters, as described in Tezza (2014) and Conceição et al. (2017). By subtracting LE_s (micro-lysimeters or model) from ET_a , measured at the EC tower, LE_v was obtained. Subsequently, LE_v was compared with average sap flow data in order to correct it, obtaining a time-series for LE_v of the main plot under deficit irrigation where also total LE was measured. Afterwards, it was possible to infer LE_v for the small Subplots 2 and 3, in the way explained in the following section.

2.2.3. Transpiration of the two subplots

For the duration of a stress period (3 August to 15 September, 2011) the experimental site had additionally two small subplots outside the footprint area of the main plot (Fig. 1). In each of the two subplots, sap flow measurements for six trees were taken, also using the thermal dissipation method as described by Granier (1985). Subplots 2 ($38^{\circ}1'13.99''$ N, $8^{\circ}10'42.68''$ W) and 3 ($38^{\circ}1'11.81''$ N, $8^{\circ}10'41.12''$ W) were equipped with independent irrigation systems, and a stress period was temporarily induced from 3 August (Day of the Year = DoY, 215) until 15 September (258), 2011 in Subplot 2.

Only during the stress period of six weeks, Subplot 2 remained non-irrigated, while Subplot 3 was kept well-irrigated for reference, (pre-dawn leaf water potential above -0.5 MPa). This experimental lay-out was used to analyse the impact of water shortage on water stress indicators and water fluxes (Ferreira et al., 2012a). Before the beginning of the stress period, all plots had reached maximum water status

(comfort, > -0.5 MPa of pre-dawn leaf water potential). The main plot (1) continued to be deficit-irrigated (approximately 1.4 mm day $^{-1}$).

The value of LE_v for the well-irrigated Subplot 3 was obtained by dividing LE_v of the main plot by the stress coefficient of the main plot ($LE_{v,3} = LE_{v,1} \div k_{s,1}$), which takes into account the LE_v reduction in the main plot, being deficit-irrigated. This factor ($k_s = 0.88$) was retrieved from the relationship between pre-dawn leaf water potential and k_s or relative LE_v obtained during the stress period, (Ferreira et al., 2012b; Conceição et al., 2017), by using the values measured in all subplots for the day of satellite overpass during this stress cycle. The same principle was applied to LE_v for the highly stressed Subplot 2 (day of satellite overpass on DoY 255, 2011) by using the measured relative LE_v of this plot (i.e., $k_s = 0.77$, being LE_v of stressed Subplot 2 = LE_v of the well irrigated Subplot 3 multiplied by 0.77, because $LE_{v,2} = LE_{v,3} \times k_{s,2}$).

Five cloud-free Landsat 5 Thematic Mapper (L5-TM) images were selected in approximately monthly intervals from May until October 2011, including one image during the stress period. The sensor aboard Landsat 5 has a medium spatial resolution (30 m in visible and near-infrared bands, and 120 m in the thermal band), and offers a detailed observation of the Earth's surface. The Level 1 product of surface reflectance data (Level 1 product, Bands 1-5 and 7, atmospherically corrected by Landsat Ecosystem Disturbance Adaptive Processing System, LEDAPS), and the brightness temperature (Band 6), provided by the U.S. Geological Survey Earth Resources Observation and Science (EROS) Data Center (<http://earthexplorer.usgs.gov/>) were downloaded, and further processed.

For the estimates of the main plot a square of 3×3 pixels within the footprint area was extracted and averaged, while for the Subplots 2 and 3 central coordinates were used to extract the corresponding pixels in the images to compare with ground observations. The subplots themselves covered only around 941 m 2 (28 trees), corresponding to the 30×30 m pixel size of the visible band of Landsat. We have tested two approaches – averaging over the overlapping pixels or using just the closest pixel to the center of each subplot – and since the latter lead to better estimates we have used it in our calculations, knowing that the tree-lines were rather uniform.

Landsat-derived albedo (α), land surface temperature (T_{rad}) and Normalized Difference Vegetation Index (NDVI, see Section 3.4) were plotted against ET_a for 15 observation days along the year 2011. The time pattern of those variables was compared to verify that the input data for the STSEB model were in line with the annual distribution of

remote sensing data. Furthermore, simple and multiple regression models, using as predictors α , T_{rad} or $NDVI$, were fitted to evaluate how the STSEB model improved the ET_a estimation over simple statistical models.

The global solar radiation (S) was provided by the Copernicus Atmosphere Monitoring Service (CAMS) and downloaded from SoDa (Solar Energy Services for Professionals, <http://www.soda-pro.com/>). Air temperature (T_a) and wind speed (u) were measured on-site at the EC tower, and the instantaneous values used for modeling are given in Table 2.

The incident long-wave radiation (L_{sky}) was provided by the Spinning Enhanced Visible and Infrared Imager (SEVIRI) aboard Meteosat and retrieved with 3 km pixel size from the EUMETSAT Satellite Application Facility on Land Surface Analysis (LSA SAF; <https://landsaf.ipma.pt/>). Due to uniformity over a large area (Humes et al., 2004), the L_{sky} value of the pixel that included the test site was further processed.

Atmospheric transmissivity (τ), hemispheric down-welling sky irradiance (L_{atm}^{\downarrow}) and hemispheric up-welling sky irradiance (L_{atm}^{\uparrow}) were obtained by introducing radio-sounding data into the MODTRAN 4.0 code (Berk, 1999). The atmospheric parameters (τ , L_{atm}^{\downarrow} , and L_{atm}^{\uparrow}) served for atmospheric corrections in order to obtain T_{rad} from brightness temperature and were calculated by the Atmospheric Correction Parameter Calculator (<http://atmcorr.gsfc.nasa.gov/>, Barsi et al., 2003).

2.3. Model description

The STSEB model (Sánchez et al., 2008a) is based on the energy balance equation (Eq. (A.1)), and estimates instantaneous values for R_n , H and G ($W m^{-2}$) from meteorological data and satellite imagery, in order to obtain LE . To retrieve daily values from the instantaneous ones, the EF method (described at the end of this section) was applied, i.e. the ratio of LE and the available energy during satellite overpass. G was estimated as a portion of R_n (Eq. (A.11), Choudhury et al., 1987), and considered for retrieving daily ET_a , using the EF method.

2.3.1. Instantaneous values

One of the key processes in the STSEB model is the successful partitioning into the contributing parts of the vegetation (v) and the soil (s) (Timmermans et al., 2007; Kustas et al., 2012; Sánchez et al., 2015b) in order to obtain P_v (Eq. (1), Valor and Caselles, 1996). This means that P_v is calculated from the $NDVI$ (Eq. (A.5)) and the coefficient K (Eq. (A.6)):

$$P_v = \frac{\left(1 - \frac{NDVI}{NDVI_s}\right)}{\left(1 - \frac{NDVI}{NDVI_s}\right) - K \times \left(1 - \frac{NDVI}{NDVI_v}\right)} \quad (1)$$

Both ($NDVI$ and K), were calculated from the red- and near-infrared bands (B_3 and B_4). Band designations (B_i) for Landsat satellites are provided by the official site of U.S. Geological Survey (USGS, <http://www.usgs.gov/>). The fully vegetated and bare soil areas were manually selected by the use of the $NDVI$, and averaged. They are referred to by the subscripts of v and s, respectively (Region of Interest = ROI;

Table 1
Changing soil (s) and vegetation (v) characteristics for different Landsat 5 images, where B_3 and B_4 denote the red and near-infrared bands, respectively.

Image (L5-TM)	B_{4v}	B_{4s}	B_{3v}	B_{3s}	$NDVI$	$NDVI_v$	$NDVI_s$
23 May 2011	0.341	0.210	0.041	0.131	0.40	0.782	0.237
24 Jun 2011	0.399	0.281	0.040	0.197	0.43	0.814	0.187
26 Jul 2011	0.378	0.294	0.049	0.206	0.38	0.768	0.175
12 Sep 2011	0.375	0.285	0.039	0.201	0.39	0.810	0.173
30 Oct 2011	0.408	0.177	0.044	0.125	0.40	0.803	0.175

Table 2
Average records of model variables for the main plot (3×3 pixels) at the time of satellite overpass. T_a represents the air temperature and u the wind speed recorded at the eddy covariance tower. T_v and T_s were extracted by plotting P_v (partial vegetation) against land surface temperature T_{rad} , and were fixed to certain values for modeling (see Section 2.3 for details).

Date (DoY)	T_a (°C)	T_v (°C)	T_s (°C)	u ($m s^{-1}$)	P_v
23 May (143)	28.7	34.9	37.8	1.4	0.27
24 Jun (175)	27.9	28.5	45.3	1.6	0.39
26 Jul (207)	29.2	29.7	46.9	1.5	0.37
12 Sep (255)	27.5	29.6	41.9	1.2	0.37
30 Oct (303)	20.7	22.3	34.9	0.8	0.28

Table 1). The ROIs obtained for the $NDVI_v$ and $NDVI_s$ classification were also used to obtain the average values of the bands for vegetated and bare soil regions for K . The classification of the $NDVI$ into vegetated and bare soil regions are found in Sobrino et al. (2004).

Separating T_s and T_v when only T_{rad} is available is probably the most intricate issue in the STSEB models. Hereby, for each day, T_{rad} retrieved from the thermal band (Eq. (A.7)) was plotted against P_v (main plot, 3×3 pixels), where isolines with an almost linear relationship were obtained (Carlson, 2007; Yang et al., 2015b; Kasim and Usman, 2016). First estimates for the components soil T_s and canopy T_v temperature of T_{rad} were retrieved. Here, higher temperatures related to low values of P_v (bare soil pixels), represented the estimate of T_s , while lower temperatures related to high values of P_v (vegetated pixels) gave the estimate for T_v during satellite overpass (Table 2).

The partitioning of the different fluxes into soil ($1 - P_v$) and canopy (P_v) components was used to estimate H_s (Eq. (A.10)) and H_v (Eq. (A.9)), separately. To be consistent, this approach was also applied to estimating the contributing parts of soil and vegetation cover for R_n , adapting Eq. (A.2), by using the soil and canopy specific emissivities and α . Following this methodology, the component fluxes of LE_s and LE_v , as well as total LE were retrieved, applying:

$$LE_s = R_{ns} - H_s - \frac{G}{(1 - P_v)} \quad (2)$$

$$LE_v = R_{nv} - H_v \quad (3)$$

$$LE = P_v LE_v + (1 - P_v) LE_s \quad (4)$$

2.3.2. Daily values

Finally, daily values were retrieved by applying the EF constant method as described in Ruan et al. (2014). This algorithm assumes that EF is constant during the daytime hours, and is defined for the total scene, and the individual portions of canopy and soil, respectively as:

$$EF_{t,i} = \frac{LE_i}{R_{ni} - G_i} \quad (5)$$

$$EF_{v,i} = \frac{LE_{v,i}}{R_{nv,i}} \quad (6)$$

$$EF_{s,i} = \frac{LE_{s,i}}{R_{ns,i} - G_i} \quad (7)$$

where i denotes the instantaneous values measured (or estimated) at the time of satellite overpass for the total (t) scene, the canopy (v) or soil (s) contribution (Gentine et al., 2007).

However, Van Niel et al. (2011) address three major surface energy balance interactions with EF that result in a bias. Those interactions are called beta-factors and represent the systematic errors in LE , in the available energy ($R_n - G$), and in the evaporative fraction (assuming daytime self-preservation). The combined influence of the beta-factors was determined and multiplied as explained in Van Niel et al. (2011). The daily values of ET_a were then multiplied by the combined beta-factors as listed in Table 4. Physical background and application of the

beta-factors must be retrieved from the given reference as this is beyond of the scope of this paper.

Daily ET_a (mm day^{-1}) were retrieved from instantaneous observations using (Ruan et al., 2014):

$$ET_{a,daily} = 8.64 \times 10^7 \times EF_i \frac{R_{nd} - G_d}{L \times \rho_w} \quad (8)$$

where L is the latent heat of vaporization given in MJ kg^{-1} , ρ_w is the water density (1000 kg m^{-3}), and EF_i is the evaporative fraction for the total scene, the soil, or the vegetation contribution (Eqs. (5)–(7)).

2.4. Time series analysis of remote sensing data

The STSEB model relies on the surface reflectance and the thermal band of L5-TM. However, for the time series, Landsat 7 Enhanced Thematic Mapper Plus (L7-ETM+) data were also available. A total of 15 observations, from May 15, 2011 until October 30, 2011, were evaluated, testing the representativeness of the five observations used for the STSEB model. Since the STSEB model was not used to estimate ET_a for the additional ten dates, we limited ourselves to looking at the relation between Landsat-derived variables used in the STSEB model, and in-situ measured ET_a . The combination of TM and ETM+ data for the STSEB model, would have further complicated our analysis and add additional variability (different sensors and orbits), and was therefore not considered.

To investigate whether ET_a could be modeled by simple linear regression on the predictor variables α , $NDVI$ and T_{rad} , (which were extracted from a time series of Landsat data), multiple linear regression techniques were used. The linear model assumes that the response variable can be written as a linear function of the predictors, plus a Gaussian random error ϵ . Formally,

$$Y_i = \beta_0 + \beta_1 x_{1(i)} + \dots + \beta_p x_{p(i)} + \epsilon_i, \quad i = 1, \dots, n \quad (9)$$

for the n observations and p predictors, where ϵ_i has a Gaussian distribution with mean 0 and fixed but unknown variance σ^2 . The goodness-of-fit is evaluated with the coefficient of determination R^2 , which measures the proportion of the variability of the response that is explained by the regression model. Nested models (i.e. where only a subset of predictors is considered) were compared using a F -test to understand if the inclusion of additional variables lead to a significant increase in the coefficient of determination (Dytham, 2011).

3. Results

3.1. Instantaneous ET_a

The satellite-derived R_n was underestimated by at most 26 W m^{-2} , compared to that measured. On average, the estimated values mismatched the ground measurements by only -3% (Mean Absolute Deviation = MAD of 17 W m^{-2}). The absolute maximum difference for H was 27 W m^{-2} , resulting in a relative deviation of 4% (MAD of 16 W m^{-2}). For G , a maximum absolute difference of -3 W m^{-2} was observed, and on average the values differed from the measured soil heat flux densities by -1% (MAD of 1.3 W m^{-2}) for the main plot. For LE , the maximum deviation of 28 W m^{-2} , resulting in an error of 18% (MAD of 36 W m^{-2}), on average, for the days analysed (see also Table 3).

3.2. Daily ET_a

Comparing the daily estimated values of R_n , LE , and H with the ones observed at the main plot, differences of -3% (MAD of 5 W m^{-2}), 14% (MAD of 15 W m^{-2}), and 3% (MAD of 5 W m^{-2}) were observed on average, respectively. Instantaneous values of G were estimated (Eq. (A.11)) and considered for modeling in order to retrieve daily values of

Table 3

Comparison of ground-based measurements with instantaneous model estimates of the energy balance surface fluxes (Meas. = Measured and Estim. = Estimated), where R_n is the net radiation, H the sensible heat flux density, LE the latent heat flux density and G the soil heat flux density.

Date (DoY)	H (W m^{-2})		LE (W m^{-2})		R_n (W m^{-2})		G (W m^{-2})	
	Meas.	Estim.	Meas.	Estim.	Meas.	Estim.	Meas.	Estim.
23 May (143)	154	181	193	247	625	613	189	186
24 Jun (175)	183	182	258	299	621	595	114	115
26 Jul (207)	148	175	242	267	570	550	108	107
12 Sep (255)	166	141	234	256	513	517	123	120
30 Oct (303)	119	120	157	196	371	347	31	30

LE by using the EF constant method. In Fig. 2, the daily measured G is given which was between -0.6 , and 17 W m^{-2} for the five days used for this study.

Generally, the daily estimated ET_a of the subplots were lower than the ones from the main plot with the exception of DoY 255, which was the observation day during the stress period. On that day, ET_a either measured or estimated from the model, was higher in Subplot 3 being well-irrigated. Therefore, Subplot 3 evapotranspired more than the main plot, which was kept deficit-irrigated. The model was able to detect a clear difference to Subplot 2 receiving no irrigation water at that time (Table 4).

Even though the differences between observed and estimated values were rather small (with exception of DoY 207) for the main plot, ET_a for Subplots 2 and 3 were underestimated, assuming the same conditions in comparison with the main plot, except for DoY 255 (e.g. tree height and tree distribution, water application and irrigation scheduling). Thus, the beta-factor correction as described by Van Niel et al. (2011) was used to account for systematic errors made in LE , available energy ($R_n - G$) and the evaporative fraction (assuming daytime self-preservation). The estimations, especially for DoY 207, could be improved (Table 4). In the main plot a difference of only 0.1 mm day^{-1} (before 0.6 mm day^{-1}) between measured and estimated ET_a was achieved after applying the beta-factor of 1.19. Subplots 2 and 3 were also corrected by this factor, reducing the underestimation from 1.0 mm day^{-1} to 0.3 mm day^{-1} .

3.3. Evaporation/transpiration partitioning

The possibility of separating evapotranspiration into its contributing portions of LE_v and LE_s by means of the STSEB algorithm was explored. Again, the EF constant method (Eqs. (2)–(8)) was used to estimate daily values from the records during the satellite overpass, and the beta-factor correction was applied as describe in Section 2.3.2.

A clear difference in LE_v was recorded during the stress period, which lasted from DoY 215 to 258 (3 August until 15 September, 2011). During this time, the main plot was kept deficit-irrigated while Subplot 2 was not irrigated at all (stressed), and Subplot 3 was kept near field capacity (control). Accordingly, Subplot 3 transpired the most during the stress period, while in relative terms Subplot 2 transpired the least.

The daily measurements of LE_v at the main plot and the subplots with the corresponding estimates are given in Fig. 3. For DoY 255 the graph displays extra data due to the fact that this was during the stress period applied to Subplot 2, when LE_v for Subplots 2 and 3 were also measured. For the main plot the greatest differences were observed for DoYs 175, and 207, with an underestimation of 1.4 mm day^{-1} , followed by DoY 255, with an underestimation of 1.0 mm day^{-1} .

For the Subplots 2 and 3 the greatest differences between observed and estimated LE_v were recorded at DoY 175 when the overestimation was 1.9 and 1.6 mm day^{-1} , respectively (Fig. 3).

In summary, the estimated daily LE_v values for the main plot and the subplots were underestimated. For the stress period (DoY 255), the

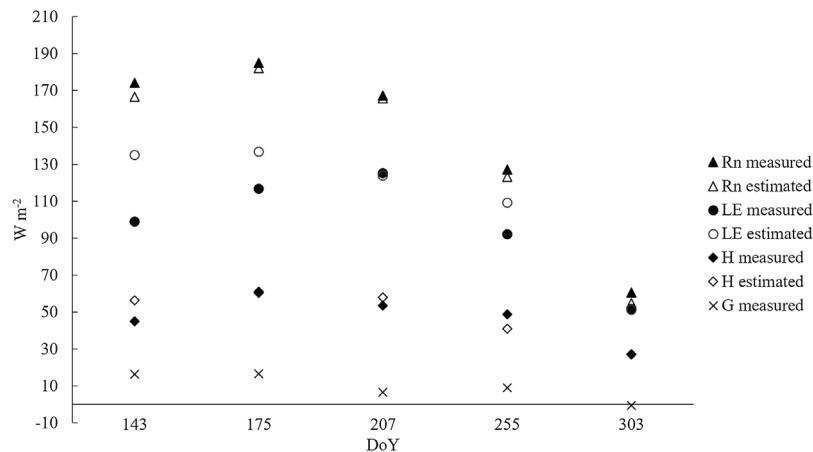


Fig. 2. Comparison of daily model estimates with ground-based measurements (R_n , H , LE , and G).

STSEB algorithm was able to detect differences in LE_v for the different water applications (Fig. 3, where Subplot 3 was highest (control), followed by the main plot (deficit-irrigated) and the Subplot 2 (stressed).

The fraction of LE_s (after application of EF method and systematic error correction) was compared with the model estimates, showing relatively large differences (overestimation) for the DoYs 175, 207, and 255, of at most 1.1 mm day^{-1} , but good agreement for the DoYs $143 \pm 0.2 \text{ mm day}^{-1}$, Table 5.

3.4. Time series analysis of remote sensing data

As discussed, the Landsat data were used to derive α (Eq. (A.3)), $NDVI$ (Eqs. (A.5), (1) and (A.6)), and to estimate T_{rad} (Eq. (A.7), see also Fig. 4b). Fig. 4a depicts the relations between the Landsat 5-7 derived variables (α , $NDVI$, and T_{rad}), and ET_a in-situ observations. One can notice that the five observations used in earlier sections were well distributed among the available data, which is an indication of their representativeness.

Fig. 4a shows that α had the best correlation with ET_a and that they were positively correlated. This resulted from the combined effect of both canopy and inter-row components of the Landsat signal: as summer progresses, the herbaceous component of ground cover dries out, and therefore the soil's reflectance increases. Simultaneously and independently, LE_v rates also increase due to irrigation in combination with a higher atmospheric demand.

$NDVI$ (Fig. 4a), on the other hand, showed a very weak correlation with ET_a . As expected, it showed lower values in summer, since the soil surface was almost bare, and increased when the natural conditions were favourable for the development of the ground cover. Therefore, $NDVI$ variation reflected mostly the ground cover dynamics, which was mostly driven by the inter-rows, since the leaf area of olive tree canopies was relatively stable over the course of the year (Häusler et al., 2016). In the STSEB model, $NDVI$ was in fact used essentially to

distinguish the soil from the canopy. It is worth noting that Landsat-derived α and $NDVI$ happen to have an almost opposite time pattern, although α correlates more with ET_a .

Multiple linear regression analysis of the data in Fig. 4a was performed to understand if a combination of variables could describe the ET_a values. The most important individual variable was α , followed by T_{rad} , leading to a small increase of the goodness-of-fit from $R^2 = 0.49$ to $R^2 = 0.54$. The inclusion, however, of $NDVI$ did not improve the model significantly ($p = 0.5205$). This is further evidence that the STSEB model made better use of Landsat-derived data than a multiple regression model.

4. Discussion

4.1. Instantaneous ET_a

At the olive orchard LE fluxes showed the largest error in relation to the other energy heat fluxes (18%) and were overestimated, on average. However, the errors for R_n (−3%), H (4%) and G (−1%) were rather small. Sánchez et al. (2015a) reported relative errors of 4%, 40%, 14%, and 40% for R_n , G , H , and LE , respectively, at a burnt forest area during the satellite overpass. With the exception of G , this tendency agrees with our results, applying a similar version of the STSEB model and comparing its estimates to EC measurements. In another study the energy heat fluxes were estimated from a two-layer model and compared to instantaneous values from EC measurements at an olive orchard (Ortega-Farías et al., 2016). They reported a rather small error of G (2%), which agrees with our findings. R_n and H were generally both underestimated by around 5%, while our observations resulted in an underestimation of R_n , and an overestimation of H . The largest error was determined for LE (7%), a constant overestimation, which is in agreement with our results. Nevertheless, in our case study LE had a larger deviation mainly due to the first observation date (23 May, DoY

Table 4

Estimations of total ET_a before and after the application of the beta-factor correction. Absolute values and difference between ET_a (mm day^{-1}) from EC method and the estimates from the STSEB model are listed. RMSE is the root mean square error. The linear regression (slope of 0.95, $R^2 = 0.90$) between ground measurements and estimated ET_a , indicated a good correlation even before the beta-factor correction. The beta-factor is the combined factor of systematic error correction in satellite-derived LE , which was applied according to Van Niel et al. (2011). On DoY 255 (stress period from 3 August to 15 September, 2011) the measured ET_a (main plot 1) does not apply to Subplots 2 and 3.

Date (DoY)	Measured (EC)	Estimated (Model)			Subplot 2		Subplot 3		beta-factor
		Before	RMSE	After	Before	After	Before	After	
23 May(143)	3.5	3.6	0.08	3.7	3.4	3.5	3.3	3.3	1.02
24 Jun (175)	4.1	4.0	0.18	4.2	3.6	3.8	3.7	3.9	1.05
26 Jul (207)	4.4	3.8	0.20	4.5	3.4	4.1	3.4	4.1	1.19
12 Sep (255)	3.3	3.2	0.10	3.2	2.9	2.9	3.4	3.4	1.00
30 Oct (303)	1.8	1.7	0.05	1.9	1.3	1.4	1.4	1.5	1.06

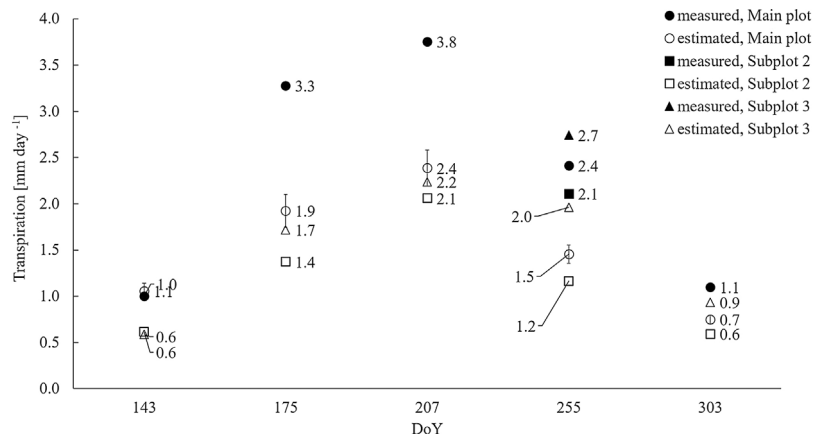


Fig. 3. Comparison between measured and estimated transpiration of the main plot and the subplots. The standard deviation of the 3 × 3 pixels extracted at the main plot (model estimates) is indicated by error bars.

Table 5
Comparison between daily measured and modeled LE_s (Tezza, 2014) with the estimated data from the STSEB model.

Date (DoY)	Measured and modeled LE_s (mm day ⁻¹)	Estimated (STSEB) LE_s (mm day ⁻¹)	Absolute Difference (mm day ⁻¹)
23 May(143)	2.5	2.3	-0.2
24 Jun (175)	0.8	1.9	1.1
26 Jul (207)	0.7	1.5	0.8
12 Sep (255)	0.8	1.3	0.5
30 Oct (303)	0.7	0.8	0.1

143), when LE was overestimated by 54 W m^{-2} due to the underestimation of P_v . In order to estimate T_v and T_s , the radiometric surface temperature T_{rad} was plotted against the partial vegetation cover P_v (described in Section 2.3). This relationship depends on soil moisture and surface emissivity (Carlson, 2007; Yang et al., 2015b; Kasim and Usman, 2016). Between 16 and 23 of May there were several rain events with a total of 42.7 mm, moistening and darkening the soil, and thus influencing the reflectance on DoY 143. On this day, $NDVI_s$ was significantly higher compared to the other days (Table 1), and consequently decreased the estimate of P_v . This variable is calculated from the vegetation index $NDVI$ (Eq. (A.5)) and the coefficient K (A.6), both retrieved from the bands B_4 and B_3 . Thus, T_v was higher, leading to an overestimation of LE .

4.2. Daily ET_a

In our case study, the model estimates for daily ET_a had the tendency to be underestimated (maximum underestimation of -0.6 mm day^{-1}) before and to be slightly overestimated (maximum overestimation of 0.2 mm day^{-1}) after the beta-factor correction (Table 4). A tendency of underestimating ET_a in TSEB models was also reported by Sánchez et al. (2015b) and Kustas et al. (2013), while Ortega-Farías and López-Olivari (2012) stated an overestimation of ET_a , depending on the phenological stage of the crop, plant moisture, and temperature stress (Zhuang and Wu, 2015). Pôças et al. (2014) stated a maximum overestimation of 0.8 mm day^{-1} . The study by Pôças et al. (2014) was conducted at a super-intensive olive grove not far from our site (75 km), applying the EF method to obtain daily values for (partly) the same dates and Landsat imagery, in 2011. In their study, ET_a was estimated using a one-source energy balance model (Mapping Evapotranspiration at high Resolution using Internalised Calibration, METRIC) and the surface energy balance fluxes were compared to ground measurements (EC method). They reported a mean bias of 12.6% between measured

and estimated daily ET_a . This is much higher than in our study where the mean bias was $< 5\%$, thus, indicating better results for heterogeneous vegetation surfaces when a two-source energy balance model is used.

4.3. Evaporation/transpiration partitioning

As stated in Section 3.3 for Subplots 2 and 3, differences of more than 1.4 mm day^{-1} were reported. Colaizzi et al. (2014) reported much smaller discrepancies of 0.79 mm day^{-1} for LE_s and 0.76 mm day^{-1} of LE_v in a fully irrigated cotton field, at Bushland, Texas, using a TSEB model to estimate the components of ET_a for different time intervals. One reason could be the difference in P_v : Subplots 2 and 3 had much lower P_v values than the main plot (P_v differences of 0.2, data not shown), which implies reduced canopy fraction. Ortega-Farías et al. (2016) and Ortega-Farías and López-Olivari (2012) stated that canopy training systems and their associated canopy geometry may significantly affect the partitioning into the energy heat flux densities. Another possible explanation would be that the thermal band has a lower spatial resolution of 120 m as compared to the other bands with a spatial resolution of 30 m. Therefore, the T_{rad} for a pixel of a higher resolution than 120 m might not yield the actual surface temperature, and result in errors calculating ET_a . Uncertainties in temperature of 1 K (T_a , T_v , and T_s) have the greatest impact on STSEB flux estimates, and result in errors of up to 30% in LE (Sánchez et al., 2008b).

The systematic underestimation of LE_v and overestimation of LE_s might not only be related to the STSEB model itself, but also to the retrieval of the daily values by the use of the EF constant method. This method assumes diurnal self-preservation of ET_a , which is often not the case, as shown by Lhomme and Elguero (1999) among other authors. Gentine et al. (2007) have investigated the EF principle for ET_a , LE_s and LE_v separately. That study showed that the soil component of EF can be assumed to be constant. Here, we have applied the beta-factor correction also to EF_s , which might have partly contributed to the overestimation of LE_s , as the multiplication factors were larger than one (Table 4).

4.4. Time series analysis of remote sensing data

So far, our analysis has focused on each date at a time, which we now extend by a brief description of the temporal pattern of our variables. To that end, we have analysed a denser time series of the major Landsat-derived variables ($NDVI$, α , T_{rad}) of the STSEB model. Fig. 4b depicts those Landsat 5–7 responses and relates them to ET_a . It suggests that the overall ground cover dynamics of the study area is driven by the heterogeneity of the olive grove at the Landsat spatial resolution scale, with both, canopies and inter-rows land cover, affecting the

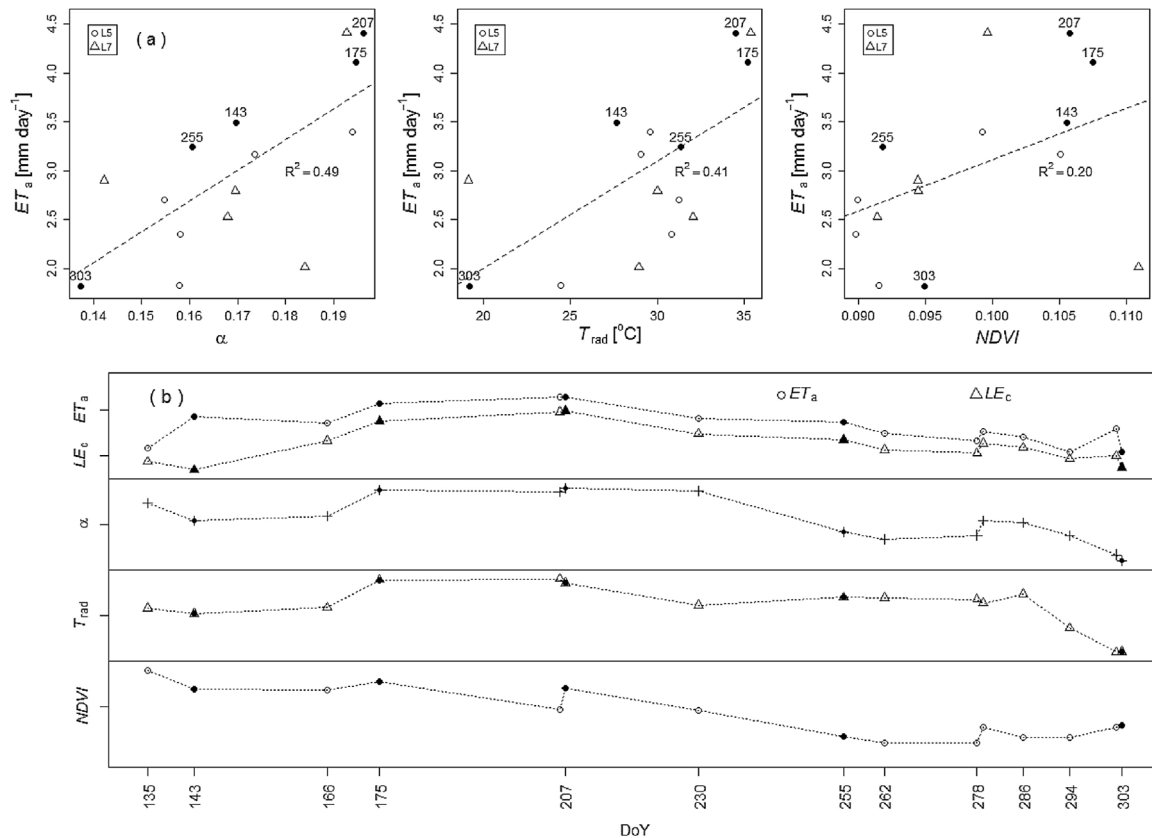


Fig. 4. Relation between Landsat-derived α , T_{rad} , and NDVI and in-situ measurements of evapotranspiration for 15 observations in 2011. The top figures indicate the relation between each Landsat variable – L5-TM and L7-ETM+ – and crop evapotranspiration (ET_a). The top center figure depicts TOA brightness temperature, available from Landsat Climate Data Record. The lower figure depicts the same observations along time, and includes also measured transpiration values. The five observations discussed in the previous sections are depicted in solid, with the respective date.

signal. This explains the positive correlation found between α and ET_a , which is contrary to Eq. (A.2) (if ET_a was proportional to R_n), but is a result of the combined effect of the dry and hot summer conditions over both components of the system (irrigated plants and increasing drier soil in between plant rows). Moreover, Fig. 4b confirms that the dates that were used as inputs of the STSEB model are in fact representative of the observations along the year.

5. Conclusions

Instantaneous and daily energy heat flux densities, and subsequently ET_a , were estimated for an intensive and deficit-irrigated olive grove in the region of Alentejo, Portugal. The performance of a STSEB model was tested, and the possibility of partitioning evapotranspiration into its components (LE_v and LE_s) was investigated by comparing its estimates with on-site measurements.

- i The results show good agreement between measured and estimated R_n , G , H , and LE for instantaneous values on crop trees which have a relatively stable phenology over the course of the year.
- ii The maximum difference recorded between modeled and measured daily ET_a was -0.6 mm day^{-1} (with a RMSE of 0.2) before, and 0.2 mm day^{-1} after applying a correction factor, which is in agreement with other studies.
- iii After beta-factor correction the partitioning of evapotranspiration into its contributing parts showed a maximum underestimation of 1.4 mm day^{-1} for LE_v and a maximum overestimation of 1.1 mm day^{-1} for LE_s at the main plot.
- iv Although satellite data with resolution of 30 m (reflectance) and 120 m (temperature) was poorly correlated with measured ET_a and LE_v

(R^2 approximately 0.5), which is not surprising due to the heterogeneity of the land cover in one pixel, the STSEB model was able to obtain refined estimates for stress conditions that fit the estimates from ground measurements.

In conclusion, these results add to those previously reported in the literature, resulting in an under- and overestimation of daily values of LE_v and LE_s , respectively, which were retrieved by applying the EF method and the beta-factor correction. Nevertheless, the remote sensing based application of the STSEB model showed a good performance in the estimation of instantaneous and daily ET_a from medium-resolution satellite images, and is therefore useful for irrigation management to optimize crop production in relation to agricultural water use.

Funding

This work was supported within the framework of the PhD research grants attributed by FCT (Fundação para a Ciência e a Tecnologia I.P.) to Melanie Häusler (PD/BD/52698/2014) and Nuno Conceição (SFRH/BD /66967/2009). The field work was financed by the project WUSS-IAAME – Water Use, Survival Strategies and Impact of Agrochemicals in Agricultural Mediterranean Ecosystems (PTDC/AAC-AMB/100635/2008, FCT Portugal), and a small part co-financed by the project TELERIEG – Uso de la teledetección para a recomendación y seguimiento de las prácticas de riego en el espacio SUDOE (SOE1/P2/E082) in the framework of the research activities of the research unit LEAF and the Department of Biosystems Eng., at the Instituto Superior de Agronomia, Universidade de Lisboa. CEF is a research unit funded by FCT, Portugal (UID/AGR/00239/2013).

Acknowledgments

The authors are grateful to the engineers and students who contributed to this project, especially to Soroor Amindezfouli, and Sónia Lourenço, who partly contributed to the on-site data collection on plant

water status. We are thankful to landowners and workers at Monte do Pardieiro. For their technical support, and fruitful discussions, we would like to thank Prof. José M. C. Pereira, Dr. João P. Nunes, Dr. Yufang Ye, Akli Benali, and Dr. Johannes Michaelsen.

Appendix A. Summary of STSEB approach

The energy balance equation is:

$$R_n = H + LE + G \tag{A.1}$$

where R_n is the net radiation ($W m^{-2}$), H the sensible heat flux ($W m^{-2}$), LE the latent heat flux ($W m^{-2}$) and G the soil heat flux ($W m^{-2}$).

The R_n was estimated from the albedo α , the global solar radiation S ($W m^{-2}$), the incident long-wave radiation L_{sky} ($W m^{-2}$), the total emissivity ϵ , the Stefan-Boltzmann constant σ ($5.67 \times 10^{-8}, W m^{-2} K^{-4}$), and the radiometric land surface temperature T_{rad} :

$$R_n = (1 - \alpha)S + \epsilon L_{sky} - \epsilon \sigma T_{rad}^4 \tag{A.2}$$

The value of α is given by the equation of Dubayah (1992), using Landsat imagery, where the visible, near-, and short-wave infrared bands ($B_1 - B_7$) contribute to the total α by weighing the bands with a corresponding factor (assuming Lambertian surface):

$$\alpha = 0.221B_1 + 0.162B_2 + 0.102B_3 + 0.354B_4 + 0.059B_5 + 0.0195B_7 \tag{A.3}$$

The emissivity components for canopy ϵ_c and soil ϵ_s were established on the basis of vegetation characterizations and their emissivities using the equation suggested by Rubio et al. (1997). Values of $\epsilon_c = 0.987$, and $\epsilon_s = 0.965$ were adopted for this research. The surface emissivity was estimated using the equation proposed by Valor and Caselles (2005), taking into account the partial vegetation cover P_v and the emissivity components ϵ_c and ϵ_s :

$$\epsilon = \epsilon_c P_v + \epsilon_s (1 - P_v)(1 - 1.74P_v) + 1.7372P_v(1 - P_v) \tag{A.4}$$

The estimation of P_v is based on the Normalized Difference Vegetation Index $NDVI$ and the coefficient K both retrieved from the Landsat surface reflectance bands B_4 and B_3 :

$$NDVI = \frac{B_4 - B_3}{B_4 + B_3} \tag{A.5}$$

$$K = \frac{B_{4v} - B_{3v}}{B_{4s} + B_{3s}} \tag{A.6}$$

To obtain T_{rad} from a single thermal band, different approaches such as the mono-channel algorithm (Qin et al., 2001) or the single-channel algorithm (Jiménez-Muñoz, 2003), based on the radiative-transfer equation, were developed. Here, in-situ radio-sounding data estimated by 4.0 MODTRAN code (Berk, 1999; Barsi et al., 2003) were used and introduced in the following equation:

$$L_{sen} = [\epsilon B(T_{rad}) + (1 - \epsilon)L_{atm}^\downarrow] \tau + L_{atm}^\uparrow \tag{A.7}$$

where L_{sen} is the Top of Atmosphere (TOA) radiance, i.e. the radiance measured by the sensor, ϵ is the emissivity of the land surface, $B(T_{rad})$ is the radiance of a black body given by Planck's Law, τ is the total atmospheric transmissivity, L_{atm}^\downarrow is the atmospheric down-welling, and L_{atm}^\uparrow the atmospheric up-welling spectral irradiance (Table A.1). After correcting the radiance for atmospheric and emissivity effects, T_{rad} was obtained.

In the STSEB approach, proposed by Sánchez et al. (2008b), the total sensible heat flux H is obtained by dividing the surface into canopy and soil contributions, H_v and H_s , respectively:

$$H = P_v H_v + (1 - P_v) H_s \tag{A.8}$$

$$H_v = \rho C_p \frac{T_v - T_a}{r_a^h} \tag{A.9}$$

$$H_s = \rho C_p \frac{T_s - T_a}{r_a^a + r_a^s} \tag{A.10}$$

where ρC_p is the volumetric heat capacity of air at constant pressure ($J K^{-1} m^{-3}$). The estimation of the aerodynamic resistances r_a for stable and unstable conditions used for this work are based on the general framework described in Norman et al. (1995), and Li et al. (2005) and adapted according to Brutsaert (1999). A summary of the expressions to estimate these resistances is given by Sánchez et al. (2008b).

Table A.1

Atmospheric parameters (transmissivity, up- and down-welling sky irradiance) estimated from 4.0 MODTRAN (Berk, 1999), as well as incident-longwave radiation L_{atm} and global solar radiation S at the time of satellite overpass.

Image (L5-TM)	τ	L_{atm}^\uparrow ($W m^{-2} sr^{-1} \mu m^{-1}$)	L_{atm}^\downarrow ($W m^{-2} sr^{-1} \mu m^{-1}$)	L_{sky} ($W m^{-2}$)	S ($W m^{-2}$)
23 May 2011	0.71	2.22	3.60	371	910
24 Jun 2011	0.85	1.18	1.99	339	934
26 Jul 2011	0.76	2.05	3.35	375	884
12 Sep 2011	0.80	1.68	2.73	347	796
30 Oct 2011	0.73	2.01	3.19	328	574

The instantaneous soil heat flux G is given by:

$$G = C_G(1 - P_v)R_n \quad (\text{A.11})$$

where C_G is the ratio of G/R_n when field measurements were around 0.3 for the period of time considered in 2011 (Conceição et al., 2017), and P_v is the partial vegetation cover.

References

- Agam, N., Kustas, W.P., Anderson, M.C., Norman, J.M., Colaizzi, P.D., Howell, T.A., Prueger, J.H., Meyers, T.P., Wilson, T.B., 2010. Application of the Priestley-Taylor approach in a two-source surface energy balance model. *J. Hydrometeorol.* 11 (1), 185–198.
- Allen, R.G., Pereira, L.S., Raes, D., Smith, M., 1998. FAO Irrigation and Drainage Paper No. 56, Crop Evapotranspiration (Guidelines for Computing Crop Water Requirements). Rome, Italy.
- Barsi, J., Barker, J., Schott, J., 2003. An atmospheric correction parameter calculator for a single thermal band earth-sensing instrument. IGARSS 2003. 2003 IEEE Int. Geosci. and Rem. Sen. Symp. Proceedings (IEEE Cat. No.03CH37477), vol. 5. IEEE, Toulouse, pp. 3014–3016.
- Bastiaanssen, W., Pelgrum, H., Wang, J., Ma, Y., Moreno, J., Roerink, G., van der Wal, T., 1998. A remote sensing surface energy balance algorithm for land (SEBAL). *J. Hydrol.* 212–213, 213–229.
- Berk, A., 1999. MODTRAN4 radiative transfer modeling for atmospheric correction. *Proc. SPIE* 3756 (1993), 348–353.
- Brutsaert, W., 1999. Aspects of bulk atmospheric boundary layer similarity under free-convective conditions. *Rev. Geophys.* 37 (4), 439–451.
- Cammalleri, C., Anderson, M., Ciraolo, G., D'Urso, G., Kustas, W., La Loggia, G., Minacapilli, M., 2012. Applications of a remote sensing-based two-source energy balance algorithm for mapping surface fluxes without in situ air temperature observations. *Remote Sens. Environ.* 124, 502–515.
- Carlson, T., 2007. An overview of the “triangle method” for estimating surface evapotranspiration and soil moisture from satellite imagery. *Sensors* 7 (8), 1612–1629.
- Choudhury, B.J., Idso, S.B., Reginato, R.J., 1987. Analysis of an empirical model for soil heat flux under a growing wheat crop for estimating evaporation by an infrared-temperature based energy balance equation. *Agric. For. Meteorol.* 39 (April (4)), 283–297.
- Colaizzi, P.D., Agam, N., Tolk, J.A., Evett, S.R., Howell, T.A., Gowda, P.H., O'Shaughnessy, S.A., Kustas, W.P., Anderson, M.C., 2014. Two-source energy balance model to calculate ET, and ET: comparison of Priestley-Taylor and Penman-Monteith formulations and two time scaling methods. *Trans. ASABE* 57 (2), 479–498.
- Colaizzi, P.D., Agam, N., Tolk, J.A., Evett, S.R., Howell, T.A., O'Shaughnessy, S.A., Gowda, P.H., Kustas, W.P., Anderson, M.C., 2016. Advances in a two-source energy balance model: partitioning of evaporation and transpiration for cotton. *Trans. ASABE* 59 (1), 181–197.
- Conceição, N., Tezza, L., Häusler, M., Lourenço, S., Pacheco, C.A., Ferreira, M.I., 2017. Three years of monitoring evapotranspiration components and crop and stress coefficients in a deficit irrigated intensive olive orchard. *Agric. Water Manage.* 191, 138–152.
- Du, J., Song, K., Wang, Z., Zhang, B., Liu, D., 2013. Evapotranspiration estimation based on MODIS products and surface energy balance algorithms for land (SEBAL) model in Sanjiang Plain, Northeast China. *Chin. Geogr. Sci.* 23 (1), 73–91.
- Dubayah, R., 1992. Estimating net solar radiation using Landsat Thematic Mapper and digital elevation data. *Water Resour. Res.* 28 (9), 2469–2484.
- Dytham, C., 2011. *Choosing and Using Statistics: A Biologist's Guide*, 3rd ed. Wiley-Blackwell.
- Fernandes-Silva, A.F.F., 2008. *Necessidades Hídricas e Resposta da Oliveira (Olea europea L.) ao Deficit Hídrico na Região da Terra Quente*. Universidade Trás-os-Montes e Alto Douro, Vila Real, Portugal (Ph.D. thesis).
- Ferreira, M.I., Conceição, N., Pacheco, C.A., Häusler, M., 2012a. Análise de indicadores de desconforto hídrico durante ciclos de stress num olival intensivo no Alentejo. In: *VI Actas do Simpósio Nacional de Olivicultura*. Mirandela, pp. 207–2015.
- Ferreira, M.I., Silvestre, J., Conceição, N., Malheiro, A.C., 2012b. Crop and stress coefficients in rainfed and deficit irrigation vineyards using sap flow techniques. *Irrig. Sci.* 30 (5), 433–447.
- Food and Agriculture Organization of the United Nations (FAO), 2006. *AQUASTAT online database*. <http://www.fao.org/nr/aboutnr/nr/en/>.
- Gentine, P., Entekhabi, D., Chehbouni, A., Boulet, G., Duchemin, B., 2007. Analysis of evaporative fraction diurnal behaviour. *Agric. For. Manage.* 143 (1–2), 13–29.
- Granier, A., 1985. Une nouvelle méthode pour la mesure du flux de sève brute dans le tronc des arbres. *Annales des Sciences Forestières* 42 (2), 193–200.
- Häusler, M., Ferreira, M.I., Conceição, N., 2014. Assessment of vegetation parameters in olive trees in the region of Alentejo: a comparison of direct and indirect methods. *Acta Hort.* 1038, 407–414.
- Häusler, M., Silva, J.M.N., Cerasoli, S., López-Saldaña, G., Pereira, J.M.C., 2016. Modelling spectral reflectance of open cork oak woodland: a simulation analysis of the effects of vegetation structure and background. *Int. J. Remote Sens.* 37 (3), 492–515.
- Hoffmann, H., Nieto, H., Jensen, R., Guzinski, R., Zarco-Tejada, P., Friborg, T., 2016. Estimating evaporation with thermal UAV data and two-source energy balance models. *Hydrol. Earth Syst. Sci.* 20 (2), 697–713.
- Humes, K., Hardy, R., Kustas, W., Prueger, J., Starks, P., 2004. April. High spatial resolution mapping of surface energy balance components with remotely sensed data. *Thermal Remote Sensing in Land Surface Processing*. CRC Press, New York, pp. 110–132 (Chapter 3).
- Jiménez-Muñoz, J.C., 2003. A generalized single-channel method for retrieving land surface temperature from remote sensing data. *J. Geophys. Res.* 108 (D22), 4688.
- Kasim, A.A., Usman, A.A., 2016. Triangle method for estimating soil surface wetness from satellite imagery in Allahabad District, Uttar Pradesh, India. *J. Geosci. Environ. Prot.* 4 (January), 84–92.
- Kustas, W.P., Alfieri, J.G., Anderson, M.C., Colaizzi, P.D., Prueger, J.H., Evett, S.R., Neale, C.M., French, A.N., Hipps, L.E., Chávez, J.L., Copeland, K.S., Howell, T.A., 2012. Evaluating the two-source energy balance model using local thermal and surface flux observations in a strongly advective irrigated agricultural area. *Adv. Water Res.* 50, 120–133.
- Kustas, W.P., Anderson, M.C., Cammalleri, C., Alfieri, J.G., 2013. Utility of a thermal-based two-source energy balance model for estimating surface fluxes over complex landscapes. *Proc. Environ. Sci.* 19, 224–230.
- Lhomme, J.P., Elguero, E., 1999. Examination of evaporative fraction diurnal behaviour using a soil-vegetation model coupled with a mixed-layer model. *Hydrol. Earth Syst. Sci.* 3 (2), 259–270.
- Li, F., Kustas, W.P., Prueger, J.H., Neale, C.M.U., Jackson, T.J., 2005. Utility of remote sensing based two-source energy balance model under low and high vegetation cover conditions. *J. Hydrometeorol.* 6, 878–891.
- Minacapilli, M., Consoli, S., Vanella, D., Ciraolo, G., Motisi, A., 2016. A time domain triangle method approach to estimate actual evapotranspiration: application in a Mediterranean region using MODIS and MSG-SEVIRI products. *Remote Sens. Environ.* 174, 10–23.
- Nishida, K., Nemani, R.R., Glassy, J.M., Running, S.W., 2003a. Development of an evapotranspiration index from Aqua/MODIS for monitoring surface moisture status. *IEEE Trans. Geosci. Remote Sens.* 41 (2 Pt 1), 493–500.
- Nishida, K., Nemani, R.R., Running, S.W., Glassy, J.M., 2003b. An operational remote sensing algorithm of land surface evaporation. *J. Geophys. Res.* 108 (D9), 4270.
- Norman, J.M., Kustas, W., Humes, K., 1995. A two-source approach for estimating soil and vegetation energy fluxes from observations of directional radiometric surface temperature. *Agric. For. Meteorol.* 77, 263–293.
- Ortega-Farías, S., López-Olivari, R., 2012. Validation of a two-layer model to estimate latent heat flux and evapotranspiration in a drip-irrigated Olive Orchard. *Trans. ASABE* 55 (4), 1169–1178.
- Ortega-Farías, S., Ortega-Salazar, S., Poblete, T., Kilic, A., Allen, R., Poblete-Echeverría, C., Ahumada-Orellana, L., Zuñiga, M., Sepúlveda, D., 2016. Estimation of energy balance components over a drip-irrigated olive orchard using thermal and multi-spectral cameras placed on a helicopter-based unmanned aerial vehicle (UAV). *Remote Sens.* 8 (8), 638.
- Peng, J., Liu, Y., Zhao, X., Loew, A., 2012. Estimation of evapotranspiration from TOA radiances in the Poyang Lake Basin, China. *Hydrol. Earth Syst. Sci. Discuss.* 9 (9), 10963–11003.
- Pôças, I., Paço, T.A., Cunha, M., Andrade, J.A., Silvestre, J., Sousa, A., Santos, F.L., Pereira, L.S., Allen, R.G., 2014. Satellite-based evapotranspiration of a super-intensive olive orchard: application of METRIC algorithms. *Biosyst. Eng.* 128, 1–13.
- Qin, Z., Karnieli, A., Berliner, P., 2001. A mono-window algorithm for retrieving land surface temperature from Landsat TM data and its application to the Israel-Egypt border region. *Int. J. Remote Sens.* 22 (18), 3719–3746.
- Roerink, G.J., Su, Z., Menenti, M., 2000. S-SEBI: a simple remote sensing algorithm to estimate the surface energy balance. *Phys. Chem. Earth B: Hydrol. Oceans Atmos.* 25 (2), 147–157.
- Ruan, Z., Jia, L., Menenti, M., 2014. Evaluation of algorithms to estimate daily evapotranspiration from instantaneous measurements under all-sky conditions. *IOP Conference Series: Earth and Env. Sci.* 17 012133.
- Rubel, F., Kottek, M., 2010. Observed and projected climate shifts 1901–2100 depicted by world maps of the Köppen-Geiger climate classification. *Meteorologische Zeitschrift* 19 (April (2)), 135–141.
- Rubio, E., Caselles, V., Badenas, C., 1997. Emissivity measurements of several soils and vegetation types in the 8–4 μm wave band: analysis of two field methods. *Remote Sens. Environ.* 59, 490–521.
- Ruhoff, L., Paz, R., Aragao, L.E.O.C., Mu, Q., Malhi, Y., Collischonn, W., Rocha, H.R., Running, S.W., 2013. Assessment of the MODIS global evapotranspiration algorithm using eddy covariance measurements and hydrological modelling in the Rio Grande basin. *Hydrol. Sci. J.* 58 (8), 1658–1676.
- Sánchez, J., Scavone, G., Caselles, V., Valor, E., Copertino, V., Telesca, V., 2008a. Monitoring daily evapotranspiration at a regional scale from Landsat-TM and ETM+ data: application to the Basilicata region. *J. Hydrol.* 351 (March (1–2)), 58–70.
- Sánchez, J.M., Bisquert, M., Rubio, E., Caselles, V., 2015a. Impact of land cover change induced by a fire event on the surface energy fluxes derived from remote sensing. *Remote Sens.* 7 (11), 14899–14915.
- Sánchez, J.M., Kustas, W.P., Caselles, V., Anderson, M.C., 2008b. Modelling surface energy fluxes over maize using a two-source patch model and radiometric soil and canopy temperature observations. *Remote Sens. Environ.* 112 (3), 1130–1143.
- Sánchez, J.M., López-Urrea, R., Doña, C., Caselles, V., González-Piqueras, J., Nicolòs, R., 2015b. Modeling evapotranspiration in a spring wheat from thermal radiometry: crop

- coefficients and E/T partitioning. *Irrig. Sci.* 33 (6), 399–410.
- Schuepp, P.H., Leclerc, M.Y., MacPherson, J.I., Desjardins, R.L., 1990. Footprint prediction of scalar fluxes from analytical solutions of the diffusion equation. *Boundary-Layer Meteorol.* 50 (1–4), 355–373.
- Sobrino, J.A., Jiménez-Muñoz, J.C., Paolini, L., 2004. Land surface temperature retrieval from LANDSAT TM 5. *Remote Sens. Environ.* 90 (4), 434–440.
- Sun, Z., Gebremichael, M., Ardö, J., Nickless, A., Caquet, B., Merboldh, L., Kutschi, W., 2012. Estimation of daily evapotranspiration over Africa using MODIS/Terra and SEVIRI/MSG data. *Atmos. Res.* 112 (August), 35–44.
- Tanner, B.D., Swiatek, E., Greene, J.P., 1993. Density fluctuations and use of the krypton hygrometer in surface flux measurements. In: *Engineers A. S. o. C (Ed.), Proceeding of the 1993 National Conference on Irrigation and Drainage Engineering Irrigation and Drainage Division*. Park City.
- Tasumi, M., Trezza, R., Allen, R.G., Wright, J.L., 2005. Operational aspects of satellite-based energy balance models for irrigated crops in the semi-arid U.S. *Irrig. Drain. Syst.* 19 (3–4), 355–376.
- Tezza, L., 2014. Misura e stima dell'evaporazione dal suolo in oliveto nella regione dell'Alentejo, Portogallo. Università degli studi di Padova (Ph.D. thesis).
- Timmermans, W.J., Kustas, W.P., Anderson, M.C., French, A.N., 2007. An inter-comparison of the Surface Energy Balance Algorithm for Land (SEBAL) and the Two-Source Energy Balance (TSEB) modeling schemes. *Remote Sens. Environ.* 108 (4), 369–384.
- Valor, E., Caselles, V., 1996. Mapping land surface emissivity from NDVI. Application to European, African and South-American areas. *Remote Sens. Environ.* 57, 167–184.
- Valor, E., Caselles, V., 2005. Validation of the Vegetation Cover Method for Land Surface Emissivity Estimation. Research Signpost, Kerala.
- Van Niel, T.G., McVicar, T.R., Roderick, M.L., van Dijk, A.I.J.M., Renzullo, L.J., van Gorsel, E., 2011. Correcting for systematic error in satellite-derived latent heat flux due to assumptions in temporal scaling: assessment from flux tower observations. *J. Hydrol.* 409 (1–2), 140–148.
- Webb, E.K., Pearman, G.I., Leuning, R., 1980. Correction of flux measurements for density effects due to heat and water vapour transfer. *Q. J. R. Meteorol. Soc.* 106 (447), 85–100.
- Yang, Y., Long, D., Guan, H., Liang, W., Simmons, C., Batelaan, O., 2015a. Comparison of three dual-source remote sensing evapotranspiration models during the MUSOEXE-12 campaign: revisit of model physics. *Water Resour. Res.* 51 (5), 3145–3165.
- Yang, Y., Su, H., Zhang, R., Tian, J., Li, L., 2015b. An enhanced two-source evapotranspiration model for land (ETEML): algorithm and evaluation. *Remote Sens. Environ.* 168, 54–65.
- Zhuang, Q., Wu, B., 2015. Estimating evapotranspiration from an improved two-source energy balance model using ASTER satellite imagery. *Water* 7 (12), 6673–6688.

Web references

- [1] Wikimedia Commons (January 6, 2007). Map of the climatic regions of Portugal according to the Köppen-Geiger climate classification system. IPMA. https://commons.wikimedia.org/wiki/File:Map_of_the_climatic_regions_of_Portugal.jpg [November 16, 2016].
- [2] Google earth V 7.1.7.2606. (May 26, 2013). Alentejo, Portugal. 38° 1.34' N, 8° 10.84' W, Eye alt 788 m. SIO, NOAA, U.S. Navy, NGA, GEBCO. Image Landsat, DigitalGlobe 2016. <http://www.earth.google.com> [November 14, 2016].

Assessment of the indirect impact of wildfire (severity) on actual evapotranspiration in eucalyptus forest based on the surface energy balance estimated from remote sensing techniques, (Article II)

As the STSEB model can be applied over different types of vegetation, this second work profited from the results of the olive grove, and a comparison of the STSEB estimates to EC data over grassland (A). The only different and influencing variable between the study areas was the vegetation height. Sensitivity analysis of Sánchez et al. (2008b, 2009) showed that the height has only a small impact on the output of the energy heat fluxes and evapotranspiration. Within this work the influence of tree and shrub height on evapotranspiration was tested, using data from fire-affected areas and different satellite platforms. The results of the sensitivity analysis are provided in the section of Supplemental material B.









Here, the STSEB model was applied to a fire-affected area with eucalypt stands, to estimate ET_a and its components of transpiration and evaporation. Differences for the estimates of the model, between burnt and unburnt areas, were determined. The time of recovery of ET_a and its components to conditions before the fire was estimated, where the severity of the fire had a strong impact.

This chapter was originally published in *International Journal of Remote Sensing*, 8 April 2018, ©Informa UK Limited, trading as Taylor & Francis Group, available online: <https://doi.org/10.1080/01431161.2018.1460508>. This journal was rated with an impact factor of 1.724 in 2016.

Melanie Häusler, João P. Nunes, Paula Soares, Juan M. Sánchez, João M. N. Silva, Thorsten Warneke, Jan Jacob Keizer, and José M. C. Pereira.



Assessment of the indirect impact of wildfire (severity) on actual evapotranspiration in eucalyptus forest based on the surface energy balance estimated from remote-sensing techniques

Melanie Häusler ^a, João P. Nunes ^b, Paula Soares ^a, Juan M. Sánchez ^c,
João M. N. Silva ^a, Thorsten Warneke ^d, Jan Jacob Keizer ^e and José M. C. Pereira ^a

^aForest Research Centre, School of Agriculture, University of Lisbon, Tapada da Ajuda, Lisbon, Portugal; ^bCE3C Centre for Ecology, Evolution and Environmental Changes, Faculdade de Ciências, Universidade de Lisboa, Lisboa, Portugal; ^cIDR, Regional Development Institute, Applied Physics Department, University of Castilla-La Mancha, Albacete, Spain; ^dInstitute of Environmental Physics, University of Bremen, Bremen, Germany; ^eCESAM, Centre for Environmental and Marine Studies, Department of Environment and Planning, University of Aveiro, Aveiro, Portugal

ABSTRACT

Wildfires have a strong impact on the environment, changing its structure, soil properties, and microclimate and subsequently its water cycle with implications on the surface energy fluxes. Persisting droughts and catastrophic forest fires initiated this case study of pure eucalyptus stands in north-central Portugal. Although many studies have investigated changes in actual evapotranspiration (ET_a), surface energy flux patterns, and the related physical parameters, only a few concentrated on the fire-driven changes in pure eucalyptus stands in the Mediterranean climate. This study aims to understand the consequences of wildfires on the water cycle, namely the ET_a , and the surface energy heat fluxes by applying a simplified two-source energy balance model in combination with medium-resolution imagery (Landsat 8). A total of 21 different burnt locations were evaluated, which burned between 2011 and 2013. Estimated surface energy fluxes and daily ET_a were compared to nearby control sites (unburnt) during satellite overpass for the time after the fire (2013–2015). The fire scars were classified into their burn severity, using the differenced Normalized Burn Ratio. The absolute difference of ET_a (ΔET_a) between unburnt and burnt locations was used to identify fire-driven changes in magnitude and its evolution over time. Our results show that for the unburnt stands, the contributions to the total latent heat flux were around 80% from the canopy and 20% from the soil, while for the burnt site the contributions were around 30% (canopy) and 70% (soil) shortly after the fire. Inter-annually, the difference in ET_a increased during the rainy season, which was related to the epicormic shooting, the fast regrowth rate of foliage, and the abundance of water. Generally, smaller differences in ET_a were related to the severity classification and stand properties (i.e. tree species and soil characteristics).

ARTICLE HISTORY

Received 14 September 2017
Accepted 21 March 2018

Two to three years after the fire events, ΔET_a became non-significant for all severity classes, leading to an impact on the total water cycle smaller in comparison to other post-fire studies.

1. Introduction

According to the 6th National Forest Inventory (ICNF 2013a), the eucalyptus tree *Eucalyptus globulus* Labill. (Tasmanian blue gum) is the most widespread tree species in Continental Portugal with 26% of the total forest cover. The wood is mainly used for pulp and paper production and its plantation is supported by the industry. In 2010, eucalyptus forests occupied 811,943-ha, corresponding to an increase in area of 13% since 1995.

The areas to where the eucalyptus species expanded are also the ones increasingly affected by wildfire. Between 2001 and 2012, almost 225,000-ha of eucalyptus were affected by wildfires (ICNF 2013b). In Europe, Portugal belongs to the southern top five most fire-affected member states according to the records between 1980 and 2008 (JRC Scientific and Technical Report 2008). A changing climate with hot and dry summers in combination with the highly flammable characteristic of eucalyptus forests (Luke and McArthur 1978; Mirra et al. 2017) promotes fire occurrences (JRC Scientific and Technical Report 2008). These lead to a partial or even complete removal of the vegetation cover and change the soil properties (Nunes et al. 2016; Hawtree et al. 2015), which in return disturb the natural water cycle and need years to recover (Whelan et al. 2015; Nolan et al. 2014; Sánchez et al. 2015). The regrowth of the biomass and its impact on the water dynamics are directly related to the severity of the fire (Nolan et al. 2014; Maia et al. 2012). The classification of burn severity is often used as a measure of changes in vegetation structure and moisture content, being also suitable to be monitored by remote sensing (Cocke, Fulé, and Crouse 2005; Escuin, Navarro, and Fernández 2008).

It is of utmost importance to understand and predict the implications of fire events for the water dynamics. The removal of vegetation by fire has direct influence on the microclimate, the precipitation, the streamflow, and subsequently the water resources for production systems and local residents. To that avail, we study the recovery of actual evapotranspiration (ET_a) in fire-affected eucalyptus stands, as well as the energy heat fluxes and their contributing parts from soil and canopy.

In the literature, many studies were carried out in forests to determine the relationship between the water dynamics and disturbances such as wind-throw (Hirano, Suzuki, and Hirata 2017), drought (Tursilowati et al. 2012; Whelan et al. 2015; David et al. 2007; Glenn et al. 2011), logging (de Almeida and Riekerk 1990; Spracklen, Arnold, and Taylor 2012; Iroumé and Palacios 2013), and wildfires (Ueyama et al. 2014; Bond-Lamberty et al. 2009; Nolan et al. 2014). Bosch and Hewlett (1982) tested the validity of generalizations about the relationship between forest cover and water yield of Hibbert (1967), by analysing a total of 94 catchment experiments worldwide. The results showed that a reduction of forest cover (e.g. clear-cut, wildfire) regularly resulted in increasing water yields independently from the tree species, with the exception of one study by Langford (1976). The latter author reported a reduction in streamflow from three to five years after the wildfire in *Eucalyptus regnans* stands. Subsequent

studies also observed this effect for other eucalyptus species in Australia (Buckley et al. 2012; Nolan et al. 2015). However, in the Portuguese Águeda watershed, Hawtree et al. (2015) analysed a time series of the long-term hydrological impact of afforestation of mainly eucalyptus and pine plantations, showing no significant change in streamflow.

The application of remote sensing-based two-source energy balance (TSEB) models has the advantage of estimating energy heat fluxes over vast areas (e.g. field-scale, regional-scale) compared to surface-based techniques. Fire effects on energy fluxes have been extensively studied in eucalyptus (Shakesby et al. 1993; Nolan et al. 2014) and other forests (Montes-Helu et al. 2009; Ueyama et al. 2014; Whelan et al. 2015; Sánchez et al. 2015), often using the ground-based eddy covariance method as reference. Its results of surface energy heat fluxes and ET_a are reliable, but, in contrast to remote sensing-based approaches, only on a local-scale for homogeneous vegetation covers directly upwind from the instruments (Ghassam 1989; Scott et al. 2000). Algorithms such as the simplified TSEB model (STSEB) allow the assumption of heterogeneous surfaces (Cristóbal et al. 2017; Sánchez et al. 2015; Du et al. 2013). Here, this two-source layer model estimates the contributing parts of soil and canopy to the total heat flux densities of net radiation (R_n), sensible heat (H), and latent heat (LE), giving additional information about their origin. Other models, such as the Terrestrial Ecosystem Process Model (Biome-BGC, Kang, Kimball, and Running 2006; Bond-Lamberty et al. 2009), make assumptions about the water dynamics also on a regional scale, using on-site measurements. A weakness of the Biome-BGC model approach might be that it does not include explicit energy balance calculation and therefore gives no information about the energy balance fluxes. This might simplify the need of input parameters, but leads to crude calculations of, for instance, the soil temperature. Furthermore, it is not designed to simulate ET_a over poorly drained areas, which is one condition of our case study.

In Portugal, only few studies have focused on the water balance of eucalyptus stands (Boulet et al. 2015; De Almeida and Riekerk 1990; Hawtree et al. 2015). To our knowledge, there is none investigating the hydrological implications of wildfires for the energy balance fluxes of H ($W\ m^{-2}$) and LE ($W\ m^{-2}$), where the latter can be directly converted into evapotranspiration ET_a ($mm\ day^{-1}$). Therefore, we applied a simplified version of the STSEB (Sánchez et al. 2008; based on Norman, Kustas, and Humes 1995), together with remotely sensed data (Landsat 8) to assess the energy flux patterns and the ET_a over fire-affected areas. This model has already been tested over a variety of different vegetation types in combination with remotely sensed data with an accuracy of $\pm 1.0\ mm\ day^{-1}$ (Häusler et al. 2018; Sánchez et al. 2008; Sánchez et al. 2007; Sánchez et al. 2009; Sánchez et al. 2011; Sánchez et al. 2015). Fire scars were classified into their burn severity. For each class, the difference between burnt and control sites of ET_a was determined to identify fire-induced changes and its evolution over time (up to four years). Stand and fire properties (i.e. distribution of vegetation to soil surface and severity of fires) were used to explain the course of the recovery by:

- (i) assessing the post-fire changes of instantaneous LE (LE_i , at the time of satellite overpass) and its contributions from canopy and soil;
- (ii) analysing the recovery of ET_a , on a daily basis, from pure eucalyptus stands after wildfires with different levels of fire severity and stand properties (i.e. greenness, partial vegetation cover).

2. Materials and methods

2.1. Study area

This study comprises a large part of the Caramulo mountain range, about 20–30 km inland from the city of Aveiro, in the north-central part of Portugal (Figure 1). According to Köppen–Geiger, the climate classification corresponds to the Csb type (Köppen 1936). The climate is humid Mediterranean, characterized by high annual precipitation (750 – 2000 mm), leading to biomass production and thereby accumulating fire fuels. The summer seasons are mild and dry, promoting wildfires.

The principal soil types are humic Cambisols and Leptosols that are derived from schist (and granite, depending on the exact site locations) with very shallow soils (down to only 20 cm). Their textures are between sandy loam and silt loam and a high stone content. The impenetrable bedrock is made of granite and schist (soil properties and compositions are given in Shakesby et al. 1993; Tavares Wahren et al. 2016).

At present, the Caramulo mountains are predominantly covered by plantations of eucalyptus (*Eucalyptus globulus* Labill.) and to a lesser extend with maritime pine (*Pinus pinaster* Ait.). The maritime pine becomes increasingly substituted by eucalyptus stands after wildfires (Forest inventory COS 2007 level 5). Generally, eucalyptus is a fast-growing tree species, with short rotation cycles of typically 10–12 years and three to four rotation cycles between planting.

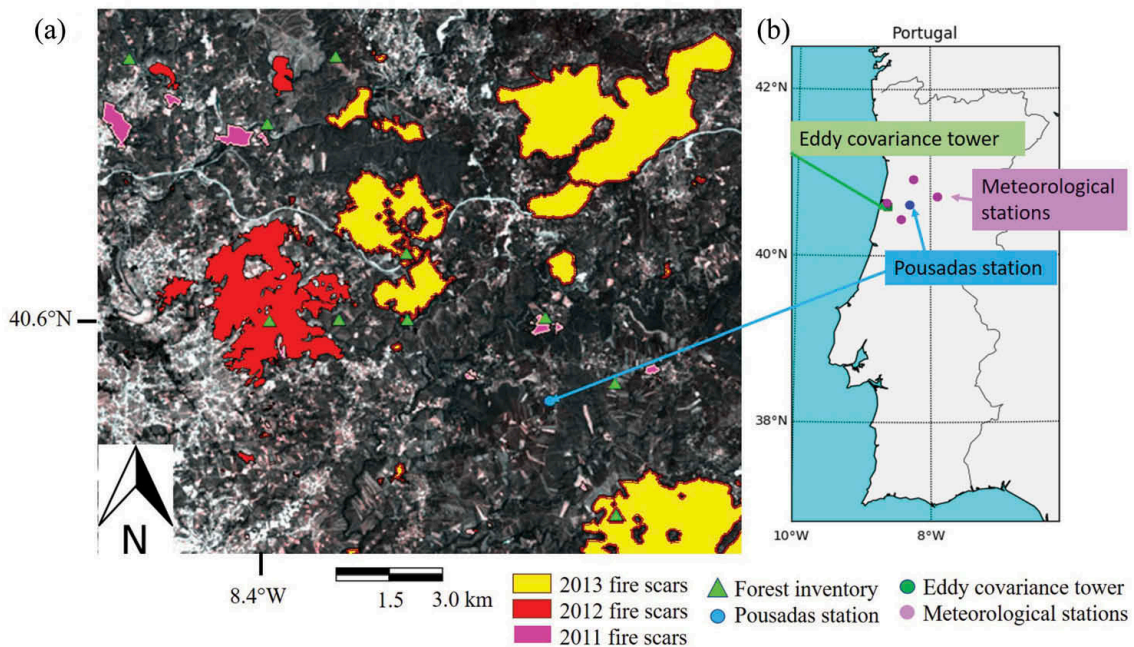


Figure 1. Yellow areas: fire scars of 2013, red areas: fire scars of 2012, and pink areas: fire scars of 2011, green triangles: forestry inventory plots, blue dot: Pousadas station, violet dots: meteorological stations, green dot: station of Aveiro/Suburban area used for validation. The meteorological station Pousadas is operated by the Department of Environment and Planning & CESAM; the other four meteorological stations are operated by the Instituto Português do Mar e da Atmosfera.

2.2. Selection of control and burnt sites

The fire scar maps were provided by the ICNF (2013a), and the areas with pure eucalyptus stands selected by overlapping with the forest inventory COS 2007, level 5 data. At the centre of our study site was the meteorological station Pousadas, where the fire scars were chosen within a radius of 15 km.

A total of 8574-ha were selected that burnt in the years 2011, 2012, and 2013 (Table 1). The burnt and control sites were selected within and immediately outside the burnt areas. For small fire scars, only one pair of control and burnt site was considered (< 50-ha), while two to five pairs were fitted into large fire scars (>800-ha) with a minimum distance of 1 km between them. The sizes ranged between 3×3 and 9×9 pixels, depending on the size of the burnt area. All sites were chosen to coincide or be as close as possible (maximum 2 km) to plots of the National Forest Inventory 2006, for which also data from the Paper Industry Portuguese Association (CELPA, measurements from 2007 to 2010) were available. The vertical distribution of the vegetation was analysed on-site by the measurement of stand characteristics such as tree height, tree type, and height of understory. The vertical vegetation structure is needed for calculating the aerodynamic resistances and must be assumed to be similar for the surrounding area. Furthermore, both burnt and control sites were selected to be at least 90 m away (at least three pixels, with a pixel size of 30 m) from the burnt area boundaries. Control and burnt sites were also visually (aerial photography) compared to each other to eliminate structural influences (small roads, or buildings, which cannot be seen at satellite imagery) and to find similar forest stand structure. Then, the surface reflectance of the control and the burnt site was compared to each other, using satellite images acquired approximately one month before the fire event. For the fires of 2011 and 2012, Landsat 5 images (bands *b*, 1–5 and 7) were used, while for the 2013 fires, Landsat 8 images (*b*, 1–7) have been already available. If the average surface reflectance of each band of both sites was within one standard error (see, for example, Figure 2), they were defined as comparable and, therefore, constituting a pair (Sánchez et al. 2015).

2.3. Stand biometry

During 2007–2010, eucalyptus inventories were carried out by CELPA in privately owned properties. The year of the forest inventory closest to the fire year was selected, and the data used to project the stand growth with the Web-Globulus 3.0 empirical model (Tomé, Oliveira, and Soares 2006). To obtain the mean tree height of an eucalyptus stand, different variables must be known. Stand density, stand age, and dominant height served as model input to predict the quadratic mean diameter at breast height (dbh),

Table 1. Description of fire scars.

Year	Area burnt (ha)	Description	Fire scar sizes (ha)	Time of wildfire
2011	118	Many small sized ones	6–51	August/September, with one exception in April
2012	1113	Several with different sizes	24–929	Beginning till end of September
2013	7343	Two fire scars	815; 6528	July and August, respectively

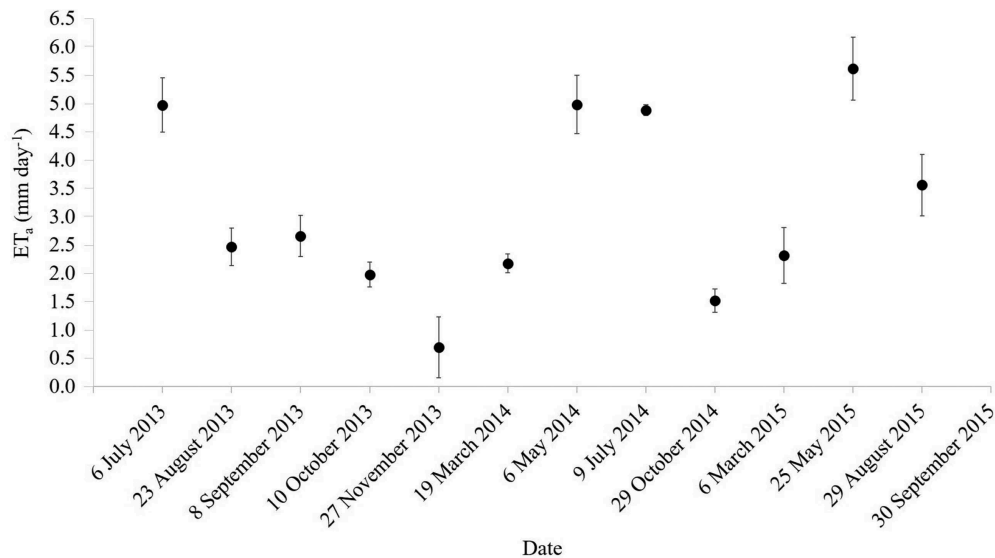


Figure 2. The dots indicate the average of the estimated ET_a of the control sites for each observation day. The standard deviation is indicated and used to define the natural variability between different test stands (about 0.5 mm day^{-1}).

from which the mean tree height can be estimated. This was done for the years 2013–2015 with the Web-Globulus 3.0 version available at Palma (2013).

The understory characteristics were obtained from the 5th National Forest Inventory (AFN 2010) of Continental Portugal and the CELPA inventory plots with the main herbaceous species of *Rubus* spp., *Ulex* spp., and *Erica* spp. The average understory height was estimated to be around 1.0 m (Boulet et al. 2015). After a fire, the shrub height was estimated to be 0.4 m, 0.7 m, and 1.0 m for the first, the second, and the third plus following years, respectively.

2.4. Remote-sensing and meteorological data

From May 2013 till September 2015, 16 Landsat 8 images distributed by the US Geological Survey (Collection 1, Level-2) were processed (approximately five per year). Cloudless images for Path 204 and Row 32 were selected, with an overpass time around 11:15 UTC scene centre time. Aboard, the Operational Land Imager sensor (visible and near-infrared bands), and the Thermal Infrared Sensor have a medium spatial resolution of 30 m and 100 m, respectively, offering a detailed observation of the Earth's surface. The Level-1 of the surface 8 reflectance code (LASRC) product, b_{2-7} , and the brightness temperature, b_{10} (LT08 for Collection 1), were downloaded and further processed.

In total, five meteorological stations in the study area were selected for providing on-site measurements of the air temperature (T_a , K), the wind speed (u , m s^{-1}), and the global solar radiation (S , W m^{-2}) (Table 2 and Figure 1). These variables were interpolated and maps were created using the ordinary kriging technique (Section 3.1.1). At the Aveiro/Suburban area station, being the sixth station listed at Table 2, measurements of T_a and u served for validation and were therefore not included in the interpolation procedure. Since April 2014, the system is operating, which consists

Table 2. Location of the meteorological stations are given. Point measurements of T_a , u , and S were taken and used for interpolating the data (ordinary kriging) over the study area. Measurements at Aveiro/Suburban area were not included in the kriging technique, but used for validation.

Meteorological station	Latitude (°)	Longitude (°)	Elevation (m)
Pousadas	40.6144	-8.3166	432
Viseu/C. C.	40.7149	-7.8959	636
Aveiro/Universidade	40.6354	-8.6596	5
Anadia	40.4388	-8.4399	45
Arouca	40.9269	-8.2611	270
Aveiro/Suburban area	40.6142	-8.6516	19

Table 3. Range of ΔNBR to classify different severity burn levels, which was adapted from Key and Benson (1999).

Severity classification	Range of ΔNBR
Unburned	<0.099
Low	0.100–0.255
Moderate–low	0.256–0.410
Moderate–high	0.411–0.660
High	>0.660

Table 4. Soil and canopy reflectance and NDVI values for the different dates are listed. Mean values for the different regions of interest (ROI) from L8 scenes are given.

L8 acquisition date	$b_{5,v}$	$b_{5,s}$	$b_{4,v}$	$b_{4,s}$	NDVI_v	NDVI_s
20 June 2013	0.339	0.278	0.053	0.167	0.750	0.262
6 July 2013	0.342	0.258	0.028	0.178	0.841	0.193
23 August 2013	0.396	0.156	0.029	0.087	0.862	0.230
8 September 2013	0.369	0.202	0.027	0.121	0.863	0.253
10 October 2013	0.303	0.185	0.025	0.072	0.844	0.232
27 November 2013	0.277	0.130	0.023	0.086	0.849	0.205
19 March 2014	0.387	0.126	0.041	0.084	0.804	0.202
6 May 2014	0.409	0.193	0.037	0.122	0.832	0.227
9 July 2014	0.398	0.227	0.027	0.146	0.872	0.221
29 October 2014	0.180	0.254	0.030	0.170	0.714	0.216
6 March 2015	0.202	0.213	0.024	0.140	0.784	0.217
25 May 2015	0.374	0.201	0.033	0.120	0.831	0.260
28 July 2015	0.381	0.204	0.026	0.127	0.865	0.238
29 August 2015	0.329	0.150	0.029	0.106	0.834	0.186
30 September 2015	0.177	0.128	0.022	0.084	0.830	0.198

of a 12-m tall tower, located at the suburban area of Aveiro, Portugal (40°36'51.07"N, 8°39'05.90"W, Datum WGS84). A three-dimensional sonic anemometer (Windmaster Pro, Gill Instruments, Lymington, UK) was installed, directly measuring the three components of wind speed and virtual temperature. The instrument allowed to calculate T_a and u . The 10-Hz raw flux data were stored, using the data logger Xlite 9210 (Sutron Corporation, Sterling, VA, USA). The measurements were integrated and recorded at 30-min intervals.

The incident longwave radiation L_{sky} was provided every 30 min by the Spinning Enhanced Visible and Infrared Imager (Seviri) aboard Meteosat. The data were downloaded from the EUMETSAT Satellite Application Facility on Land Surface Analysis (LSA SAF), with a spatial resolution of $3 \times 3 \text{ km}^2$. Due to uniformity of L_{sky} over large areas under cloud-free sky conditions (Humes et al. 2004), the pixel values for L_{sky} , covering the corresponding test sites, were further processed.

Table 5. Atmospheric parameters (transmissivity, up- and down-welling sky irradiance) estimated from 4.0 MODTRAN code, as well as incident-longwave radiation L_{sky} and solar global radiation S at the time of satellite overpass. (The value for S is the one measured at the Pousadas station.)

L8 acquisition	τ	L_{atm}^{\uparrow}	L_{atm}^{\downarrow}	L_{sky}	S
date		(W m ⁻² sr ⁻¹ μm ⁻¹)	(W m ⁻² sr ⁻¹ μm ⁻¹)	(W m ⁻²)	(kJ m ⁻²)
20 June 2013	0.83	1.24	2.06	333	850
6 July 2013	0.69	2.59	4.18	415	899
23 August 2013	0.80	1.61	2.65	359	818
8 September 2013	0.89	0.88	1.49	317	834
10 October 2013	0.88	0.96	1.62	322	683
27 November 2013	0.95	0.35	0.60	242	473
19 March 2014	0.83	1.22	2.04	303	714
6 May 2014	0.81	1.38	2.28	340	934
9 July 2014	0.82	1.48	2.44	333	957
29 October 2014	0.78	1.67	2.76	345	534
6 March 2015	0.95	0.35	0.61	259	718
25 May 2015	0.84	1.20	2.00	331	942
28 July 2015	0.72	2.41	3.76	372	927
29 August 2015	0.81	1.66	2.70	373	848
30 September 2015	0.81	1.48	2.43	331	711

Table 6. Ratio of $R_{n,d}/R_{n,i}$ used to estimate daily values of the energy balance fluxes obtained by the STSEB model.

Month	Year 2013		Year 2014		Year 2015	
	Day	Ratio	Day	Ratio	Day	Ratio
March	–	–	19	0.237	6	0.194
May	–	–	6	0.280	25	0.282
June	20	0.295	–	–	–	–
July	6	0.284	9	0.284	28	0.290
August	23	0.267	–	–	29	0.267
September	8	0.240	–	–	30	0.220
October	10	0.201	29	0.170	–	–
November	27	0.130	–	–	–	–

To obtain land surface temperature T_{rad} from brightness temperature, satellite data had to be atmospherically corrected. Thus, hemispheric down-welling sky radiance L_{atm}^{\downarrow} , hemispheric up-welling sky radiance L_{atm}^{\uparrow} , and atmospheric transmissivity τ were obtained through the Atmospheric Correction Parameter Calculator by Barsi, Barker, and Schott (2003), using MODTRAN 4.0 code (Berk 1999).

3. Methodology

3.1. Preliminary work

3.1.1. Kriging

The ordinary kriging technique was applied, which uses a semivariogram model to interpolate meteorological data such as T_a , u , and S (Liu, Shi, and Erdem 2010; Rehman and Ghori 2000; Hengl et al. 2012). Maps of the area of interest were created and used for the model.

3.1.2. Fire severity classification

The severity of the fire, which describes the extent of the damage to the vegetation, was derived from the Normalized Burn Ratio (NBR). This index is related to vegetation vitality

and water content in vegetation and soil (Veraverbeke et al. 2010), combining near-infrared (b_5) and shortwave infrared (b_7) reflectance, as given in Equation (1):

$$\text{NBR} = \frac{b_5 - b_7}{b_5 + b_7}. \quad (1)$$

The change in surface vegetation and ground properties by the fire is characterized by a drop in the reflectance in the (b_5) and the (b_7) (García and Caselles 1991; see also Figure 3(b)). Pre- and post-fire images were compared using the NBR where changes are qualitatively ranked into low- to high-severity burns. The difference between pre- and post-fire images is called ΔNBR (Equation (2)), and its intervals for the different severity classes used for this study are given by Key and Benson (1999). see also Table 3.

$$\Delta\text{NBR} = \text{NBR}_{\text{pre-fire}} - \text{NBR}_{\text{post-fire}}. \quad (2)$$

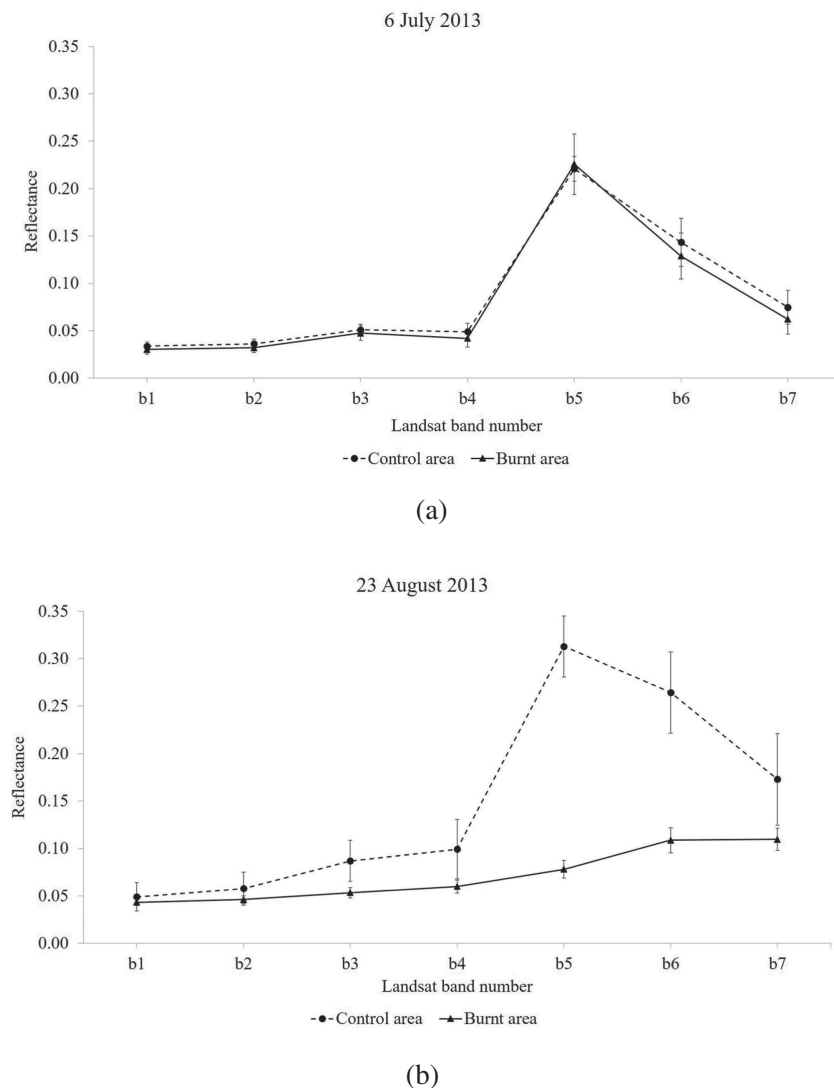


Figure 3. One example of a 2013 fire comparing control and burnt area before (Landsat 8 image taken on 6 July 2013) and after the fire (Landsat 8 image taken on 23 August 2013).

3.2. STSEB model

3.2.1. Latent heat flux retrieval

The STSEB model estimates the energy balance fluxes of R_n (W m^{-2}), H (W m^{-2}), and G (W m^{-2}) from remote-sensing data and meteorological variables. The instantaneous values of LE (W m^{-2}) are retrieved by solving the energy balance equation ($R_n = H + LE + G$) for LE . Total R_n and H are retrieved by summing up the contributions of canopy (subindex v) and soil (subindex s), which are individually estimated.

The total R_n is the sum of $R_{n,v}$ and $R_{n,s}$, weighted by its corresponding vegetated and bare soil contributions (Sánchez et al. 2008), expressed as:

$$R_n = P_v R_{n,v} + (1 - P_v) R_{n,s}, \quad (3)$$

where P_v stands for partial vegetation cover and was obtained by a simple equation (Equation (4)) introduced by Valor and Caselles (1996) using the Normalized Differenced Vegetation Index (NDVI, Equation (5)) to estimate the proportions of bare soil and total vegetation cover of each mixed pixel. Again, the NDVI is used to select vegetated and bare soil pixels within the satellite images. After selecting pure soil and vegetated locations (region of interest), the mean NDVI of each proportion was taken, indicated as $NDVI_v$ and $NDVI_s$, respectively (Table 4). The ranges for the NDVI comprising vegetated and bare soil pixels were used as described in Sobrino, Jiménez-Muñoz, and Paolini (2004). P_v and NDVI were obtained as follows:

$$P_v = \frac{\left(1 - \frac{NDVI}{NDVI_s}\right)}{\left(1 - \frac{NDVI}{NDVI_s}\right) - K \times \left(1 - \frac{NDVI}{NDVI_v}\right)}. \quad (4)$$

$$NDVI = \frac{b_5 - b_4}{b_5 + b_4}, \quad (5)$$

where b stands for the corresponding band of Landsat 8 (Table 4), and the coefficient K is given by

$$K = \frac{b_{5,s} - b_{4,v}}{b_{5,s} - b_{4,s}}. \quad (6)$$

Consequently, the contributions of canopy and soil to the total R_n are calculated by establishing a balance between the short- and longwave radiation for each component, separately:

$$R_{n,v} = (1 - \alpha_v)S + \varepsilon_v L_{sky} - \varepsilon_v \sigma T_v^4. \quad (7)$$

$$R_{n,s} = (1 - \alpha_s)S + \varepsilon_s L_{sky} - \varepsilon_s \sigma T_s^4, \quad (8)$$

where the albedo for canopy α_v and soil α_s were assumed to be 0.14, and 0.18, respectively. These values are given in Wilson and Henderson-Sellers (1985) for ever-green broadleaf trees, and typical soil albedo classified according to their colour and moisture content. The emissivity components for canopy ε_v and soil ε_s were assumed to be values of $\varepsilon_v = 0.982$ and $\varepsilon_s = 0.950$ on the basis of vegetation characterizations and their respective emissivities by Rubio, Caselles, and Badenas (1997) and Valor and

Caselles (1996). The Stefan–Boltzmann constant is σ (5.67×10^{-8} , $\text{W m}^{-2} \text{K}^{-4}$) and the soil temperature is T_s given in kelvin (K).

Following this concept, the total H is once again obtained by dividing the surroundings into canopy and soil contributions:

$$H = P_v H_v + (1 - P_v) H_s, \quad (9)$$

where H_v and H_s , for the time of satellite overpass (instantaneous values), are expressed as

$$H_v = \rho C_p \frac{T_v - T_a}{r_a^h}. \quad (10)$$

$$H_s = \rho C_p \frac{T_s - T_a}{r_a^a + r_a^s}. \quad (11)$$

Here, ρ stands for air density (kg m^{-3}) and C_p ($\text{kJ kg}^{-1} \text{K}^{-1}$) denotes the air-specific heat at constant pressure. T_v and T_s are the temperatures of the vegetation and the soil, respectively, both also given in kelvin (K). The estimations of the aerodynamic resistances r_a (m s^{-1}) for stable and unstable conditions are based on Sánchez et al. (2008).

To obtain T_{rad} from a single thermal band, different approaches are available, such as the mono-channel (Wang et al. 2015) or the single-channel algorithm (Jimenez-Munoz et al. 2014) based on the radiative transfer equation. Here, the following equation was used:

$$L_{\text{sen}} = \left[\varepsilon B(T_{\text{rad}}) + (1 - \varepsilon) L_{\text{atm}}^{\downarrow} \right] \tau + L_{\text{atm}}^{\uparrow}, \quad (12)$$

where L_{sen} is the top of atmospheric radiance, i.e. the radiance measured by the sensor, ε is the land surface emissivity, and $B(T_{\text{rad}})$ (K) is the radiance of a black body given by Planck's Law. The variables τ , $L_{\text{atm}}^{\downarrow}$ ($\text{W m}^{-2} \text{sr}^{-1} \mu\text{m}^{-1}$), and $L_{\text{atm}}^{\uparrow}$ ($\text{W m}^{-2} \text{sr}^{-1} \mu\text{m}^{-1}$) were obtained by introducing radio-sounding data into MODTRAN 4 code (Table 5) as explained in Section 2.4.

The surface emissivity was estimated by the equation proposed by Valor and Caselles (2005), using P_v , and its emissivity components ε_v and ε_s :

$$\varepsilon = \varepsilon_v P_v + \varepsilon_s (1 - P_v) (1 - 1.74 P_v) + 1.7372 P_v (1 - P_v). \quad (13)$$

By inverting Equation (12), and correcting the radiance for atmospheric and emissivity effects, the radiometric surface temperature T_{rad} (K) was obtained.

In order to run the model, the temperatures for T_v and T_s have to be estimated, for which following relationship was used:

$$T_{\text{rad}} = \left[\frac{P_v(\theta) \varepsilon_v T_v^4 + (1 - P_v(\theta)) \varepsilon_s T_s^4}{\varepsilon} \right]^{\frac{1}{4}}. \quad (14)$$

Separating T_v and T_s from T_{rad} without having ground measurements for comparison is difficult, but crucial to obtain good estimates for ET_a .

By plotting P_v against T_{rad} , isolines with an almost linear relationship can be retrieved (Equation (14)), indicating lower temperatures for fully covered pixels and higher temperatures for bare soil pixels (Carlson 2007; Yang et al. 2015; Kasim and Usman 2016).

Here, a linear relationship ($y = mx + t$) between T_{rad} and P_v was assumed to extract the radiometric temperature components from Equation (15).

$$\underbrace{\varepsilon T_{\text{rad}}^4}_y = \underbrace{P_v}_x \underbrace{(\varepsilon_v T_v^4 - \varepsilon_s T_s^4)}_m + \underbrace{\varepsilon T_s^4}_t. \quad (15)$$

In the following, the values for T_{rad} and P_v were extracted over the areas of interest (control and burnt sites separately) with squares of increasing sizes (3×3 up to 15×15). Then, the variables were plotted against each other to get the temperatures for canopy and soil by assuming a linear relationship between them as given in Equation (15). At least 9×9 pixels were necessary to include mixed pixels with higher and lower vegetation cover to get good estimates for T_s and T_v . Larger areas (11×11 or 15×15 pixels) gave similar results with no significant changes in temperatures. For this study, we decided to extract 11×11 pixels to determine T_s and T_v , as in very few cases the extraction of 9×9 pixels still differed compared to larger areas. This procedure was done for each control and burnt site separately.

In order to run the model, first estimates of H and LE are required. In the literature, different approaches such as the Priestley–Taylor equation and others (Sánchez et al. 2008; Venturini et al. 2008; Liou and Kar 2014) are proposed to obtain first estimates. As a first approximation, stable conditions for the aerodynamic resistance were assumed (where the transport of heat and momentum are equally efficient) to approximate H and LE . Then, they were further estimated to unstable conditions, using an iterative process to calculate the aerodynamic resistances from stable to unstable conditions (see Appendix of Sánchez et al. 2008).

The soil heat flux density G is retrieved as a fraction of R_n with:

$$G = C_G(1 - P_v)R_n. \quad (16)$$

This ratio differs with vegetation cover and the time of the day (Clothier et al. 1986; Allen et al. 1998; Kustas and Daughtry 1990), being higher for dry soils and lower under wet conditions (Idso, Aase, and Jackson 1975). For our study, C_G was set to 0.4 for the dry months of the year (July, August, and September), when the understory vegetation is senescent (Häusler et al. 2016) and the soil moisture decreased (Idso, Aase, and Jackson 1975). C_G was set to 0.15 for the other months of the year, when soil moisture was increased and the understory was green. A ratio of about 0.1 for full cover was suggested by Kustas and Daughtry (1990), and for agricultural purposes by De Bruin and Holtslag (1982) for a short grass pasture.

Finally, LE during satellite overpass was retrieved by subtracting H and G from R_n . Waterbodies and urban areas were masked within all images to avoid any influence or to be misleadingly considered as uncovered (e.g. bare soil) surfaces.

To obtain daily values from the instantaneous ones, the following relationship was considered (Seguin and Itier 1983):

$$\frac{H_i}{R_{n,i}} = \frac{H_d}{R_{n,d}}. \quad (17)$$

This relationship is representative for cloudless days. To obtain daily values, the instantaneous values taken around midday (here, Landsat 8 overpass time around 11:15 a.m.)

were used. Thus, assuming that G can be neglected on a daily scale (Seguin and Itier 1983; Kustas and Daughtry 1990), the energy balance equation is written as:

$$R_{n,d} = H_d + LE_d, \quad (18)$$

and LE_d finally obtained as a residual term combining Equations (17) and (18), retrieving:

$$LE_d = \frac{R_{n,d}}{R_{n,i}} (R_{n,i} - H_i). \quad (19)$$

The ratio of $R_{n,d}/R_{n,i}$ is dependent on latitude, day of the year, and the time of day, but independent of the type of vegetation (Table 6) (Wassenaar et al. 2002; Sobrino et al. 2005; Sánchez et al. 2007; Cristóbal et al. 2011; Sánchez et al. 2015).

3.3. Changes of daily ET_a

The estimated LE_d ($W m^{-2}$) was converted into ET_a ($mm day^{-1}$). To assess the recovery of ET_a after a wildfire, the total difference of ET_a (ΔET_a , subtraction of the estimated ET_a at the burnt site from the control area) was investigated (see Figure 4).

$$\Delta ET_a = ET_{a, \text{control site}} - ET_{a, \text{burnt site}}. \quad (20)$$

To define the recovery of the stand to the original state before the fire, a threshold was established. The estimated ET_a of all control sites used for this study was averaged and the standard deviation calculated. The standard deviation was $<0.5 mm day^{-1}$ (Figure 2) for almost all observation days. Thus, this benchmark of $\pm 0.5 mm day^{-1}$ was defined as the indicator of natural variability between test stands.

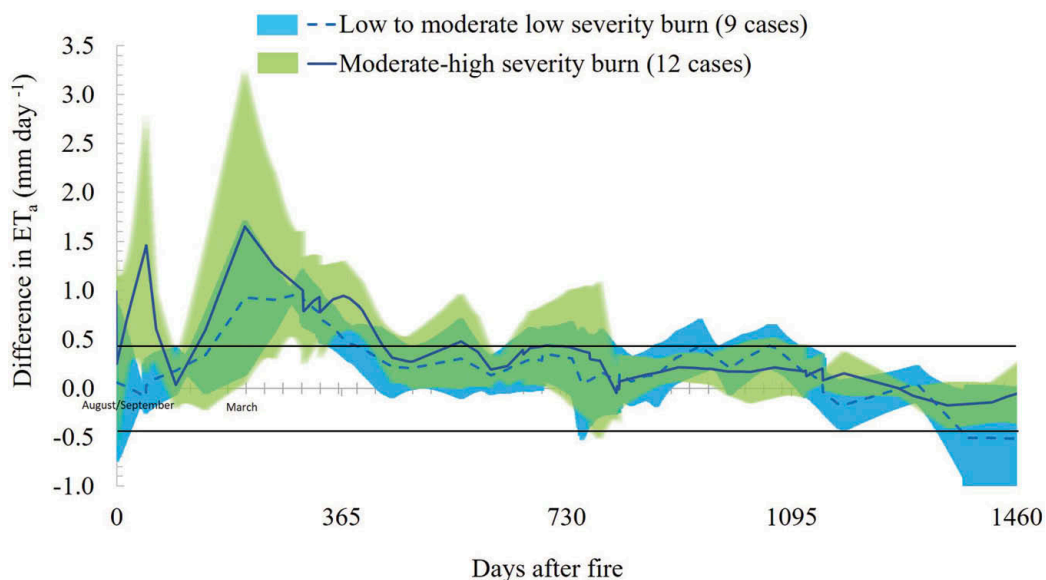


Figure 4. The graph shows the evolution of ΔET_a (difference in ET_a between control and burnt site in $mm day^{-1}$) over the period of time after the fire event. Moderate-high- and moderate-low-severity burns are plotted separately showing the average of 12 and 9 affected plots with the standard deviation indicated in green and blue, respectively. The classification into fire severity levels is given in Key and Benson (1999).

4. Results

4.1. Fire severity classification

A total of 21 sites that mostly burnt during the dry months of August and September were evaluated. The direct impact, which was caused by the fires on vegetation and soil, was classified by their severity using the ΔNBR . Nine of the burnt areas were graded as low- to moderate-low-severity burns, while 12 of them were categorized as moderate-high-severity burns. The paired burnt-unburnt sites revealed minor differences in [Figure 3\(a\)](#) before the fire as opposed to [Figure 3\(b\)](#) after the fire.

4.2. Kriging technique

The interpolated maps of u and T_a created by ordinary kriging technique were compared to measurements taken at the Aveiro/Suburban area station. The relationships were very strong, with the coefficient of determination R^2 of 0.92 in the case of u and 0.83 in the case of T_a ([Figure 5](#)). The root mean square error was 0.2 m s^{-1} and 1.0°C and the mean absolute error was 0.2 m s^{-1} and 0.8°C for u and T_a , respectively.

4.3. Latent heat flux retrieval

The differences in total as well as canopy and soil LE between the neighbouring burnt and unburnt sites were determined for three dates (23 August 2013, 9 July 2014, and 29 August 2015) at the time of satellite overpass. These dates were chosen as the July-August period corresponds to the summer dry period in the study region, when the peak of fire occurrences tends to occur and when differences in the vegetation's phenological status between the exact dates are expectantly minor. [Figure 6](#) compares the relative contributions of LE_s and LE_v for the neighbouring pairs of control and burnt sites on the three referred dates.

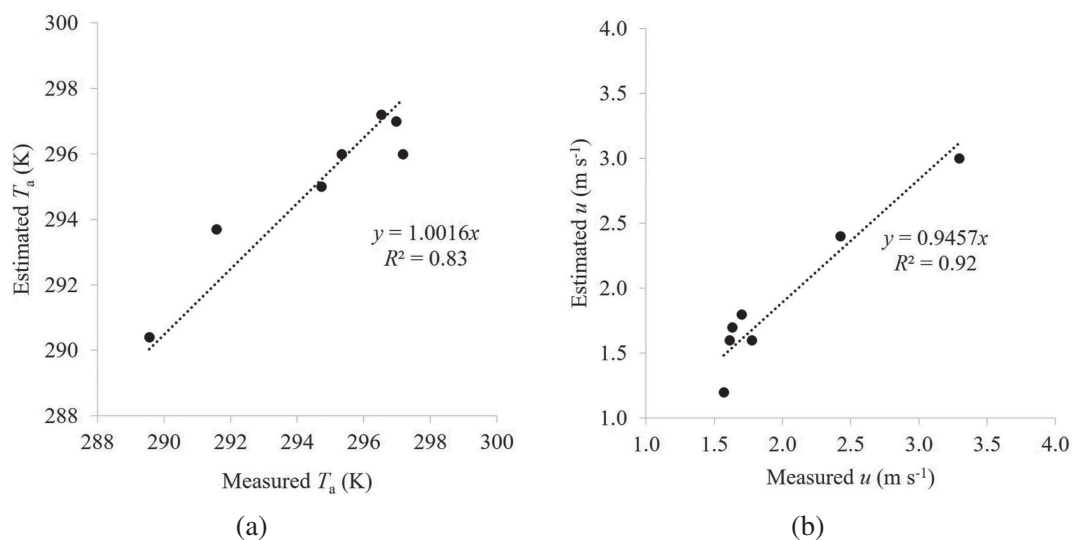


Figure 5. Figures (a) and (b) show the relationship between measured and estimated T_a and u , respectively, where variables were recorded at the Aveiro/Suburban area station, and the estimates modelled with the ordinary kriging technique.

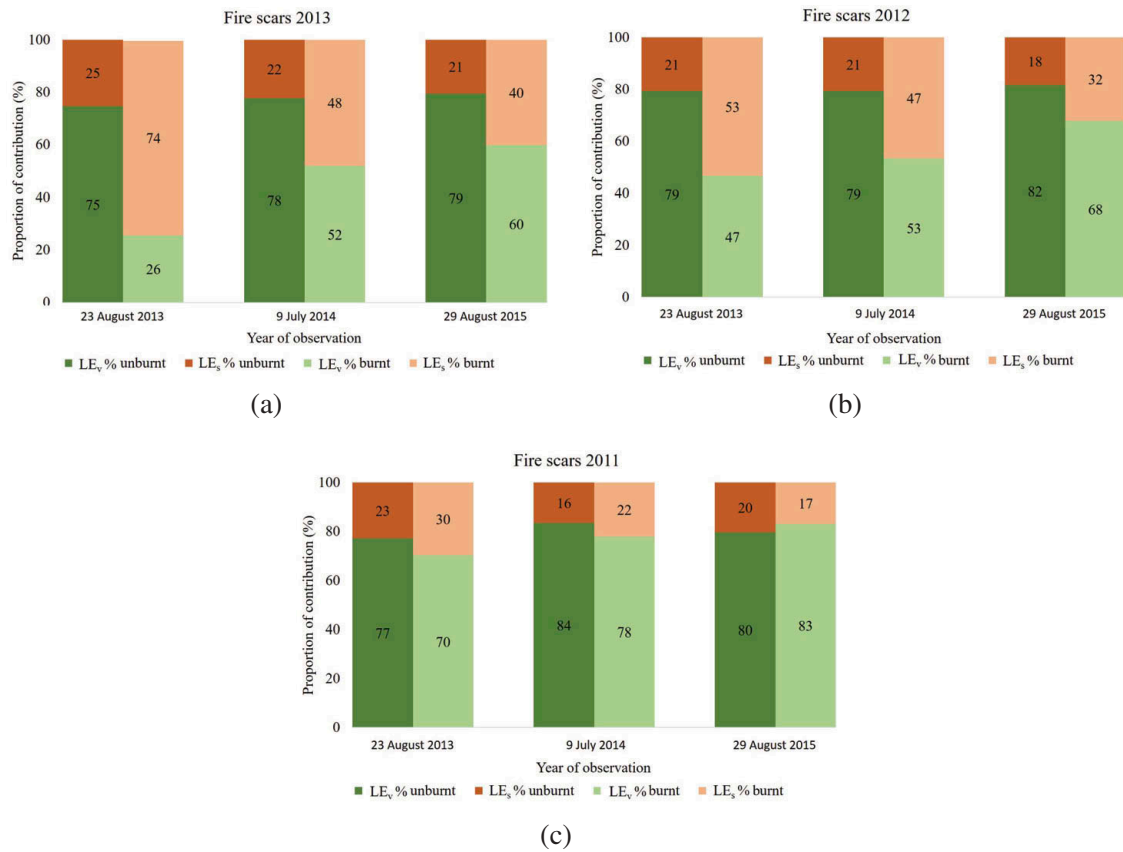


Figure 6. Figures (a), (b), and (c) show the contributions of soil (LE_s) and canopy latent heat flux (LE_v) to the total latent heat flux during satellite overpass (LE_i) in percentage for the years 2013, 2012, and 2011, respectively. For the specific observation day, the fire scars were averaged (right column) and plotted against the respective average of the associated control sites (left column). Note that the total LE_i from the burnt and unburnt sites differ from each other in magnitude (see Section 4.3).

For the 2013 wildfires, the soil contribution to the total LE in August 2013 (i.e. immediately after the fires) contrasted sharply between the burnt and unburnt sites, with on average 75% vs 25% (Figure 6(a)). This soil contribution at the unburnt sites varied little between years as well as between burnt areas. The absolute difference in total LE between the 2013-burnt and neighbouring control sites was similar immediately after the fire in August 2013 ($120 \pm 70 \text{ W m}^{-2}$) and roughly one year later in July 2014. In August 2015, however, this difference was less than half/roughly twice as small ($54 \pm 27 \text{ W m}^{-2}$). In 2013, there were four moderate–high and three moderate–low fire scars monitored. Their tree density was between 800 and 1800 trees-ha⁻¹, the tree age was between 8 and 14 years, and their estimated tree height was between 12.4 and 16.8 m.

For the 2012 fire events, on average LE_v and LE_s contributed to equal parts after one and two years of the fire occurrence for the days of observation (Figure 6(b)). There was a tendency of higher soil contribution in the first and higher canopy contribution in the second year for the observation days in summer. During the observation year 2015 (three years after the fire), the distribution changed to about 70% of the canopy and around 30% of the soil (Figure 6(b)). The total differences in LE between control and burnt site were around $90 \pm 44 \text{ W m}^{-2}$, $100 \pm 53 \text{ W m}^{-2}$, and almost $60 \pm 30 \text{ W m}^{-2}$ for the first, second, and third year of observation, respectively. In 2012, the moderate–

high-severity burns outweighed the moderate–low classified fire scars with six to two observations. The tree density was between 600–1100 trees-ha⁻¹, the tree age was between 7 and 8 years, and their estimated tree height was between 10 and 12.6 m.

For the fire events in 2011, the average proportion changed of around 70% LE_v and 30% LE_s to about 80% and 20% for LE_v and LE_s, respectively, from the second to the third year after the disturbance. The proportion of soil and canopy to the total LE suddenly changed for the date at the fourth year of observation in 2015, where the contribution of the canopy exceeded 83%, which was larger than the canopy contribution at the control area (80%). In contrast, the soil contributed with 17%, being also smaller than the LE_s at the control stand with around 20% (Figure 6(c)). The difference in LE, in absolute terms, was around $56 \pm 28 \text{ W m}^{-2}$ for the second year, $33 \pm 16 \text{ W m}^{-2}$ for the third year, and $-51 \pm 26 \text{ W m}^{-2}$ for the fourth year on average, indicating higher LE at the burnt site during satellite overpass. In 2011, four fire scars were classified as moderate–low to low- and two as moderate–high-severity burns. The tree density was between 600 and 1800 trees-ha⁻¹, the tree age was between 6 and 9 years, and their estimated tree height was between 11.5 and 14.4 m.

4.4. Changes of daily ET_a

In agreement with the first research hypothesis, the greatest ΔET_a between the control and the fire-affected site occurred during the first year of observations (i.e. 2013) for all classifications. The differences in ET_a between the unburnt and 2013-burnt sites, immediately after the fire in August 2013, seemed to relate to ΔNBR . In the case of the burnt sites at moderate–high severity, a sudden increase in ΔET_a appeared shortly after the fire and a second peak around March.

In March, ΔET_a was around 1.5 mm day⁻¹ on average. For the moderate–low cases, Δ increased in a constant manner with time since the fire and also reached its maximum around March, with an average of ΔET_a around 0.9 mm day⁻¹ after the first year of the fire.

In the second year, the average of all cases has been already beneath the threshold of 0.5 mm day⁻¹, marking the natural variability within the plots. This means that there was no significant difference in ET_a and that the sites were defined to be equivalent. Even though the average might have been returned to the division of natural variation, this does not mean a recovery to the former status of the forest. This is indicated by the standard deviation showing a large distribution in ΔET_a , where moderate–high-severity cases were in the range of 0.0 to almost 1.0 mm day⁻¹, and moderate–low cases within an interval of -0.2 to 0.7 mm day⁻¹ around March. By the end of the second year (August/September), moderate–low to moderate–high cases ranged between -0.5 mm day⁻¹ (both) and 0.7 and 1.1 mm day⁻¹, respectively.

After the third year, the moderate–high classified areas did not show any extreme peaks, but rather started to decline with an average becoming slightly negative ΔET_a (around -0.1 mm day⁻¹) by the end of the fourth year. For the moderate–low cases, the average of ΔET_a reached the -0.5 mm day⁻¹ threshold in the last quarter of the fourth year, suggesting a further decrease in ΔET_a , which means higher evapotranspiration at the burnt site compared to the control after the fire. At this point, the standard deviation marks a range of around 0.0 to -0.8 mm day⁻¹ for ΔET_a .

5. Discussion

5.1. Latent heat flux retrieval

In this study, one year after the 2013 fire, and two to three years after the 2012 fire, the LE_v and LE_s contributed to the total LE on average to almost equal parts during satellite overpass. This result is comparable to the ones obtained by Nolan et al. (2014), even though methods, site description, and classification of fire severity differ from our approach. They conducted a study in the Maroondah and Coranderrk catchments with a vegetation mix of wet ash-type and mixed eucalyptus stands. At the moderately burnt areas, transpiration contributed between 42% and 59% after one to two years after the fire, on average (interception 28–43%, forest floor evapotranspiration 13–15%, Nolan et al. 2014). In our study, the portions of LE_v and LE_s were about 80% and 20%, respectively, of the overall LE. In unburnt stands, Nolan et al. (2014) reported a contribution of LE_v between 64% and 71% which is less than the ones estimated here.

Our results show higher LE_v compared to the control sites after the fourth year of the 2011 fires (mostly moderate–low-severity burns). Higher LE_v (compared to control area) were also recorded by Nolan et al. (2014) for moderate-severity burns already around January of the third year after the fire (records given in mm month^{-1}). The increase of LE_v was observed for trees and shrubs (>1.2 m), as well as for forest floor ET_a (including vegetation smaller 1.2 m, but no shrubs). LE_v of trees and shrubs higher than 1.2 m accounted for the largest contribution to the total ET_a , where 21–42% was coming only from shrubs.

Most species of the Mediterranean climate are adapted to fires and regenerate by resprouting or seed germination (Tessler, Wittenberg, and Greenbaum 2016). After only a few weeks, shrubs start to regrow (Silva, Rego, and Mazzoleni 2002; Bastos et al. 2011), followed by the trees' regeneration. The eucalyptus tree is not only well adapted to fire, but adaptations such as lignotubers, extensive root systems, epicormic buds, and hard woody capsules ensure their survival and fast recovery (Catry et al. 2013; Nolan et al. 2015; Arán et al. 2013).

In central Portugal, Catry et al. (2013) assessed the post-fire survival in eucalyptus stands, where after one year tree mortality was rather low (3.9%). For most *Eucalyptus globulus* trees, the most common post-fire regeneration type was basal resprouting (lignotuber, 89.2%) followed by epicormic shooting (20.9%) among all sampled trees.

Comparing our results with other, mainly Australian studies (Watson et al. 1999; Nolan et al. 2014; Nolan et al. 2015), the recovery in terms of ET_a seems to be slower. One reason for a slower regrowth might be the very low soil depth in central Portugal, having low water storage capacity and an almost impenetrable bedrock, making deep rooting impossible and giving the trees only a limited access to soil and groundwater (Santos et al. 2016). Nevertheless, it should be mentioned that the exceeding of ET_a compared to unburnt stands after only few years is not the regular case. Other tree species such as, e.g. pines need many years to make a recovery. Six to seven years after the fire, Sánchez et al. (2015) were still able to record differences between control and burnt site of around $140 \pm 30 \text{ W m}^{-2}$ for total LE during satellite overpass.

5.2. Changes of daily ET_a

As explained in Section 3.1.2, the measure of ΔNBR identified the severity of fire events in the eucalyptus stands in 2013–2015, which were ranked according to the

intervals given by Key and Benson (1999). This index has already been successfully applied to different species and environments (Escuin, Navarro, and Fernández 2008; Miller and Safford 2012; Veraverbeke et al. 2010) and classified the burnt sites into moderate–low- to low- and moderate–high-severity burns, implying rather small damages to the stands and a high survival rate of the trees. Mortality of eucalyptus stands is not only dependent on the severity of the fire, but also on other factors or properties of the stand. Here, the trees were 6–14 years old and in their second or third rotation. According to Silva, Feith, and Pereira (2007), mortality decreases with age and increases with the number of rotations, which implies a rather shortened recovery time for our study sites.

As expected, after a fire event, the ΔET_a of all cases increased rapidly, due to the removal of the understory to a large degree and a partial or total damage to the tree crown. Figure 7 shows a clear difference in NDVI, P_v , and T_{rad} , comparing the fire scars to the surrounding area. The NDVI is a measure of ‘greenness,’ while P_v expresses the fractions of vegetated and bare soil surface. After a fire disturbance, both decrease drastically, due to the removal of green parts of the vegetation. At the same time, T_{rad} increases due to the darker surface of charred residuals. It should also be noted that there are other processes involved beyond changes to vegetation cover; an increase in the persistence of soil water repellency after the fire would also limit soil water storage and therefore decrease ET_a at the burnt site (Nunes et al. 2016).

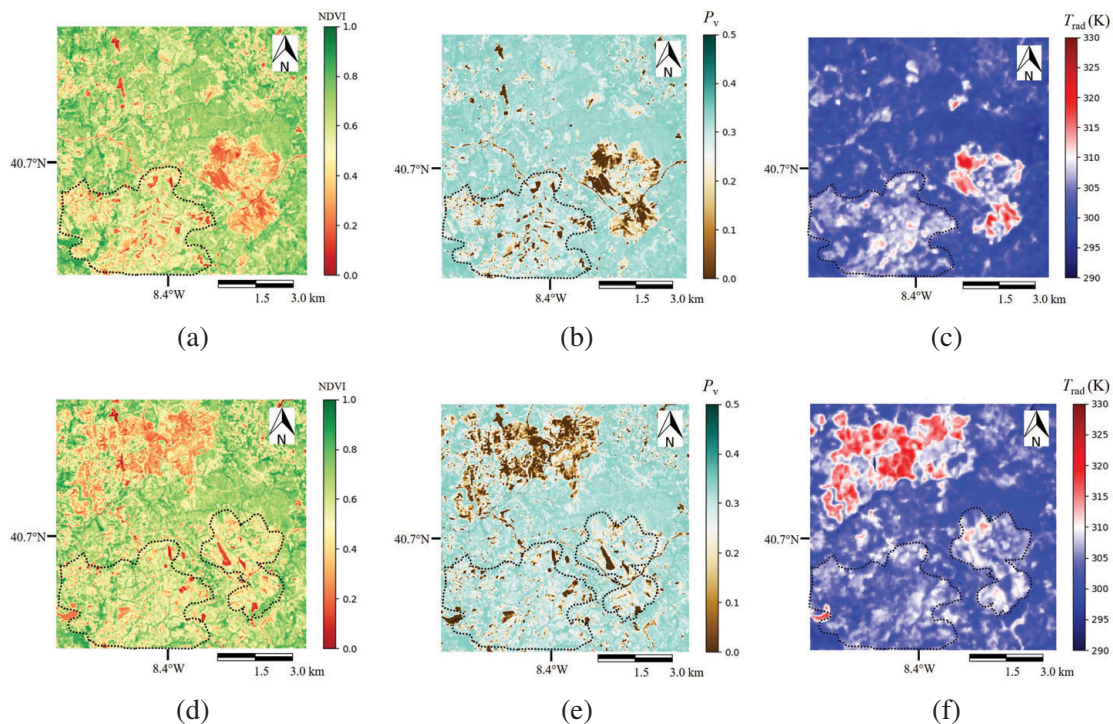


Figure 7. Figures (a), (b), and (c) show the variables NDVI, P_v , and T_{rad} (K), respectively, calculated from Landsat 8 images, which were taken on the 23 August 2013. In the lower left corner of all sub-figures, a fire scar from August 2012 is marked with a dashed line, while at the opposite a fire scar of July 2013 is visible. Figures (d), (e), and (f) show the same variables for the 25 May 2015. The fire events of 2012 (lower left) and 2013 (lower right) are surrounded with dashed lines. For comparison, a fire scar of March 2015 is visible at the upper left corner, but was not used for this study.

Nevertheless, ΔET_a between control and burnt site started to decline rapidly. This might be partly explained by the shrublands which have higher rain interception in Mediterranean climate compared to other climates (Garcia-Estringana, Alonso-Blázquez, and Alegre 2010). They also start regrowing only shortly after environmental disturbances, e.g. fire (Silva, Rego, and Mazzoleni 2002; Bastos et al. 2011). Both, interception and regrowth, may contribute to a large part to the overall ET_a (see also Section 5.1). Moreover, the eucalyptus species has special adaptations that enhance their regrowth by basal regeneration (lignotuber) (Catry et al. 2013) and/or strong epicormic shooting triggered under certain circumstances, such as sudden increase of light availability due to the damage of the tree crown or the removal of close-by standing plants (Lane et al. 2010). This fast recovery was also observed in other studies, mentioning other survival strategies and regeneration of the forest from resprouting and seeds (Tessler, Wittenberg, and Greenbaum 2016; Nolan et al. 2014; Arán et al. 2013), where especially at the beginning a strong competition is observed and only with time, when the vegetation becomes larger and crowns start to close, the forest becomes subject to a natural thinning process (Tessler, Wittenberg, and Greenbaum 2016).

The study by Nolan et al. (2015) showed a peak in total ET_a at resprouting eucalyptus forests 2–3 years after the fire, which was up to 29% above unburnt stands. The authors claim that the increase in ET_a at the burnt site might be related to the combined effect of epicormic regrowth, and an only partial defoliation of the trees, causing a higher demand of water by a temporary higher leaf area index compared to adjacent unburnt tree stands. The severity of the fires was classified as moderate, and pre-disturbance conditions were reached after 5–8 years post-fire, being 8–12 years for high-severity burns in south-eastern Australia.

In our study, higher ET_a was only recorded in the case of the 2011 fires, four years after the fire event. The 2011 fires were mostly classified as moderate–low- to low-severity burns, where the burnt sites exceeded ET_a of the control sites by roughly 2% on a daily scale. However, Watson et al. (1999) reported total ET_a being twice as high compared to unburnt stands 7–30 years after the fire in mountain ash forests (*E. regnans*).

In contrast, post-fire ET_a might remain low for other tree species as shown in the case of pine trees in south-eastern Spain with Mediterranean climate, where ΔET_a at the burnt site was still 1.0 mm day^{-1} 11 years after the fire disturbance (Sanchez et al 2015, tree densities of $450 \text{ trees-ha}^{-1}$).

Both, the shortage of water released to the atmosphere and a higher water demand after a fire, are disturbances to the water cycle. Our results showed no significant changes in daily ET_a after the second year of the fire event, regardless of the burn severity. This is also supported by the findings of Hawtree et al. (2015), showing no significant changes in the streamflow at the Águeda watershed which comprises a large part of our study area.

6. Conclusions

The relationship between evapotranspiration and tree regrowth/recovery after fire disturbances in pure eucalyptus stands was observed by applying an STSEB model based

on satellite observations. The study was conducted in the Caramulo mountain range, located in the centre of Portugal. A total of 21 burnt sites of pure eucalyptus stands were investigated by comparing ET_a to nearby control sites that had similar stand properties. The results show:

- (i) to the total LE at the unburnt stands (control sites); LE_v (about 80%) and LE_s (about 20%) had similar contributions for all years of observation at the satellite overpass;
- (ii) the recovery to pre-fire conditions is rather different from other studies, namely ΔET_a has already been much smaller in the third year after the fire event in comparison;
- (iii) higher ET_a at the fire-affected areas compared to control sites is only recorded at mainly moderate-low- to low classified severity burns after four years of the fire event (with increasing tendency);
- (iv) generally, areas with lower severity classification had smaller differences in ΔET_a . The largest ΔET_a was observed during the first year, continuously decreasing over the observed four years after the fire; and
- (v) Inter-annually, ΔET_a increased during the rainy season, which is related to the fast regrowth rate of foliage and epicormic shooting, and the abundance of water.

Even though ΔET_a moved back to the threshold we defined as natural variability between stands ($\pm 0.5 \text{ mm day}^{-1}$), a full recovery to the former condition was not reached after four years of observations. A few of the burnt sites even responded with higher ET_a in comparison to the control sites probably related to the combined effect of basal and epicormic shooting, the recovery of the tree crown, and the germination of seeds.

To conclude, the effect of fire events on ΔET_a in eucalyptus stands was rather small in the north-central part of Portugal. Nevertheless, longer time series (>8 years) would be necessary to ensure the settlement of ΔET_a and give solid statements about the time of recovery in ET_a , the impact on the water budget, and consequently leading to adaptations in the fire management of Portugal.

Acknowledgements

The surface reflectance and brightness temperature data were provided by the US Geological Survey Earth Resources Observation and Science (EROS) Data Centre. The authors are grateful to all the scientists, engineers, and students who contributed to this project, especially to Dr Christian Melsheimer and Valentin Ludwig for the fruitful discussions, and Dr Francisco Goes (CELPA, Associação da Indústria Papeleira) and Prof. Mário Cerqueira for the provision of data, concerning stand properties and meteorological data.

Disclosure statement

No potential conflict of interest was reported by the authors.

Funding

This study was financially supported by the R&D project ([UID/AGR/00239/2013]) within the research activities of the Forest Research Center, at the Instituto Superior de Agronomia, Universidade de Lisboa. M. Häusler ([PD/BD/52698/2014]) was funded by the Foundation for Science and Technology (FCT, Portugal). J. Keizer and J. P. Nunes ([IF/01465/2015] and [IF/00586/2015]) co-funded by the European Social Fund within the Operational Program Human Potential. The study was also financed by JCCM (project ECOFLUX III, Ref: [PEIC-2014-002-P]) and Fundação para a Ciência e a Tecnologia [IF/00586/2015, IF/01465/2015, PD/BD/52698/2014].

ORCID

Melanie Häusler  <http://orcid.org/0000-0002-3229-7086>
 João P. Nunes  <http://orcid.org/0000-0002-0164-249X>
 Paula Soares  <http://orcid.org/0000-0002-7603-5467>
 Juan M. Sánchez  <http://orcid.org/0000-0003-1027-9351>
 João M. N. Silva  <http://orcid.org/0000-0001-5201-9836>
 Thorsten Warneke  <http://orcid.org/0000-0001-5185-3415>
 Jan Jacob Keizer  <http://orcid.org/0000-0003-4833-0415>
 José M. C. Pereira  <http://orcid.org/0000-0003-2583-3669>

References

- AFN. 2010. *IFN5 2005–2006, Inventário Florestal Nacional, Portugal Continental*. Technical Report. Lisbon, Portugal: Direção de Unidade de Defesa da Floresta, Autoridade Florestal Nacional.
- Allen, R. G., L. S. Pereira, D. Raes, and M. Smith. 1998. *FAO Irrigation and Drainage Paper No. 56, Crop Evapotranspiration (guidelines for computing crop water requirements)*. Rome, Italy.
- Arán, D., J. García-Duro, O. Reyes, and M. Casal. 2013. "Fire and Invasive Species: Modifications in the Germination Potential of *Acacia Melanoxylon*, *Conyza Canadensis* and *Eucalyptus Globulus*." *Forest Ecology and Management* 302: 7–13. doi:10.1016/j.foreco.2013.02.030.
- Barsi, J. A., J. L. Barker, and J. R. Schott. 2003. "An Atmospheric Correction Parameter Calculator for a Single Thermal Band Earth-Sensing Instrument." In *IGARSS 2003. 2003 IEEE Int. Geosci. and Rem. Sen. Symp. Proceedings (IEEE Cat. No.03CH37477)*, Vol. 5, 3014–3016. Toulouse: IEEE.
- Bastos, A., C. M. Gouveia, C. C. DaCamara, and R. M. Trigo. 2011. "Modelling Post-Fire Vegetation Recovery in Portugal." *Biogeo sciences* 8 (12): 3593–3607. doi:10.5194/bg-8-3593-2011.
- Berk, A. 1999. "MODTRAN4 Radiative Transfer Modeling for Atmospheric Correction." *Proceedings SPIE* 3756 (1993): 348–353.
- Bond-Lamberty, B., S. D. Peckham, S. T. Gower, and B. E. Ewers. 2009. "Effects of Fire on Regional Evapotranspiration in the Central Canadian Boreal Forest." *Global Change Biology* 15 (5): 1242–1254. doi:10.1111/j.1365-2486.2008.01776.x.
- Bosch, J. M., and J. D. Hewlett. 1982. "A Review of Catchment Experiments to Determine the Effect of Vegetation Changes on Water Yield and Evapotranspiration." *Journal Hydrol of Hydrology* 55 (1–4): 3–23. doi:10.1016/0022-1694(82)90117-2.
- Boulet, A. K., S. A. Prats, M. C. Malvar, O. González-Pelayo, C. O. A. Coelho, A. J. D. Ferreira, and J. J. Keizer. 2015. "Surface and Subsurface Flow in *Eucalyptus* plantations in North-Central Portugal." *Journal Hydrol Hydromech* 63 (3): 193–200. doi:10.1515/johh-2015-0015.
- Buckley, T. N., T. L. Turnbull, S. Pfautsch, M. Gharun, and M. A. Adams. 2012. "Differences in Water Use between Mature and Post-Fire Regrowth Stands of Subalpine *Eucalyptus Delegatensis* R. Baker." *Forest Ecology and Management* 270: 1–10. doi:10.1016/j.foreco.2012.01.008.
- Carlson, T. 2007. "An Overview of the "Triangle Method" for Estimating Surface Evapotranspiration and Soil Moisture from Satellite Imagery." *Sensors* 7 (8): 1612–1629. doi:10.3390/s7081612.

- Catry, F. X., F. Moreira, R. Tujeira, and J. S. Silva. 2013. "Post-Fire Survival and Regeneration of Eucalyptus Globulus in Forest Plantations in Portugal." *Forest Ecology and Management* 310: 194–203. doi:10.1016/j.foreco.2013.08.036.
- Clothier, B. E., K. L. Clawson, P. J. Pinter, M. S. Moran, R. J. Reginato, and R. D. Jackson. 1986. "Estimation of Soil Heat Flux from Net Radiation during the Growth of Alfalfa." *Agricultural Forest Manage* 37 (4): 319–329. doi:10.1016/0168-1923(86)90069-9.
- Cocke, A. E., P. Z. Fulé, and J. E. Crouse. 2005. "Comparison of Burn Severity Assessments Using Differenced Normalized Burn Ratio and Ground Data." *International Journal Wildland Fire* 14 (2): 189. doi:10.1071/WF04010.
- Cristóbal, J., R. Poyatos, M. Ninyerola, P. Llorens, and X. Pons. 2011. "Combining Remote Sensing and GIS Climate Modelling to Estimate Daily Forest Evapotranspiration in a Mediterranean Mountain Area." *Hydrol Earth Systems Sciences* 15 (5): 1563–1575. doi:10.5194/hess-15-1563-2011.
- Cristóbal, J., A. Prakash, M. C. Anderson, P. William, E. Kustas, S. Euskirchen, and D. L. Kane. 2017. "Estimation of Surface Energy Fluxes in the Arctic Tundra Using the Remote Sensing Thermal-Based Two-Source Energy Balance Model." *Hydrol Earth Systems Sciences* 21 (June): 1339–1358. doi:10.5194/hess-21-1339-2017.
- David, T. S., M. O. Henriques, C. Kurz-Besson, J. Nunes, F. Valente, M. Vaz, J. S. Pereira et al. 2007. "Water-Use Strategies in Two Co-Occurring Mediterranean Evergreen Oaks: Surviving the Summer Drought." *Tree Physiology* 27 (6): 793–803. doi:10.1093/treephys/27.6.793.
- de Almeida, P. A., and H. Riekerk. 1990. "Water Balance of Eucalyptus Globulus and Quercus Suber Forest Stands in South Portugal." *Forest Ecology Manage* 38 (1–2): 55–64. doi:10.1016/0378-1127(90)90085-P.
- de Bruin, H. A. R., and A. A. M. Holtslag. 1982. "A Simple Parameterization of the Surface Fluxes of Sensible and Latent Heat during Daytime Compared with the Penman-Monteith Concept." *Journal Applications Meteorol* 21 (11): 1610–1621. doi:10.1175/1520-0450(1982)021<1610:ASPOTS>2.0.CO;2.
- Du, J., K. Song, Z. Wang, B. Zhang, and D. Liu. 2013. "Evapotranspiration Estimation Based on MODIS Products and Surface Energy Balance Algorithms for Land (SEBAL) Model in Sanjiang Plain, Northeast China." *Chinese Geographic Science* 23 (1): 73–91. doi:10.1007/s11769-013-0587-8.
- Escuin, S., R. Navarro, and P. Fernández. 2008. "Fire Severity Assessment by Using NBR (Normalized Burn Ratio) and NDVI (Normalized Difference Vegetation Index) Derived from LANDSAT TM/ETM Images." *International Journal of Remote Sensing* 29 (4): 1053–1073. doi:10.1080/01431160701281072.
- García, M. J. L., and V. Caselles. 1991. "Mapping Burns and Natural Reforestation Using Thematic Mapper Data." *Geocarto International* 6 (1): 31–37. doi:10.1080/10106049109354290.
- García-Estringana, P., N. Alonso-Blázquez, and J. Alegre. 2010. "Water Storage Capacity, Stemflow and Water Funneling in Mediterranean Shrubs." *Journal of Hydrology* 389 (3–4): 363–372. doi:10.1016/j.jhydrol.2010.06.017.
- Ghassam, A. 1989. *Theory and Applications of Optical Remote Sensing*. Washington, D.C.: John Wiley & Sons.
- Glenn, E. P., T. M. Doody, J. P. Guerschman, A. R. Huete, E. A. King, T. R. McVicar, A. I. J. M. Van Dijk, T. G. Van Niel, M. Yebra, and Y. Zhang. 2011. "Actual Evapotranspiration Estimation by Ground and Remote Sensing Methods: The Australian Experience." *Hydrological Processes* 25 (26): 4103–4116. doi:10.1002/hyp.8391.
- Häusler, M., N. Conceição, L. Tezza, J. M. Sánchez, M. L. Campagnolo, A. J. Häusler, J. M. N. Silva, T. Warneke, G. Heygster, and M. I. Ferreira. 2018. "Estimation and Partitioning of Actual Daily Evapotranspiration at an Intensive Olive Grove Using the STSEB Model Based on Remote Sensing." *Agricultural Water Manage* 201C: 188–198. doi:10.1016/j.agwat.2018.01.027.
- Häusler, M., J. M. N. Silva, S. Cerasoli, G. López-Saldaña, and J. M. C. Pereira. 2016. "Modelling Spectral Reflectance of Open Cork Oak Woodland: A Simulation Analysis of the Effects of Vegetation Structure and Background." *International Journal Rem Sen* 37 (3): 492–515. doi:10.1080/01431161.2015.1134847.
- Hawtree, D., J. P. Nunes, J. J. Keizer, R. Jacinto, J. Santos, M. E. Rial-Rivas, A. K. Boulet, F. Tavares-Wahren, and K. H. Feger. 2015. "Time Series Analysis of the Long-Term Hydrologic Impacts of

- Afforestation in the Águeda Watershed of North-Central Portugal." *Hydrol Earth Systems Sciences* 19 (7): 3033–3045. doi:10.5194/hess-19-3033-2015.
- Hengl, T., G. B. M. Heuvelink, M. P. Tadić, and E. J. Pebesma. 2012. "Spatio-Temporal Prediction of Daily Temperatures Using Time-Series of MODIS LST Images." *Theoretical and Applied Climatology* 107 (1–2): 265–277. doi:10.1007/s00704-011-0464-2.
- Hibbert, A. R. 1967. "Forest Treatment Effects on Water Yield." In *Forest hydrology: proceedings of a National Science Foundation Advanced Science Seminar*, 527–543. University Park, PA: Pergamon
- Hirano, T., K. Suzuki, and R. Hirata. 2017. "Energy Balance and Evapotranspiration Changes in a Larch Forest Caused by Severe Disturbance during an Early Secondary Succession." *Agr Forest Meteorol* 232: 457–468. doi:10.1016/j.agrformet.2016.10.003.
- Humes, K., R. Hardy, W. Kustas, J. Prueger, and P. Starks. 2004. "High Spatial Resolution Mapping of Surface Energy Balance Components with Remotely Sensed Data." In *Thermal Remote Sensing in Land Surface Processing* Chap,3, 110–132. New York: CRC Press.
- ICNF. 2013a. *6 Inventário Florestal Nacional, Áreas Dos Usos Do Solo E Das Espécies Florestais De Portugal Continental, 1995, 2005, 2010, Resultados Preliminares*. Technical Report. Lisbon, Portugal: Instituto da Conservação da Natureza e Florestas.
- ICNF. 2013b. *Áreas Ardidas Por Tipo De Ocupação Do Solo (1996–2012)*. Technical Report. Instituto da Conservação da Natureza e das Florestas.
- Idso, S. B., J. K. Aase, and R. D. Jackson. 1975. "Net Radiation Soil Heat Flux Relations as Influenced by Soil Water Content Variations." *Boundary-Layer Meteorol* 9 (1): 113–122. doi:10.1007/BF00232257.
- Iroumé, A., and H. Palacios. 2013. "Afforestation and Changes in Forest Composition Affect Runoff in Large River Basins with Pluvial Regime and Mediterranean Climate, Chile." *Journal Hydrol* 505: 113–125. doi:10.1016/j.jhydrol.2013.09.031.
- Jimenez-Munoz, J. C., J. A. Sobrino, D. Skokovic, C. Mattar, and J. Cristobal. 2014. "Land Surface Temperature Retrieval Methods from Landsat-8 Thermal Infrared Sensor Data." *IEEE Geosci and Remote Sensor Letters* 11 (10): 1840–1843. doi:10.1109/LGRS.2014.2312032.
- JRC Scientific and Technical Report. 2008. "Forest Fires in Europe 2008.", Italy: Ispra (VA).
- Kang, S., J. S. Kimball, and S. W. Running. 2006. "Simulating Effects of Fire Disturbance and Climate Change on Boreal Forest Productivity and Evapotranspiration." *Science of the Total Environment* 362 (1–3): 85–102. doi:10.1016/j.scitotenv.2005.11.014.
- Kasim, A. A., and A. A. Usman. 2016. "Triangle Method for Estimating Soil Surface Wetness from Satellite Imagery in Allahabad District, Uttar Pradesh, India." *Journal Geosci and Environment Protection* 4 (January): 84–92.
- Key, C. H., and N. C. Benson. 1999. "Measuring and Remote Sensing of Burn Severity." In *Proceedings Joint Fire Science Conference and Workshop*, edited by K. C. Neuenschwander and L. F. Ryan, 284. Moscow: Univ. of Idaho.
- Köppen, W. 1936. "Das Geographische System Der Klimate." In *Handbuch Der Klimatologie*, 44. Berlin, Germany: Gebrüder Borntraeger.
- Kustas, W. P., and C. S. T. Daughtry. 1990. "Estimation of the Soil Heat Flux/Net Radiation Ratio from Spectral Data." *Agricultural Forest Meteorol* 49 (3): 205–223. doi:10.1016/0168-1923(90)90033-3.
- Lane, P. N. J., P. M. Feikema, C. B. Sherwin, M. C. Peel, and A. C. Freebairn. 2010. "Modelling the Long Term Water Yield Impact of Wildfire and Other Forest Disturbance in Eucalypt Forests." *Environmental Modelling & Software* 25: 467–478. doi:10.1016/j.envsoft.2009.11.001.
- Langford, K. J. 1976. "Change in Yield of Water following a Bushfire in a Forest of *Eucalyptus regnans*." *Journal Hydrol* 29 (1–2): 87–114. doi:10.1016/0022-1694(76)90007-X.
- Liou, Y.-A., and S. Kar. 2014. "Evapotranspiration Estimation with Remote Sensing and Various Surface Energy Balance Algorithms – A Review." *Energies* 7 (5): 2821–2849. doi:10.3390/en7052821.
- Liu, H., J. Shi, and E. Erdem. 2010. "Prediction of Wind Speed Time Series Using Modified Taylor Kriging Method." *Energy* 35 (12): 4870–4879. doi:10.1016/j.energy.2010.09.001.
- Luke, R. H., and A. G. McArthur. 1978. *Bushfires in Australia*. Canberra: CSIRO Division of Forestry Research.
- Maia, P., J. G. Pausas, A. Vasques, and J. J. Keizer. 2012. "Fire Severity as a Key Factor in Post-Fire Regeneration of *Pinus pinaster* (Ait.) In Central Portugal." *Annals of Forest Science* 69 (4): 489–498. doi:10.1007/s13595-012-0203-6.

- Miller, J. D., and H. Safford. 2012. "Trends in Wildfire Severity: 1984 to 2010 in the Sierra Nevada, Modoc Plateau, and Southern Cascades, California, USA." *Fire Ecology* 8 (3): 41–57. doi:10.4996/fireecology.0803041.
- Mirra, I. M., T. M. Oliveira, M. G. Ana Barros, and P. M. Fernandes. 2017. "Fuel Dynamics following Fire Hazard Reduction Treatments in Blue Gum (*Eucalyptus Globulus*) Plantations in Portugal." *Forest Ecology and Management* 398 (August): 185–195. doi:10.1016/j.foreco.2017.05.016.
- Montes-Helu, M. C., T. Kolb, S. Dore, B. Sullivan, S. C. Hart, G. Koch, and B. A. Hungate. 2009. "Persistent Effects of Fire-Induced Vegetation Change on Energy Partitioning and Evapotranspiration in Ponderosa Pine Forests." *Agriculture Forest Meteorol* 149 (3–4): 491–500. doi:10.1016/j.agrformet.2008.09.011.
- Nolan, R. H., P. N. J. Lane, R. G. Benyon, R. A. Bradstock, and P. J. Mitchell. 2015. "Trends in Evapotranspiration and Streamflow following Wildfire in Resprouting Eucalypt Forests." *Journal Hydrol* 524: 614–624. doi:10.1016/j.jhydrol.2015.02.045.
- Nolan, R. H., P. N. J. Lane, R. G. Benyon, R. A. Bradstock, and P. J. Mitchell. 2014. "Changes in Evapotranspiration following Wildfire in Resprouting Eucalypt Forests." *Ecohydrol* 7 (5): 1363–1377.
- Norman, J. M., W. Kustas, and K. Humes. 1995. "A Two-Source Approach for Estimating Soil and Vegetation Energy Fluxes from Observations of Directional Radiometric Surface Temperature." *Agr Forest Meteorol* 77: 263–293. doi:10.1016/0168-1923(95)02265-Y.
- Nunes, J. P., M. Malvar, A. A. Benali, E. R. María Rivas, and J. J. Keizer. 2016. "A Simple Water Balance Model Adapted for Soil Water Repellency: Application on Portuguese Burned and Unburned Eucalypt Stands." *Hydrol. Processes* 30 (3): 463–478. doi:10.1016/j.rse.2007.07.018.
- Palma, J. H. N. Jan. 2013. "Web-Globulus 3.0." Accessed 01 Jan 2016. http://home.isa.utl.pt/joao_palma/modelos/webglobulus/.
- Rehman, S., and S. G. Ghorri. 2000. "Spatial Estimation of Global Solar Radiation Using Geostatistics." *Renewable Energy* 21 (3–4): 583–605. doi:10.1016/S0960-1481(00)00078-1.
- Rubio, E., V. Caselles, and C. Badenas. 1997. "Emissivity Measurements of Several Soils and Vegetation Types in the 8–4 M Wave Band: Analysis of Two Field Methods." *Remote Sensor Environment* 59: 490–521. doi:10.1016/S0034-4257(96)00123-X.
- Sánchez, J. M., M. Bisquert, E. Rubio, and V. Caselles. 2015. "Impact of Land Cover Change Induced by a Fire Event on the Surface Energy Fluxes Derived from Remote Sensing." *Remote Sensor* 7 (11): 14899–14915. doi:10.3390/rs71114899.
- Sánchez, J. M., V. Caselles, R. Niçlòs, C. Coll, and W. P. Kustas. 2009. "Estimating Energy Balance Fluxes above a Boreal Forest from Radiometric Temperature Observations." *Agricultural Forest Meteorol* 149 (6–7): 1037–1049. doi:10.1016/j.agrformet.2008.12.009.
- Sánchez, J. M., V. Caselles, R. Niçlòs, E. Valor, C. Coll, and T. Laurila. 2007. "Evaluation of the B-Method for Determining Actual Evapotranspiration in a Boreal Forest from MODIS Data." *International Journal Rem Sen* 28 (6): 1231–1250. doi:10.1080/01431160600928617.
- Sánchez, J. M., W. P. Kustas, V. Caselles, and M. C. Anderson. 2008. "Modelling Surface Energy Fluxes over Maize Using a Two-Source Patch Model and Radiometric Soil and Canopy Temperature Observations." *Remote Sensor Environmental* 112 (3): 1130–1143. doi:10.1016/j.rse.2007.07.018.
- Sánchez, J. M., R. López-Urrea, E. Rubio, and V. Caselles. 2011. "Determining Water Use of Sorghum from Two-Source Energy Balance and Radiometric Temperatures." *Hydrol Earth Systems Sciences* 15 (10): 3061–3070. doi:10.5194/hess-15-3061-2011.
- Santos, J. M., F. G. A. Verheijen, F. T. Wahren, A. Wahren, K.-H. Feger, L. Bernard-Jannin, M. E. Rial-Rivas, J. J. Keizer, and J. P. Nunes. 2016. "Soil Water Repellency Dynamics in Pine and Eucalypt Plantations in Portugal – A High-Resolution Time Series." *Land Degradation & Development* 27 (5): 1334–1343. doi:10.1002/ldr.2251.
- Scott, R. L., W. James Shuttleworth, D. C. Goodrich, and T. Maddock. 2000. "The Water Use of Two Dominant Vegetation Communities in a Semiarid Riparian Ecosystem." *Agricultural Forest Meteorol* 105 (1–3): 241–256. doi:10.1016/S0168-1923(00)00181-7.

- Seguin, B., and B. Itier. 1983. "Using Midday Surface Temperature to Estimate Daily Evaporation from Satellite Thermal IR Data." *International Journal Rem Sen* 4 (2): 371–383. doi:10.1080/01431168308948554.
- Shakesby, R. A., D. O. Celeste, A. Coelho, A. D. Ferreira, J. P. Terry, and P. D.R Walsh. 1993. "Wildfire Impacts on Soil Erosion and Hydrology in Wet Mediterranean Forest, Portugal." *International Journal Wildland Fire* 3 (2): 95–110. doi:10.1071/WF9930095.
- Silva, J. M. N., H. Feith, and J. M. C. Pereira. 2007. "Exploração E Silvicultura Pós-Fogo Em Eucaliptais." In *O Eucaliptal Em Portugal: Impactes Ambientais E Investigação Científica Chap. 9*, edited by J. M. N. Alves, A. M. Pereira, and J. S. Silva, 285–312, Lisbon, Portugal: ISAPress.
- Silva, J. S., F. C. Rego, and S. Mazzoleni. 2002. "Fire Effects on Soil Water Dynamics in a Mediterranean Shrubland." In *Forest Fire Research & Wildland Fire Safety*, edited by D. X. Viegas, 1–11. Rotterdam: Millpress.
- Sobrino, J. A., M. Gómez, J. C. Jiménez-Muñoz, A. Olioso, and G. Chehbouni. 2005. "A Simple Algorithm to Estimate Evapotranspiration from DAIS Data: Application to the DAISEX Campaigns." *Journal Hydrol* 315 (1–4): 117–125. doi:10.1016/j.jhydrol.2005.03.027.
- Sobrino, J. A., J. C. Jiménez-Muñoz, and L. Paolini. 2004. "Land Surface Temperature Retrieval from LANDSAT TM 5." *Remote Sensor Environmental* 90 (4): 434–440. doi:10.1016/j.rse.2004.02.003.
- Spracklen, D. V., S. R. Arnold, and C. M. Taylor. 2012. "Observations of Increased Tropical Rainfall Preceded by Air Passage over Forests." *Nature* 489: 282–285. doi:10.1038/nature11390.
- Tessler, N., L. Wittenberg, and N. Greenbaum. 2016. "Vegetation Cover and Species Richness after Recurrent Forest Fires in the Eastern Mediterranean Ecosystem of Mount Carmel, Israel." *Science of the Total Environment* 572 (1): 1395–1402. doi:10.1016/j.scitotenv.2016.02.113.
- Tomé, M., T. Oliveira, and P. Soares. 2006. *O Modelo GLOBULUS 3.0 Dados E Equações*. Technical Report. Lisbon, Portugal: Departamento de Engenharia Florestal, Instituto Superior de Agronomia.
- Tursilowati, L., J. Tetuko, S. Sumantyo, H. Kuze, and E. S. Adiningsih. 2012. "Surface Energy Balance Method into Remote Sensing Application and GIS for Drought Monitoring in Bandung, Indonesia Corresponding Author: Laras Tursilowati." *Journal of Emerging Trends in Engineering and Applications Sciences (JETEAS)* 3 (3): 394–400.
- Ueyama, M., K. Ichii, E. S. Hiroki Iwata, D. Z. Euskirchen, A. V. Rocha, Y. Harazono, C. Iwama, T. Nakai, and W. C. Oechel. 2014. "Change in Surface Energy Balance in Alaska Due to Fire and Spring Warming, Based on Upscaling Eddy Covariance Measurements." *Journal of Geophysical Research: Biogeosciences* 119 (10): 1947–1969.
- Valor, E., and V. Caselles. 1996. "Mapping Land Surface Emissivity from NDVI. Application to European, African and South-American Areas." *Remote Sensor Environmental* 57: 167–184. doi:10.1016/0034-4257(96)00039-9.
- Valor, E., and V. Caselles. 2005. *Validation of the Vegetation Cover Method for Land Surface Emissivity Estimation*. Kerala: Research Signpost.
- Venturini, V., S. Islam, G. Bisht, and L. Rodriguez. 2008. "Estimation of Evaporative Fraction and Evapotranspiration from MODIS Products Using a Complementary Based Model." *Remote Sensor Environmental* 112 (1): 132–141. doi:10.1016/j.rse.2007.04.014.
- Veraverbeke, S., S. Lhermitte, W. W. Verstraeten, and R. Goossens. 2010. "The Temporal Dimension of Differenced Normalized Burn Ratio (Dnbr) Fire/Burn Severity Studies: The Case of the Large 2007 Peloponnese Wildfires in Greece." *Remote Sensor Environment* 114 (11): 2548–2563. doi:10.1016/j.rse.2010.05.029.
- Wahren, T., S. J. Filipa, J. P. Nunes, O. Gonzalez-Pelayo, D. Hawtree, K. H. Feger, and J. J. Keizer. 2016. "Combining Digital Soil Mapping and Hydrological Modeling in a Data Scarce Watershed in North-Central Portugal." *Geoderma* 264: 350–362. doi:10.1016/j.geoderma.2015.08.023.
- Wang, F., Z. Qin, C. Song, T. Lili, A. Karnieli, and S. Zhao. 2015. "An Improved Mono-Window Algorithm for Land Surface Temperature Retrieval from Landsat 8 Thermal Infrared Sensor Data." *Remote Sensor* 7 (4): 4268–4289. doi:10.3390/rs70404268.
- Wassenaar, T., A. Olioso, C. Hasager, F. Jacob, and A. Chehbouni. 2002. "Estimation of Evapotranspiration on Heterogeneous Pixels." In *Proceedings of the First Int. Symp. on Recent*

Advances in Quantitative Rem. Sen., edited by J. A. Sobrino, pp. 458–465. València: Publicacions de la Universitat de València.

Watson, F. G. R., R. A. Vertessy, T. A. McMahon, B. G. Rhodes, and I. S. Watson. 1999. *The hydrologic impacts of forestry on the Maroondah catchments*. Technical Report 99/1.

Whelan, A., G. Starr, C. L. Staudhammer, H. W. Loescher, and R. J. Mitchell. 2015. "Effects of Drought and Prescribed Fire on Energy Exchange in Longleaf Pine Ecosystems." *Ecosphere* 6 (7): art128–art128. doi:[10.1890/ES15-00111.1](https://doi.org/10.1890/ES15-00111.1).

Wilson, M. F., and A. Henderson-Sellers. 1985. "A Global Archive of Land Cover and Soils Data for Use in General Circulation Climate Models." *Journal of Climatology* 5: 119–143. doi:[10.1002/joc.3370050202](https://doi.org/10.1002/joc.3370050202).

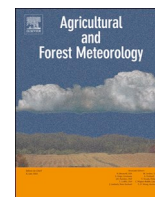
Yang, Y., S. Hongbo, R. Zhang, J. Tian, and L. Lu. 2015. "An Enhanced Two-Source Evapotranspiration Model for Land (EEML): Algorithm and Evaluation." *Remote Sensor Environment* 168: 54–65. doi:[10.1016/j.rse.2015.06.020](https://doi.org/10.1016/j.rse.2015.06.020).

A promising new approach to estimate drought indices for fire danger assessment using remotely sensed data (Article III)

In this third part, the improvement of soil moisture estimations SMD from drought indices was investigated, by replacing empirical equations from evapotranspiration with ET_a from the STSEB model. Soil moisture is related to fuel moisture content and therefore, with decreasing water content, to fire danger. The method described in Chapter 5 to estimate the soil moisture deficit for fire danger rating was also tested at a study site in Indonesia, where the results are provided in the section of Supplemental material D of the manuscript.

This chapter was published at the journal of *Agriculture and Forest Meteorology*, 2019, ©Elsevier B.V., available online: <https://doi.org/10.1016/j.agrformet.2019.04.015> (impact factor of 4.039, 5-year impact factor of 5.035)

Melanie Häusler, João P. Nunes, João M. N. Silva, Jan Jacob Keizer, Thorsten Warneke, and José M. C. Pereira.



A promising new approach to estimate drought indices for fire danger assessment using remotely sensed data



Melanie Häusler^{a,*}, João P. Nunes^b, João M.N. Silva^a, Jan Jacob Keizer^c, Thorsten Warneke^d, José M.C. Pereira^a

^a Forest Research Centre, School of Agriculture, University of Lisbon, Tapada da Ajuda, 1349-017 Lisbon, Portugal

^b CE3C – Centre for Ecology, Evolution and Environmental Changes, Faculdade de Ciências, Universidade de Lisboa, 1749-016 Lisboa, Portugal

^c CESAM, Centre for Environmental and Marine Studies, Department of Environment and Planning, University of Aveiro, Aveiro, Portugal

^d Institute of Environmental Physics, University of Bremen, 28359 Bremen, Germany

ARTICLE INFO

Keywords:

Fire danger rating
Two-source energy balance model
Soil moisture deficit
MODIS

ABSTRACT

One of the crucial input variables in fire danger rating systems is the water content of the soil, as well as of the living and dead fuels. This study concentrates on the Keetch-Byram Drought Index (KBDI) and the Drought Code (DC), which are both used to estimate the soil moisture deficit (SMD) and are inherent parts of well-established fire danger rating systems.

These indices assume a simple water balance equation where effective rainfall is the only input and evapotranspiration is the only loss term, retrieved from empirical equations. We propose a method to increase spatial resolution of estimated SMD from KBDI and DC by replacing the empirical estimation of evapotranspiration with the actual evapotranspiration (ET_a) estimated by the remote-sensing based Simplified Two-Source Energy Balance model (STSEB). For the days with no satellite observations, the basal crop coefficient (K_{cb}) and the adjusted crop coefficient ($K_{c,adj}$) approach for water stress conditions were applied to obtain continuous daily estimates for fire danger rating. A new approach was suggested to find a threshold dividing areas into fire-prone and fire-safe, regardless of the status of the drought indices.

Both drought indices (KBDI and DC) benefited from the estimated ET_a of the existing STSEB model obtaining SMD maps with higher spatial resolution (compared to conventional methods and products using interpolation techniques). Areas with higher proneness to drought and therefore to occurrence to fire were identified in the north-central part of Portugal, where e.g. on 16 July 2015, in the case of KBDI 47% of a specific area was classified as fire-prone and about 67% of the fires occurred within the identified area of this year.

This new approach generated information on the water status of the soil at a spatial resolution of 500 m, which can be useful for forest management to identify endangered areas, as the danger of fire increases with increasing drought conditions.

1. Introduction

In many ecosystems, forest fires are a part of the natural regeneration cycle. However, as the number and size of forest fires in Portugal (Parente et al., 2018) increase (e.g. 508,763 ha in 2017, ICNF, 2018), wildfires mean extreme damage to the environment and the production systems.

For protection, fire rating systems were introduced to warn against the risk of fire at an early stage. The most prominent ones such as the McArthur Forest Fire Danger Index (FFDI, used in Australia, McArthur, 1967) and the Canadian Forest Fire Weather Index System (CFFWIS, used in Canada, Alaska and Portugal), include drought indices, which

are a measure of the dryness of the soil layer (see Drought Code, DC for the deep duff layer, Van Wagner, 1974).

Drought indices are typically driven by weather conditions, as fire danger, fire ignition and spreading are related to air temperature (T_a), wind speed (u) and direction, air humidity and solar irradiance (Sharples et al., 2009). At present, fire danger assessment involves interpolation of weather data from point observations at weather stations. Even in countries with local observations from a dense network of weather stations, interpolation techniques result only in little spatial variation, since they are, overlooking the role of vegetation type and structure (Aguado et al., 2003). Moreover, meteorological variables have considerable limitations for estimating soil moisture content,

* Corresponding author.

E-mail address: aa18795@isa.ulisboa.pt (M. Häusler).

<https://doi.org/10.1016/j.agrformet.2019.04.015>

Received 20 October 2018; Received in revised form 25 March 2019; Accepted 17 April 2019

0168-1923/© 2019 Elsevier B.V. All rights reserved.

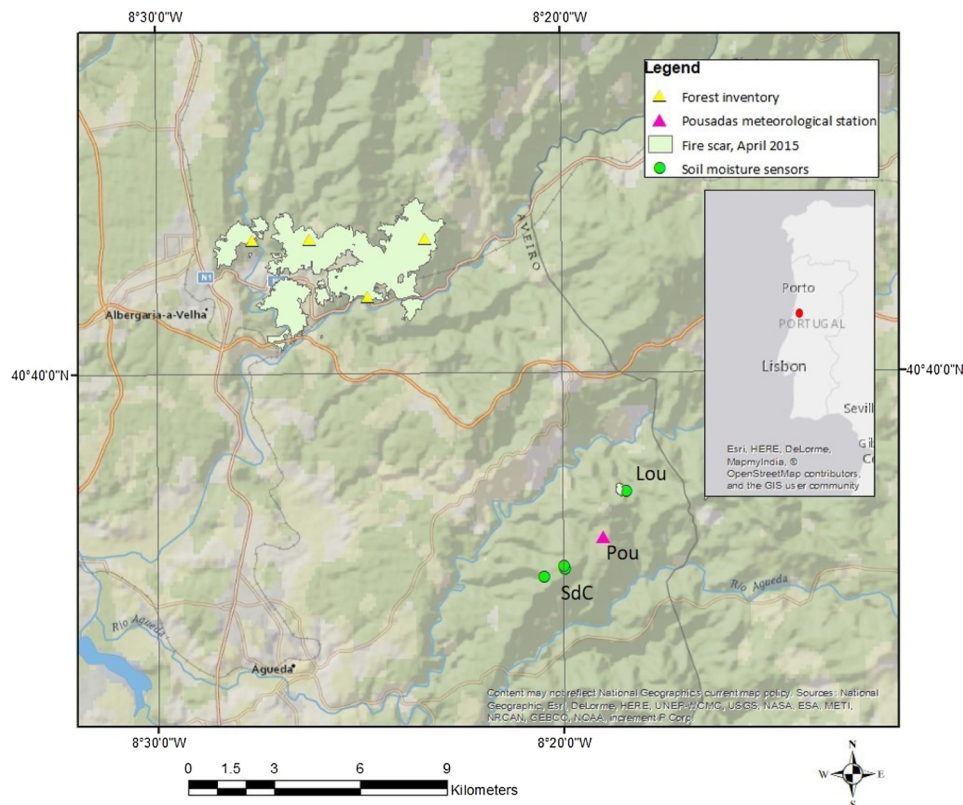


Fig. 1. The map gives an overview of the spring-fire, showing its location, and distances to measurement points. Pou = Pousadas; Lou = Lourizela; SdC = Serra de Cima.

which is a key factor in fire danger. Only recently Krueger et al. (2015) presented a strong relationship between soil moisture and wildfire size for Oklahoma. The authors stressed the necessity to develop innovative approaches that explicitly take soil moisture data into account for assessing fire danger. Over the last years, soil moisture related drought indices were further developed from existing ones or were newly proposed.

Garcia-Prats et al. (2015) developed a version of the KBDI that was adjusted to Mediterranean environments and took into account silvicultural operations (e.g. thinning) that influence the soil moisture content. The KBDI and other drought indices, such as DC or Palmer Drought Index (Palmer, 1965) are based on a simple soil water balance model, where evapotranspiration is assumed to be the only loss term to the water balance. To this end, they modified the coefficients of the empirical equation that includes the estimation of the reference evapotranspiration (ET_0). The ET_0 (or ET_p) constitutes the maximum possible water vapor rate due to the prevailing meteorological conditions, when water supply is unlimited. It is defined as the evaporation from the soil plus the transpiration from a hypothetical reference grass, with a crop height of 0.12 m, a fixed surface resistance of 70 s m^{-1} and an albedo of 0.23 (Allen et al., 1998). ET_0 is often denoted as potential evapotranspiration (ET_p), even though the concept of ET_p has been replaced since the 1970s (Doorenbos and Kassam, 1979; Irmak and Haman, 2003; Allen et al., 1998).

A replacement of the authors' called empirical ET_p equation of KBDI by the Hargreaves and Samani reference evapotranspiration equation (Hargreaves and Samani, 1985) was suggested by Snyder et al. (2006), which also improved the soil moisture deficit (SMD) estimates from KBDI. Ganatsas et al. (2011) adapted the variables of maximum air temperature (T_{\max}), and the mean annual rainfall (MAR; Eq. (4)) to adjust KBDI to Mediterranean conditions. Holgate et al. (2017) suggested to substitute soil moisture estimations from KBDI, with innovative approaches such as the Antecedent Precipitation Index (API)

or with soil moisture products from satellite platforms. This was done by Vinodkumar et al. (2017) and Kerr et al. (2010), who recently investigated API and the Soil Moisture Ocean Salinity product (SMOS) for their suitability in fire danger rating applications, respectively. Both API and SMOS simplified and improved soil moisture estimates.

With the emergence of satellite imagery, nearly daily and worldwide coverage of soil moisture data are provided (e.g. SMOS). The downside of satellite soil moisture products is the spatial resolution of several kilometers (e.g. SMOS; Level 3, with an average spatial resolution of about 40 km), which is rather coarse for operational fire management (Carlson and Burgan, 2003). Typically, fire danger ratings from data of weather stations are either provided as interpolated maps or gridded with a spatial resolution between 1 km^2 and 9 km^2 (Carlson and Burgan, 2003; DaCamara et al., 2015).

In this study we aim to:

- i. incorporate the estimated ET_a from the Simplified Two-Source Energy Balance model (STSEB, Sánchez et al., 2008; Häusler et al., 2018b) into drought indices,
- ii. provide higher spatial resolution of KBDI and DC, using satellite observations,
- iii. test two different coefficients to obtain the drought indices for days with no satellite observations, and
- iv. find a threshold for drought indices to identify areas which are more fire-prone than others.

The goal of this work is to spatially enhance soil water balance estimation and thus to improve fire danger rating by identifying areas that are at risk of faster soil drying.

The STSEB model makes use of the MODerate-resolution Imaging Spectroradiometer (MODIS) that has an almost daily coverage with a pixel size of 500 m. The spatial resolution of the estimated soil water deficit from KBDI and DC (obtained with ET_a from STSEB, using MODIS

imagery) presented here is therefore higher compared to conventional products (e.g. pixel size of 3 km, fire risk product of LSA SAF). The modified drought indices were applied to the example of a (1) spring fire and an (2) extended fire-affected area at the Caramulo mountain range in Portugal, 2015.

2. Materials and methods

2.1. Study area

This study concerns a fire-affected area in the Caramulo mountain range, which is 20 to 30 km inland from the city of Aveiro, in the north-central part of Portugal (Fig. 1). The humid Mediterranean climate classifies as the Csb type (Belda et al., 2014) with high annual rainfall between 750 and 2000 mm. The main precipitation regularly occurs during the cooler winter months, resulting in biomass production and accumulating fire fuels, while the warmer and dry summer months promote wildfires. We investigated spring and summer wildfires that occurred in 2015, which has been a particular dry year and fire occurrences above the average since 2003. In particular, we studied a spring wildfire (2 to 6 April 2015) that burned 1.5-ha of eucalypt plantations (*Eucalyptus globulus* Labill.), and a comprised area affected by spring and summer fires of about 6400 km², from which 108.6 km² were burnt and the greatest part was classified as forests (75 km²). Only 2.9-ha were burned for agricultural use and the rest was unidentified.

For the eucalypt trees an average height of 15.3 m was estimated from a web application (Web-Globulus 3.0 version available at Palma (2013), see also Häusler et al., 2018b), with a tree density of about 580 trees per ha, and an average age of 11 years, in their second and third rotation as input. Comparing tree heights from forest inventory, the height of 15.3 m showed also to be a good fit as average tree height for the larger forest area that was investigated. The STSEB model operates independently from the vegetation type, and differences of ± 1 m tree height result in biases smaller than 1–2% of ET_a (Sánchez et al., 2008).

The soils are shallow (from 20 cm down to 100 cm) with humic Cambisols and Leptosols as the principle soil types. Their textures range from sandy loam to silt loam, and have a high stone content. Granite and schist form the almost impermeable bedrock. Further details about the soil properties are given by Shakesby et al. (1993) and Wahren et al. (2016).

2.2. Meteorological data and remote sensing

The Pousadas meteorological station provided the instantaneous (at satellite overpass) measurements of air temperature (T_a , °C), wind speed (u , m s⁻¹), global solar radiation (S , kJ m⁻²) and daily precipitation (mm) to run the STSEB model. For the estimation of the SMD over a larger area these variables were interpolated from the measurements taken at the weather stations given in Table 1. Maps were created using the ordinary kriging technique (Liu et al., 2010; Rehman and Ghorri, 2000; Hengl et al., 2012; Mukhopadhyaya, 2016) and were used for the model.

For the year 2015, 46 cloudless images for tile 17/4 from MODIS/Terra imagery were processed, which are distributed by LAADS DAAC. The reflectance values of the near-infrared band (NIR) and the red band (RED) were taken from the daily product of MOD09GQ.006 (V006, level-2) with a grid size of 250 m. The surface albedo product was given by MCD43A3.006. The land surface temperature (T_{rad} , K) was obtained from the split-window algorithm as the swath product MOD11L2.006, which has a pixel size of 1000 m. The product of T_{rad} had to be re-processed with the geolocation product of MOD03.006. For the processing of all MODIS products, the MODIS tools for swath and raster products were used and scaled to a spatial resolution of 500 m.

The Spinning Enhanced Visible and Infrared Imager (SEVIRI) aboard Meteosat provided the incident long-wave radiation (L_{sky} , W m⁻²) with a temporal resolution of 30 min. At satellite overpass the

Table 1

Location of the meteorological stations are given. Daily point measurements of T_a , u , GSR , and precipitation were taken and used for interpolating the data (ordinary kriging) over the study area.

Meteorological station	Latitude (°)	Longitude (°)	Elevation (m)
Pousadas	40.6144	-8.3166	432
Viseu/C. C.	40.7149	-7.8959	636
Aveiro/Universidade	40.6354	-8.6596	5
Anadia	40.4388	-8.4399	45
Arouca	40.9269	-8.2611	270

values for L_{sky} were downloaded from the EUMETSAT Satellite Application Facility on Land Surface Analysis (LSA SAF) with a spatial resolution of 3×3 km. Over large areas the L_{sky} is rather uniform when the sky is unclouded (Humes et al., 2004), therefore the average value for L_{sky} , covering the corresponding test site was further processed.

2.3. Soil properties and measurements

The soil characteristics were determined at three different sites (Serra de Cima = SdC, Lourizela = Lou, Macieira de Alcôba = MdA). The soil water content was measured at different soil depths (e.g. SdC at two depths ranges between 0–50 and 50–100 mm), using either a hand-held probe (Decagon, EC-5 sensors at SdC and Lou) or permanently installed Decagon EC-5 sensors with recordings taken in 15 min intervals and stored with a Decagon data logger at SdC. The continues measurements of the soil water content were later used to be compared with the estimates of KBDI and DC (Fig. 4). The soil water retention was obtained from soil samples in the laboratory (pressure plate method and, for SdC, also evaporation method) to determine the permanent wilting point (PWP) and the field capacity (FC). The FC was defined at pF-value¹ of 2.54 with 0.32, and the PWP at pF-value of 4.2 with 0.16 volumetric fraction of soil water content, on average. Details for SdC are given by Boulet et al. (2015) and Nunes et al. (2016), and additionally for Lou by Santos et al. (2016). Field characteristics of MdA are described by Nunes et al. (2018). The soil properties such as soil depth, soil composition and soil type are summarized in Table 2.

2.4. Drought indices

Background

Drought indices (Turner, 1972; Keetch and Byram, 1968; Van Wagner, 1974) provide long-term information of the dryness of the soil and duff layer from weather conditions, the plants' water use and the soil water holding capacity. For this study, two drought indices were applied:

- The Keetch-Byram Drought Index (KBDI) that was developed by Keetch and Byram (1968) and is incorporated into the McArthur Forest Fire Danger Index.
- The Drought Code (DC), as part of the Canadian Forest Fire Weather Index System (CFFWI, Van Wagner, 1974), finds its application mainly in Europe, e.g., in Portugal.

The purpose of both indices is to estimate the progress of drought by using a simplified version of the soil water balance equation to observe changes in the soil moisture content. In the following, we would like to highlight the assumptions made for drought indices, where authors assumed runoff, deep percolation, and capillary rise as zero. The empirical equations are merely based on the effective precipitation and ET_a which are assumed to be the only input and output of the water balance

¹ The pF-value refers to the soil moisture retention curve (pF-curve) that gives the relation between soil moisture suction and soil moisture content.

Table 2

List of catchments (Pou = Pousadas, Lou = Lourizela, SdC = Serra de Cima, MdA = Macieira de Alcôba), where soil water content and the soil water retention curve (pF-curve, which is the tension given as the logarithmic value of cm water) were obtained to retrieve average values for field capacity (FC, pF 2.54) and permanent wilting point (PWP, pF 4.2). The measurements from Lourizela are representative for the Pousadas study area. Soil depths (z_1), maximum measurement depths (z_2), soil textures, and pF-curve are given below. The abbreviations Lpu and Cmu stand for Leptosols and Cambisols, respectively.

Catchment	FAO soil type	z_1 (cm)	z_2 (cm)	Soil texture (%)			pF-curve	
				Sand	Silt	Clay	pF 2.54	pF 4.2
Pou and Lou	Lpu	25	25	36	52	12	0.23	0.10
SdC	Cmu	65	33	21–26	56–55	23–19	0.31	0.13
SdC	Lpu	35	35	23	59	18	0.31	0.13
MdA	Cmu	100	50	38–45	45–39	17–16	0.47	0.24
MdA	Cmu	75	38	62–63	24–25	13–12	0.30	0.17
MdA	Lpu	40	40	61	27	12	0.30	0.17

equation, respectively. The value of (P_{eff}) is hereby identical to precipitation minus interception:

$$\Delta SM = I + P_{eff} - ET_a - RO - DP - SF \tag{1}$$

where ΔSM is the change of soil water storage (mm day^{-1}), I is the irrigation (mm day^{-1}), which does not apply for this study, P_{eff} is the precipitation (mm day^{-1}), ET_a is the actual evapotranspiration (mm day^{-1}), RO is the runoff (mm day^{-1}), DP is the deep percolation (mm day^{-1}), and SF is the subsurface flow (mm day^{-1}).

We should stress that for this equation to be valid, one assumes that plants are using water only from the soil layer that was taken as control volume. However, Mediterranean plants that have to withstand contrasts in water availability, develop deep roots and often use water from the subsoil or from even further below. In practical terms, it is very difficult to quantify changes in water storage below the soil. Therefore, the simplified approach, often used in this context, gives a perception of how fast soil water is depleted. In the case of deep roots, this concept should be applied very carefully, due to the fact that after the soil water is depleted (attains the PWP), it is no more valid.

Both drought indices assume an arbitrary soil depth and a type of soil, such that the lower limit represents the storage at field capacity (FC), and the upper limit the permanent wilting point (PWP), with the difference being the water holding capacity e.g., KBDI with 203.2 mm (Keetch and Byram, 1968, 8 in). Such high values are very unrealistic for the conditions of this study area. However, they could represent water taken from deeper soil layers.

To begin with the estimation of the drought indices, a period of abundant precipitation needs to be selected to reach full FC (Keetch and Byram, 1968). Here, the start date was 5 March 2015, after two weeks of heavy precipitation (> 500 mm).

Then, the drought indices are calculated daily, where the only input to the soil water balance is P_{eff} and the only output is ET_a . The P_{eff} is the actual water reaching and infiltrating the soil, after a part of the precipitation was intercepted by the upper vegetation layer. The ET_a cannot as easily be obtained as ET_0 , because it is not only dependent on meteorological conditions, but also on the vegetation type, the soil water status, and non-standard conditions such as the presence of plant diseases, low soil fertility or soil salinity (Allen et al., 1998). However, in the 1970s, researchers used the ET_0 for drought indices, applying to it a reduction function that was supposed to approximate the evapotranspiration to its actual value ET_a .

Thornthwaite (1948)'s equation was used, which estimates ET_0 from temperature and day length, because evapotranspiration depends on sunshine hours and their seasonal variations. This basic concept was adopted by Turner (1972) for the DC and has been partly incorporated by Keetch and Byram (1968) for the KBDI. The assumptions made for the drought indices (DC and KBDI) are given in Table 3 and are in detail discussed by Van Wagner (1985). In the Appendix information about the negative exponential evapotranspiration pattern is given where Fig. 8a shows the evapotranspiration time-lag. Other assumptions such as the reservoir capacity, rainfall interception and effect, presentation

Table 3

Properties and differences between the drought indices DC and KBDI. This table was adopted from (Table 1. Basic properties of drought indexes, Van Wagner, 1985) and additional information was added.

Object	DC	KBDI
Reservoir capacity	100 mm	8 in
Comparison value	100 mm	203.2 mm (8 in.)
Evapotranspiration pattern	Negative exponential	Negative exponential
Time-lag, 25 °C in July	48 days	88 days
Soil material represented	Organic layer, 25 kg m ⁻²	Mineral soil
Rainfall interception	2.8 mm	5.08 mm
Rainfall effect	Reduced to 83%, then additive	Additive
Presentation style	Absolute	Absolute
Scale type	Reverse log scale of reservoir content	Reverse log scale of reservoir content
Frequency of calculation	Daily	Daily

style, scale type and frequency of calculation are covered in the following sections of KBDI and DC computation. For a deeper understanding references to the original sources are provided.

Since the water balance is only valid if ET_a is known, and by analyzing the assumptions made by some scientists (e.g., including vegetation density, setting a limit corresponding to total rainfall) to estimate evapotranspiration, the empirical equations were substituted by the estimated ET_a from STSEB for spatial improvement of the soil water balance. The detailed calculations of KBDI and DC, and the parts replaced by ET_a are explained and referred to below.

Keetch-Byram Drought Index

The KBDI decreases with (P_{eff}) and increases with daily evapotranspiration given as:

$$KBDI_d = KBDI_{d-1} + \delta Q - P_{eff} \tag{2}$$

where $KBDI_d$ is the KBDI on the observation day (mm), $KBDI_{d-1}$ is the KBDI on the day before the observation day (mm), δQ is the change of soil water (soil water depletion in mm) during a certain time of δt , which is one day (24 h) as recommended by Garcia-Prats et al. (2015), and P_{eff} is the net rainfall (mm). P_{eff} represents the actual water reaching and infiltrating the soil depths without interception. Keetch and Byram (1968) defined a threshold of 5.08 mm (0.2 in) of rainfall which must be exceeded to be considered for calculation. Examples of how to obtain P_{eff} are given in Keetch and Byram (1968).

δQ is defined as:

$$\delta Q = \frac{(203.2 - Q) \times (0.968e^{(0.0876 \times T_{max} + 1.552)} - 8.3)}{1 + 10.88e^{(-0.00173 \times MAR)}} \times 10^{-3} \tag{3}$$

where Q in Eq. (3) is the accumulated soil water depletion (mm) and the upper limit of the soil water capacity is 203.2 mm (being 800 i.e. 8 in of water in the original version of Keetch and Byram (1968)). The

maximum air temperature (T_{\max}) is given in °C, and describes the daily ET_0 as a function of T_{\max} (Keetch and Byram, 1968). The mean annual rainfall (MAR) was obtained by the average annual rainfall measurements at the Pousadas station for the years 2014 to 2017 (here: MAR was 1500 mm, on average).

$$ET = \frac{(0.968e^{(0.0876 \times T_{\max} + 1.552)} - 8.3)}{1 + 10.88e^{(-0.00173 \times \text{MAR})}} \quad (4)$$

where ET is the evapotranspiration (mm day^{-1}) and the numerator of Eq. (4) is ET_0 (or ET_p , Keetch and Byram, 1968; Garcia-Prats et al., 2015). Later, ET was substituted by the estimated ET_a of the STSEB model. In order to compare the end result with a scale of 0 to 800, the $KBDI_d$ is multiplied by the factor (100/25.4).

Drought Code

Equivalent to the KBDI, the DC decreases with P_{eff} and increases with daily evapotranspiration given as:

$$DC_d = DC_{d-1} + 0.5ET_0 \quad (5)$$

where DC_d is the DC from the observation day (mm), DC_{d-1} is the DC from the day before the observation day (mm), and ET_0 is the reference evapotranspiration (mm day^{-1}). The ET_0 is halved, because according to Van Wagner (1987) the scale length of the DC is in a sense one-half of the original Stored Moisture Index (Turner, 1966). By taking the half of ET_0 , the evapotranspiration becomes dependent on the reservoir capacity (soil water content), and therefore water is limited. The restriction of water violates the definition of ET_0 . Later, the term of $0.5ET_0$ of Eq. (5) was replaced by the estimated ET_a from STSEB.

The empirical equation for ET_0 is as follows:

$$ET_0 = 0.36 \times T_{\max} + Lf \quad (6)$$

where T_{\max} is the maximum daily air temperature (°C) and Lf is the seasonal correction for day length. This empirical equation to obtain ET_0 (Eq. (6)) was firstly introduced by Thornthwaite and Mather (1955), where Lf changes with latitude and season. For the Caramulo mountain range, following values for Lf were used: January to December with $-0.5, 0.7, 3.5, 6.4, 8.9, 11.0, 12.7, 9.6, 5.9, 1.5, 0.01,$ and -0.4 , respectively. The Lf values were retrieved from meteorological recordings at the Pousadas station (monthly averages for 2014 to 2017), using the equation given by Turner (1972).

The moisture equivalent (RP, Eq. (7)) after rain is expressed as percentage of dry soil (Girardin et al., 2004):

$$RP = \frac{800}{e^{(DC_{d-1}/400)}} + 3.937 \times P_{\text{eff}} \quad (7)$$

where DC_{d-1} is the DC from the previous observation day (mm), P_{eff} is the effective rain calculated from Eq. (8), and 3.937 is a constant to adapt P_{eff} to the metric system.

To obtain the P_{eff} that adds to the water storage after interception of the canopy, following relationship was established:

$$P_{\text{eff}} = 0.83 \times (P_{\text{daily}} - 1.27) \quad (8)$$

where P_{eff} is the effective rainfall, which is only considered for days where P_{daily} exceeds 2.8 mm. The P_{daily} is the actual measured rainfall in the open for one day (24 h).

The current drought status is given by Eq. (9):

$$DC_d = 400 \ln(800/RP) \quad (9)$$

which enters again Eq. (5). The procedure and restrictions to obtain the DC are well described by Turner (1972), Van Wagner (1974), and Girardin et al. (2004). The source code for the CFFWI is provided by Wang et al. (2015).

2.5. STSEB model

To give a full description of the STSEB model is beyond the scope of

this paper. However, a short description of the main assumptions, as well as differences to the recently published applications of the model by Häusler et al. (2018a,b) are given.

The STSEB model is based on the energy balance equation (Eq. (10)):

$$R_n = H + LE + G \quad (10)$$

where R_n is the net flux radiation density (W m^{-2} , Eq. (11)), H is the sensible heat flux density (W m^{-2} , Eq. (12)), LE is the latent heat flux density (W m^{-2}) and G is the soil heat flux density (W m^{-2} , Eq. (15)).

During satellite overpass, the total R_n is obtained as follows:

$$R_n = (1 - \alpha)S + \varepsilon L_{\text{sky}} - \varepsilon \sigma T_{\text{rad}}^4 \quad (11)$$

where α is the albedo (MCD43A3), S is the global solar radiation (kJ m^{-2}), L_{sky} is the incident long-wave radiation (W m^{-2}), ε is the emissivity (obtained by Valor and Caselles, 1996), σ is the Stefan-Boltzmann constant (5.67×10^{-8} , $\text{W m}^{-2} \text{K}^{-4}$), and T_{rad} is the land surface temperature (MOD11L2, K).

The instantaneous values of H is given by:

$$H = P_v H_v + (1 - P_v) H_s \quad (12)$$

where P_v is the partial vegetation cover, retrieved as described by Valor and Caselles (1996). The H_v (Eq. (13)) and H_s (Eq. (14)), are the sensible heat flux densities over pure vegetated (v) and soil (s) pixels at the time of satellite overpass (instantaneous values), and are expressed as:

$$H_v = \rho C_p \frac{T_v - T_a}{r_a^h} \quad (13)$$

$$H_s = \rho C_p \frac{T_s - T_a}{r_a^s + r_a^s} \quad (14)$$

Here, ρ is the air density (kg m^{-3}) and C_p ($\text{kJ kg}^{-1} \text{K}^{-1}$) is the air specific heat at constant pressure. The vegetation temperature T_v and the soil temperature T_s are given in Kelvin (K). The r_a^a is the aerodynamic resistance to heat transfer between the sink levels (s m^{-1}), r_a^h is the aerodynamic resistance to heat transfer between the canopy and the reference height (s m^{-1}), and r_a^s is the aerodynamic resistance to heat flow in the boundary layer immediately above the soil surface (s m^{-1}). The estimations of the aerodynamic resistances r_a (s m^{-1}) for stable and unstable conditions are explained by Sánchez et al. (2008) in the Appendix.

The value of G is obtained as a fraction of R_n with:

$$G = C_G (1 - P_v) R_n \quad (15)$$

For our study, C_G was set to 0.3 (see also Häusler et al., 2018b).

To obtain daily values, the relationship between H and R_n during satellite overpass was taken:

$$\frac{H_i}{R_{ni}} = \frac{H_d}{R_{nd}} \quad (16)$$

which is only representative for cloudless days.

Thus, assuming that G can be neglected on a daily-scale (Seguin and Itier, 1983; Kustas and Daughtry, 1990), the daily LE (or ET_a) is obtained as a residual term, using Eqs. (10) and (16).

2.6. Crop coefficients

The concept of the crop coefficient (K_c) is well-established and has been applied for different crops and environments for decades (Conceição et al., 2017; Ferreira et al., 1996; Testi et al., 2004; Watanabe et al., 2004; Lazzara and Rana, 2010; Zhang et al., 2013; Sánchez et al., 2014; Paço et al., 2014). The value of K_c can be separated into its components, where K_c is the sum of transpiration (K_{cb}) and evaporation (K_e) components, as follows:

$$ET_a = (K_s K_{cb} + K_e) \times ET_0 \quad (17)$$

where $K_s K_{cb} + K_e$ is also denoted as $K_{c,adj}$ (adjusted crop coefficient), which combines the effect of crop transpiration, soil evaporation and water stress into one coefficient, ET_a is the actual evapotranspiration from STSEB, and K_s is the stress coefficient, which is equal to one, when there is no water stress. The value of K_{cb} is the basal crop coefficient, K_e is the soil evaporation coefficient, and ET_0 is the reference evapotranspiration (Eq. (18)).

The value of K_c (or K_{cb} if K_e is equal to zero) is obtained experimentally, in the research context, by measuring ET_a and calculating ET_0 . For practical applications, K_c is generally obtained from tables or algorithms that take into account crop parameters, such as the leaf area index or the ground cover.

With remote sensing techniques, it is possible to estimate vegetation indices that can be related to crop coefficients (Eq. (17)). Some remote sensing techniques allow to estimate crop coefficients for large areas, which is an advantage in the case of heterogeneous landscape or at a field-scale in case of very heterogeneous soil cover. In one of the approaches used here (STSEB model), the simple empirical equations (Eqs. (2) and (5)) were modified to spatially enhance the SMD estimations from the drought indices.

The estimated ET_a from STSEB was included to represent the actual reduction on evapotranspiration with impact on the soil water balance, but this was only feasible for days with satellite observations.

The value of ET_0 was calculated from the FAO Penman-Monteith method with grass parameters (Allen et al., 1998), which is the reference method in water use and irrigation management:

$$ET_0 = \frac{0.408\Delta(R_n - G) + \gamma \frac{900}{T_{mean} + 273} u_2 (e_s - e_a)}{\Delta + \gamma(1 + 0.34u_2)} \quad (18)$$

where Δ is the slope of the vapor pressure curve (kPa, °C), γ is the psychrometric constant (kPa, °C), T_{mean} is the daily mean temperature (°C), u_2 is the wind speed (m s⁻¹) at a height of 2 m, e_s is the saturation vapor pressure (kPa), and e_a is actual vapor pressure (kPa). Measurements of the weather data were provided from the Pousadas station.

The $K_{c,adj}$ (taking into account water stress to get K_s) was obtained by dividing the estimated ET_a from STSEB with ET_0 (Eq. (18)), in accordance with Eq. (17) for days with satellite observations.

In the other approach, Nunes et al. (2016) assumed that the soil evaporation can be neglected for summer, when the upper soil layer is dry. Following other researchers, they suggested a method to obtain K_{cb} from the Normalized Difference Vegetation Index (NDVI) for unstressed conditions at eucalypt stands. Their empirical method was developed from unburnt eucalypt stands in the same region as our study. Knowing that NDVI does not significantly vary for higher canopy cover (Häusler et al., 2016; Gamon et al., 1995) over short periods of time, we slightly modified the equation and applied as follows:

$$K_{cb} = a \times (NDVI - NDVI_s) \quad (19)$$

where a is an empirical scaling coefficient ($a = 2.74$), the NDVI is the last recorded NDVI from satellite data, and $NDVI_s$ represents the NDVI for bare soil pixels, where no vegetation transpiration is assumed. The procedure to obtain NDVI and $NDVI_s$ is explained by Häusler et al. (2018a,b). By dividing the value obtained from $K_{cb} \times ET_0$ (the so-called crop evapotranspiration) with K_{cb} (Eq. (19)), we get an estimation of K_s .

For the days where satellite data were unavailable, K_{cb} and $K_{c,adj}$ values of the previous day were used to estimate ET_a , by employing the day's ET_0 . This procedure continues until a cloud-free observation day allows again to retrieve, pixel-by-pixel, new values of K_{cb} and $K_{c,adj}$ from the respective method. The value for ET_a is obtained by multiplying ET_0 with K_{cb} and $K_{c,adj}$ from each pixel. Then, estimated ET_a enters the equations of the drought indices. In summary, a combined K_{cb} and $K_{c,adj}$ approach allows to bridge the gaps (here greatest gap was about two weeks) between two satellite observations and provides pixel-wise information of ET_a .

2.7. A threshold for fire-prone areas

We hypothesized that areas that are drier than others will remain drier over time, and therefore become more susceptible to fire, as the ignition and propagation are favored by drought and certain weather conditions.

The values of the KBDI and DC represent the absolute soil water content and determine the time of increased fire danger. Their values are also grouped into stages (e.g. KBDI stages from 0 to 7) expressing the current drought condition. Here, it was not our goal to question this subdivision, but to introduce a threshold to identify areas that might be drier and therefore more fire-prone than others already at the beginning of the season. A division into fire-prone to fire-safe areas might be helpful for fire management to ensure a good distribution of resources and initiate fire-preventing activities.

Due to the use of satellite images the spatial resolution of the drought factors was increased showing small variations between neighboring pixels. Normally, the ranges of the pixel values are very small at the beginning of the season and increase with time. These ranges of the drought factors are regularly too small to draw any further conclusions, but with the introduction of a threshold, areas with values smaller than the threshold itself were classified as less prone to fire and vice-versa.

To find a threshold that delimits fire-prone areas from areas with less fire danger a segmented histogram approach (Raju and Neelima, 2012) was applied. Hereby, an initial threshold S_i (here mid-range value) was selected, segmenting the image into two classes. Group 1 included all pixels defined as fire-prone $> S_i$ and group 2 incorporated the ones classified as fire-safe $\leq S_i$. Then, the average values of group 1 and 2 were computed and a new threshold found by:

$$S_i = \frac{\text{Avg. 1} + \text{Avg. 2}}{2} \quad (20)$$

The new threshold from Eq. (20) was applied and the procedure iterated till the difference of S_i was insignificantly small (e.g. variation smaller than 0.1 for the fire danger index). This procedure is called basic global thresholding and results in a histogram that partitions the image into two classes.

As the spatial range of SMD is different for each day (e.g. smaller after heavy rains, when soils are saturated and larger, when the soils become drier), the threshold must be independent of the data range. In this study, five days of the 46 days with satellite observation were randomly chosen to obtain a threshold to identify areas that are more fire-prone than others. Five days were sufficient to find a threshold as the histogram-based image segmentation varied only little between the images. The histogram-based image segmentation identified the threshold at which (a) the smallest total area assigned as fire-prone coincided with (b) most of the fire scars of 2015. In the case of the eucalypt stands in the central-north of Portugal the threshold was set to 60.6%.

Example: To identify the area as still fire-prone, the value for the threshold of 60.6% of the total data range must be obtained and subtracted from the upper limit of the total data range (e.g. 3 July 2015: absolute differences of data range for KBDI is 10.5, 60.6% is 6.3, maximum value of 185.5 minus 6.3 gives the lower limit of 179.2). Matrices were produced and overlaid with the fire scars of 2015 to identify the relationship of SMD to fire occurrences.

3. Results

3.1. Application of ET_a from STSEB

Evapotranspiration is assumed to be the only loss term of the simplified water balance model from KBDI and DC, leading to a reduction of soil moisture content and consequently to an increase of fire danger.

As no direct measurements of evapotranspiration were available,

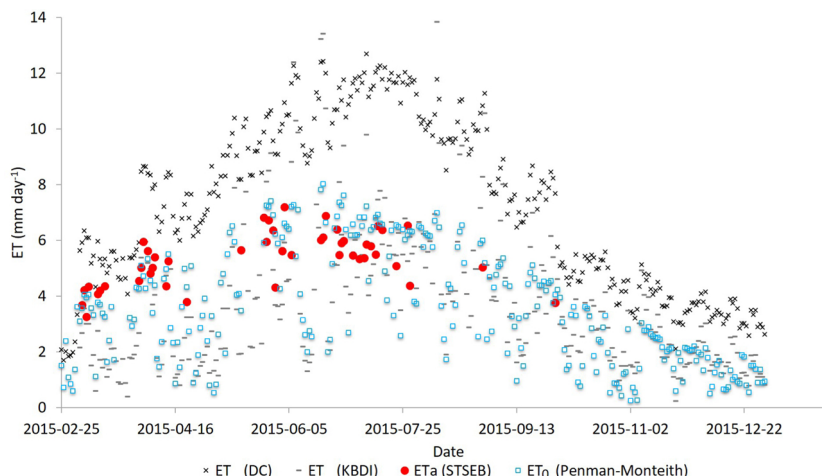


Fig. 2. The graph compares ET from the drought indices to the ET_0 from the reference method (Penman-Monteith) and the ET_a from STSEB, where all estimates are given in mm d^{-1} .

the ET from KBDI and DC were compared to the reference method from FAO Penman-Monteith and the estimates of ET_a from STSEB (Fig. 2). Regularly, the estimates of ET_a from the two-layer model were lower than the ET_0 from FAO Penman-Monteith (Eq. (18)). At the beginning of the season, ET_a from STSEB was slightly higher than ET_0 , which is probable true for eucalypt plantations, as the trees have a high water demand and did not suffer from stress after heavy rains in March, 2015 ($> 500 \text{ mm}$). Later, ET_a from STSEB becomes smaller than the reference method, which was expected due to limitations of water resources during the drier season of the year. Thus, ET_a from STSEB fits the estimates of ET_0 from FAO Penman Monteith method well. Assuming these values are representative, the ET from KBDI and DC were mostly under- and overestimated, respectively. Generally, the ET from DC showed less scatter than ET from KBDI and the reference method, and reached values up to 13 mm d^{-1} . The ET from KBDI showed a wide range of values for ET , especially during the drier months of the year (June to August), reaching from 1 mm d^{-1} to 14 mm d^{-1} .

3.2. Crop coefficients

Results showed that the K_{cb} hardly changed during the cycle with an average value of 1.20. From the beginning until the end of May, the K_{cb} was mostly below the average value (minimum of 1.03) and for the remaining observation period above the average (maximum of 1.37).

This was different for the $K_{c,adj}$, which had an average value of 1.14. At the beginning of the cycle, it went up to a value of 1.51 and

continuously decreased till the end of June with a value of 0.78 (Fig. 3). Subsequently, both coefficients were applied.

In Fig. 4, a comparison between measured SMD close to Pousadas station and estimated SMD from KBDI and DC is given, where the drought indices was retrieved from (i) the original empirical equations and also by (ii) using ET_a from STSEB (for days with satellite observations) combined with the crop coefficient approaches (no satellite observations).

The original DC version was the most responsive one to drying effects, reaching its limit by mid-July, which indicated very high fire danger. The DC, obtained from STSEB ET_a and the coefficients, was lower than the original one from the beginning of the cycle until May, when there was heavy precipitation. Up to this point the DC, using $K_{c,adj}$ steadily diverged from the original version, but less than the DC obtained from K_{cb} . The latter rose approximately only one third compared to the original DC until the first week of May, and decreased when rain was falling.

There was a clear difference between the K_{cb} and the $K_{c,adj}$ approach. After heavy rains, the DC from K_{cb} and $K_{c,adj}$ progressively estimated less SMD compared to the original DC. The DC from $K_{c,adj}$ reached the upper limit (very high fire danger) on the 10 of August. This was almost three weeks later than the original DC on the 23 of July. The DC from K_{cb} was less responsive and only estimated a maximum of SMD less than 70% until the next rainfalls in mid-September.

In the case of the original KBDI version, the drought code had a strong response to a rainfall event at the end of March, showing the

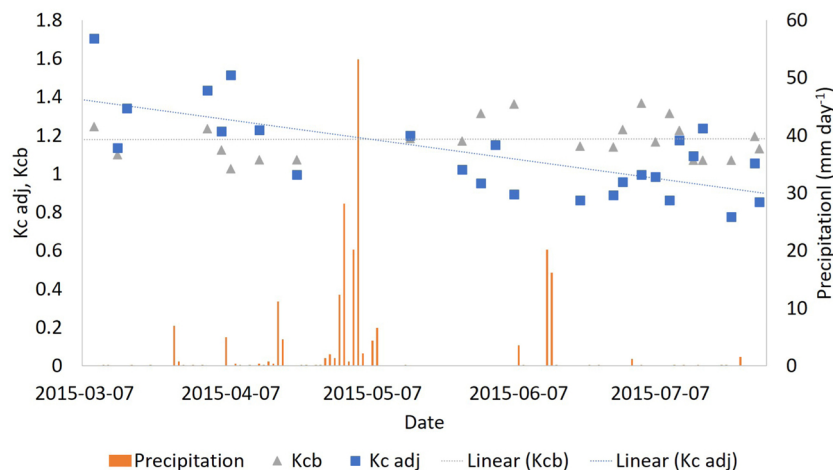


Fig. 3. Seasonal trend of basal crop coefficient (K_{cb}) and adjusted crop coefficient ($K_{c,adj}$), as they are obtained from Eq. (19) and Eq. (17).

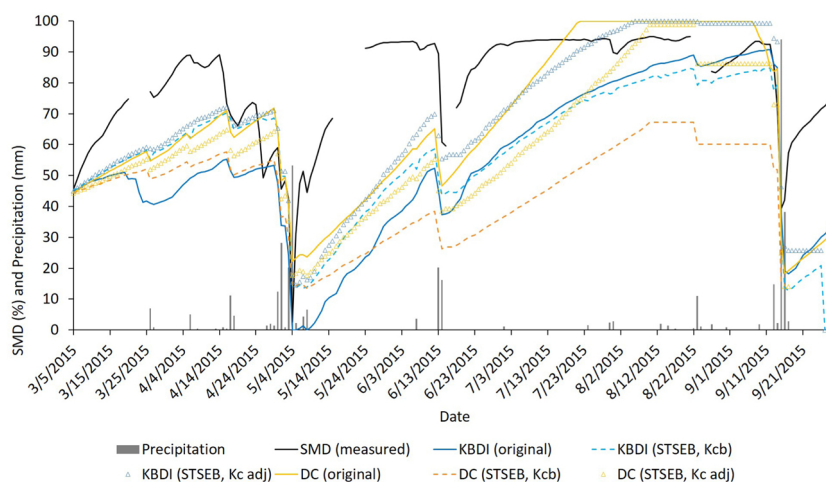


Fig. 4. Comparison of the soil moisture deficit (SMD) from on-site measurements at the Pousadas station, with the original Keetch-Byram Drought Index (KBDI) and Drought Code (DC), as well as from the combined Simplified Two-Source Energy Balance Model (STSEB) and crop coefficient approaches.

lowest value compared to the other drought code versions until the beginning of May. After the period of heavy precipitations in May, it subsequently increased and peaked at about 90% of SMD on the 11 of September. In the case of the KBDI from crop coefficients, both mimicked the progress of the original DC until May.

Then, the KBDI from $K_{c,adj}$ basically followed the original version of DC and was partly even higher and thereby closer to the measured SMD, while the K_{cb} approach slowly decreased over time and converged to the curve of the original KBDI. On the 5 of August, the KBDI from $K_{c,adj}$ reached the upper limit, that defined the point where no more soil water was available for the vegetation to be extracted. The estimated KBDI from the K_{cb} approach peaked at about 84% of SMD on the 13 of September.

In general, the original DC and the KBDI from $K_{c,adj}$ yielded similar results, indicating fire danger earlier (about end of July) than the other versions. The less responsive one was the DC from the K_{cb} approach.

3.3. A threshold for fire-prone areas

The use of MODIS satellite imagery allows to estimate SMD with a pixel size of 500 m. This makes it possible to determine the degree of dryness per pixel and identify areas that might dry out earlier than others. Small differences in SMD were detected early in the season and increased with time (e.g. drier area in March detected, one month before the actual fire occurred; first column of Fig. 5a and b). These dry areas overlay with the fire scars of the 2015 spring fires, although the absolute numbers of drought indices were still low, indicating no fire hazard.

Identifying differences per pixel also allowed to observe SMD changes after fires. The main fire we used for this study (on 2 April 2015) was identified on the drought index images produced from ET_a of the STSEB model and combined with the $K_{c,adj}$ approach (Fig. 5a and b). The values for KBDI and DC (representing SMD) increased after fire, when ET_a also increased.

Fig. 6 shows sub-figures with an area of 6400 km², with the Pousadas station located at the center point of each image. The images include masks of all the fires that occurred within the image margins in 2015. The total area burnt was about 1% of the total area shown in the figures.

When applying the threshold method (Section 2.7) to KBDI and DC, classifying the image into fire-prone and fire-safe areas, about 56.7% of the 2015 fire scars intersected with the classified fire-prone areas in both cases already on 9 March 2015 (Table 4). Generally, the drier the area becomes, the better the threshold works, being more precise in matching fire-prone areas with the fire scars. To give further examples:

on 8 July, 63.9% for KBDI and 45.7% for DC intersect with the areas classified as fire-prone. On 27 July, this is 74.5% and 52.2% for the classified fire-prone areas of KBDI and DC, respectively. Fig. 5c and Fig. 6c show the NDVI and ET_a of the different scenes for comparison.

4. Discussion

4.1. Application of ET_a from STSEB

By merely comparing the empirical equations for ET from drought indices with the reference method (FAO Penman-Monteith), the ET from KBDI and DC were under- and overestimated, respectively. The ET from both indices was far from reality during summer time, suggesting more than 13 mm d⁻¹, which was about the double value of ET_0 . The ET from KBDI was generally lower than to the reference method and showed great variability. Few values were even higher than ET from DC that was related to very high temperatures (> 30 °C). According to Keetch and Byram (1968), the relationship between T_{max} and ET_0 is exponential (numerator). By dividing the numerator by the denominator obtained from a fixed value of MAR , this results in an exponential raise.

Generally, by replacing the empirical equations for evapotranspiration with the remote sensing-based ET_a from STSEB and the crop coefficients, information on the progressive change in soil moisture content was retrieved on a pixel-by-pixel scale (Fig. 5a, b and Fig. 6a, b). Even though many studies adapted drought indices for SMD estimations, these enhancements were regularly limited to point observations and did not yield detailed spatial information.

4.2. Crop coefficients

The K_{cb} approach is simple and only needs the NDVI to continuously monitor transpiration (assuming $K_e = 0$) from satellite with a spatial resolution of 500 m. According to Anderson et al. (2012) the NDVI changes in a slow response to soil moisture, because long-term stress causes changes in vegetation indices (Ferreira, 2017). Over short periods of time, especially at high canopy cover (leaf area index > 4), K_{cb} and NDVI do not change significantly (Häusler et al., 2016; Gamon et al., 1995). Therefore, we assumed that K_{cb} values can be applied for several consecutive days without satellite observations. The value of K_{cb} showed little variation along the period under analysis (March to early August). Values higher than one indicate that there might have been evaporation for the time of observation. In May, after heavy rains, the K_{cb} slightly increased, on average, reflecting the growth of tree leaves and therefore more transpiration.

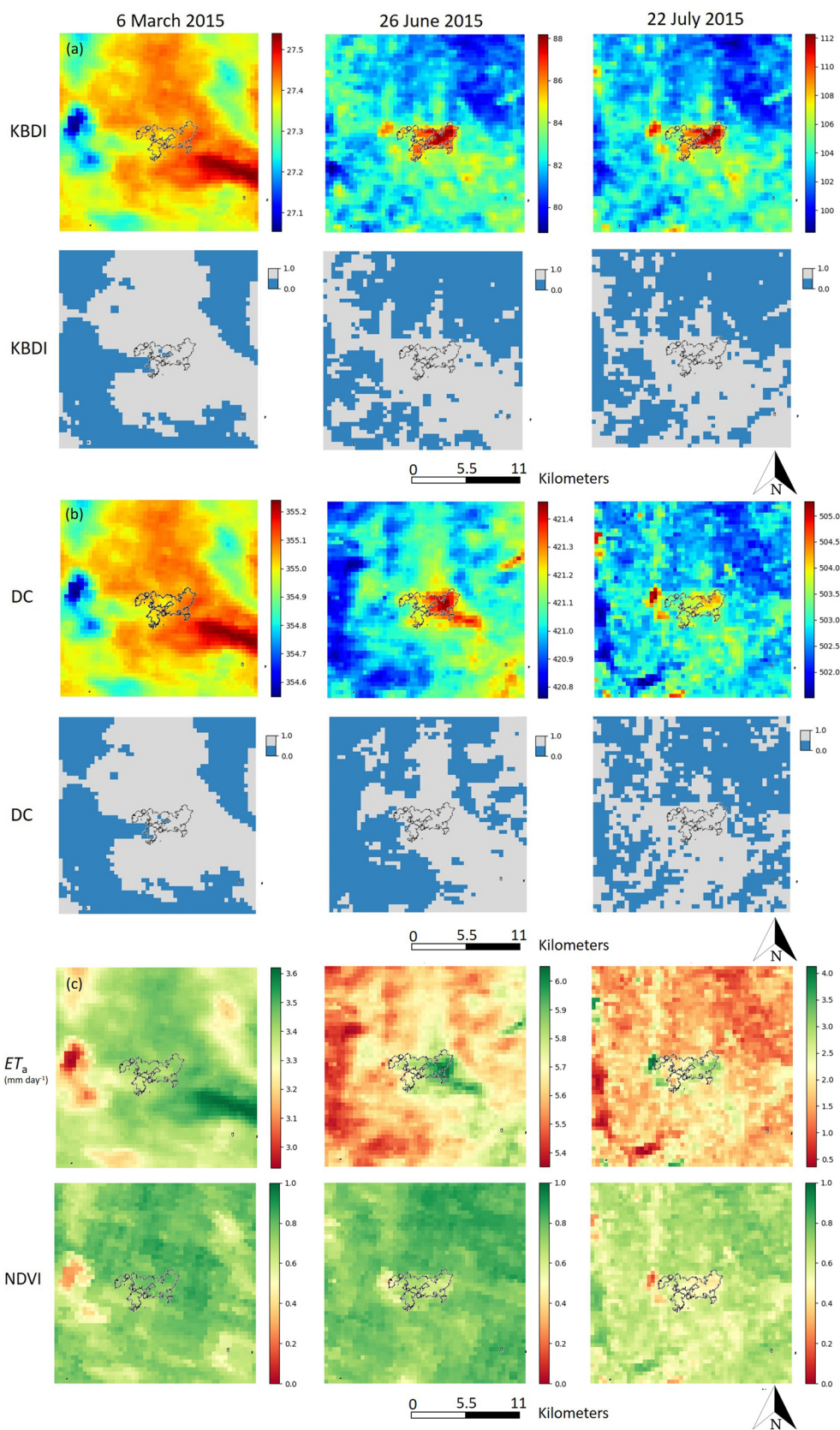


Fig. 5. Image (a) shows Keetch-Byram Drought Index (KBDI) and (b) Drought Code (DC) of the wildfire in 2015, retrieved from the actual evapotranspiration (ET_a) of the Simplified Two-Source Energy Balance model (STSEB) and the adjusted crop coefficient ($K_{c,adj}$) for cloudy days. The first row shows the drought index with its actual values, the second row the classification into fire-prone (grey) and fire-safe (blue) areas. Fig. (c) shows the estimated daily ET_a in the first row and the NDVI in the second row. The columns are the days, 6 March (about one month before the fire), 26 June (about two months after the fire), and 22 July 2015, respectively. (For interpretation of the references to color in this figure legend, the reader is referred to the web version of this article.)

Since, no direct measurements for transpiration at the eucalypt stand has been available, we assume a reduction of water consumption starting in July. David et al. (1997) showed a continuous decrease of daily transpiration in a mature eucalypt stand in Portugal, during a

drying period, using the Granier method (Granier, 1985) for sap flow measurements. This is not indicated by the values of K_{cb} , being still above 1 by the end of July.

The $K_{c,adj}$ (Eq. 5.19) includes three effects: crop transpiration, soil

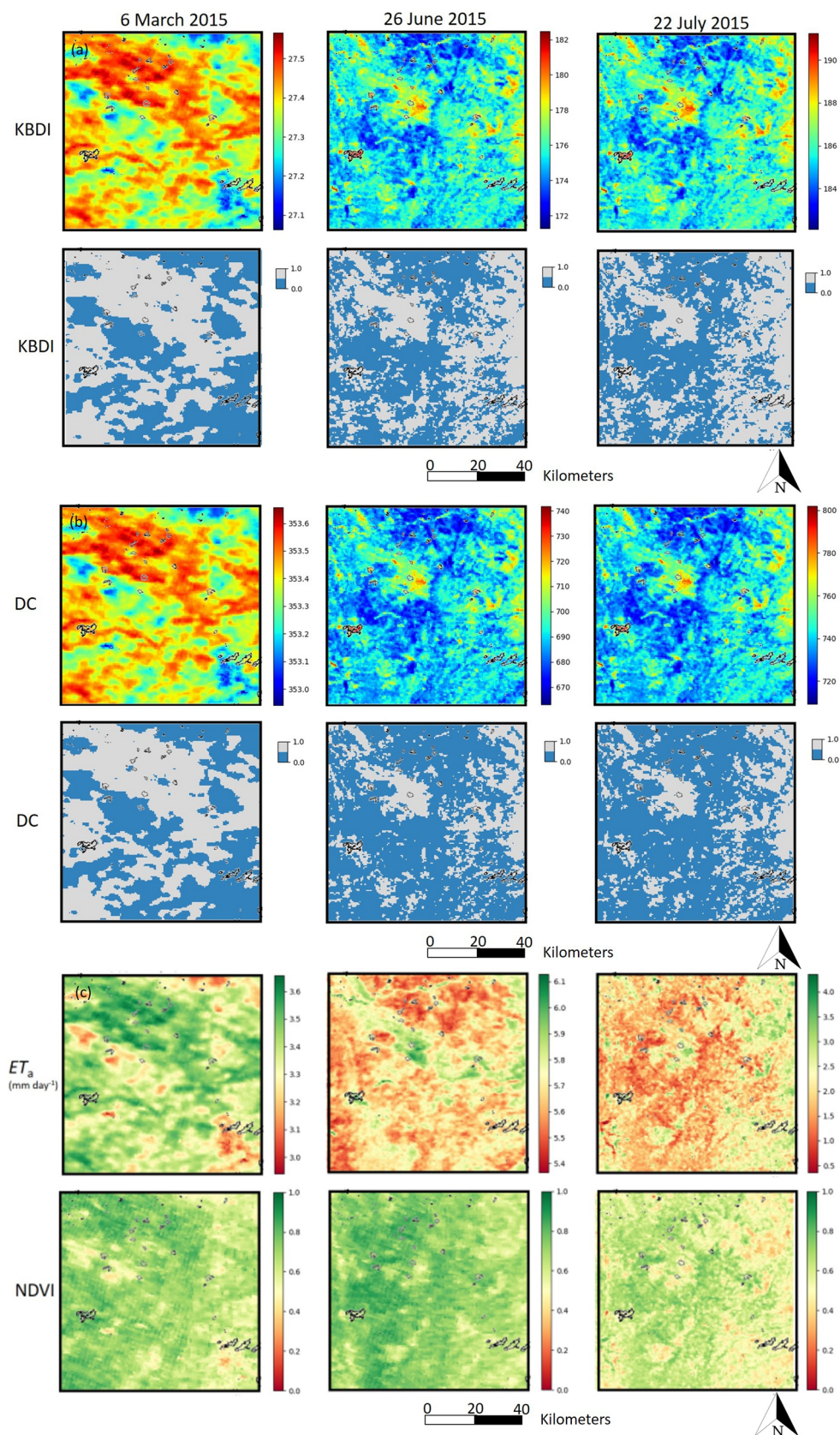


Fig. 6. The figures demonstrate an area of about 6400 km² around Pousadas station (centre point) with indicated fire margins of 2015. Image (a) shows the Keetch-Byram Drought Index (KBDI) and (b) the Drought Code (DC) retrieved by using actual evapotranspiration (ET_a) from the Simplified Two-Source Energy Balance model (STSEB) and the adjusted crop coefficient ($K_{c,adj}$). The first row shows the drought index with the actual values and the second row the classification into fire-prone (grey) and fire-save (blue) areas. Image (c) demonstrates the estimated daily ET_a from STSEB in the first row followed by the NDVI in the second row. The columns are the days, 6 March, 26 June, and 22 July 2015, respectively. (For interpretation of the references to color in this figure legend, the reader is referred to the web version of this article.)

evaporation, and the water stress. At the beginning of the cycle, the values for $K_{c,adj}$ were high, on average, indicating that there was no water stress ($K_s = 1$) and there was evaporation from the soil ($K_e > 0$). As time progresses, the upper soil layers dry out and the evaporation

component goes to zero (see values around end of May). After heavy precipitation, at the beginning of May, $K_{c,adj}$ shortly increased, and then decreased continuously. With decreasing soil water content, it is more difficult for the trees to extract water and they experience water stress,

Table 4

For the year 2015 some examples are given in percentage, listing the areas which were classified as fire-prone (i.e. Fire-prone, classified) and then later also affected by fire (i.e. Fire-affected, intersected). The threshold has been set to 60.6%, which represented the lowest value of a particular data range and day when areas were still classified as susceptible to fire.

Date	KBDI		DC	
	Fire-prone classified (%)	Fire-affected intersected (%)	Fire-prone classified (%)	Fire-affected intersected (%)
9 March 2015	52.2	56.7	51.8	56.7
7 April 2015	47.6	55.3	41.0	50.2
29 Mai 2015	35.4	47.1	29.9	41.9
2 June 2015	38.8	51.9	31.1	46.4
26 June 2015	43.4	57.4	29.1	44.7
8 July 2015	45.5	63.9	28.1	45.7
16 July 2015	47.0	66.7	29.3	47.4
27 July 2015	56.6	74.5	34.5	52.2

when the water reservoir in soil decreases to a certain threshold (lower end of RAW, Eq. (22)). However, the $K_{c,adj}$ reached only a lower limit of 0.8 by the end of the observation period, which indicated only the beginning of stress conditions. Even though the bedrock is sometimes considered relatively impermeable (Nunes et al., 2016), the trees seem to have found an efficient strategy to find access to water. In the literature, there is only little reported about K_{cb} in forest stands, as they are regularly not a subject to irrigation management. Alves et al. (2013) reported values for the dual crop coefficient K_c (including only $K_{cb} + K_c$) for newly planted eucalypt stands (up to two years old) under irrigation management in Brazil. The K_c ranged from the initial growth state to the mid-season state from 0.6 to 0.8, respectively, which is, as expected, lower than the values found in this study.

4.3. A threshold for fire-prone areas

Fire danger increases with decreasing water holding capacity of soils and the dryness of the upper layer of the soil (Snyder et al., 2006; Kumar and Dharssi, 2017). Several authors showed an existing correlation between soil moisture state and fuel moisture content (Burgan, 1988; Viegas et al., 1999). Thus, methods to estimate the SMD were developed to approximate the fuel moisture content and rate the current state of fire danger.

By the incorporation of ET_a from STSEB, the drought indices estimated small spatial differences of SMD over larger areas with a pixel size of 500 m (see Figs. 5a,b and 6a,b, first row) already early in the season. These differences allowed to distinguish areas that are drier than others and therefore are more prone to fire. With the so-called basic global thresholding a histogram was obtained to partition the image into two classes and prioritize areas for fire protection activities (Figs. 5a,b and 6a,b, second row). The occurrence of wildfires at eucalypt stands could be shown to be related to the dried out areas.

Small fluctuations or even the differentiation of different soil moisture levels can neither be determined by interpolation techniques (see: Portugal), nor by fire danger products that regularly do not exceed spatial resolutions of several kilometers (e.g. LSA-SAF, fire risk product including DC with $3 \text{ km} \times 3 \text{ km}$ spatial resolution, Trigo et al., 2011).

Even though the threshold worked well in our case, an evaluation based on fire occurrences might be biased, as the cause of the fires where mainly unknown (> 70%). This means fire might have been started, where the soil moisture conditions were not favorable e.g. “cleaning” of agricultural areas, but was included for the evaluation of the threshold. Furthermore, the KBDI and DC are only a measure of soil moisture and a proxy of fuel moisture content, which are not the only driving factors for fire danger. Other factors such as fire ignition and propagation (e.g. favorable weather conditions) (Chuvieco et al., 2004)

with the influence of human interactions, make the relationship rather complex (Bisquert et al., 2011). For future work, this should be further considered to improve the threshold.

5. Conclusion

To date, fire danger rating is based on interpolation techniques between meteorological stations that give only little information about the local conditions of fire danger (Aguado et al., 2003). Our study aimed to combine traditional methods (e.g. two-source energy balance models) with remote sensing, to enhance SMD estimations in terms of its daily, spatial resolution. The use of MODIS products allowed a simplified and fast adaption of the STSEB model (Sánchez et al., 2008), which is rather complex compared to the empirical equations of KBDI and DC. Drought indices related to SMD were tested in terms of SMD prediction and spatial resolution. By the use of satellite imagery the SMD was estimated over larger areas and we hypothesized that areas that are dryer than their surrounding areas are more susceptible to fire. For the case of Portugal it showed that the occurrence of wildfires at eucalyptus stands was related to SMD, and with the use of a threshold, regions were classified into prone and less prone to fires. For days without satellite observations, two difference crop coefficient approaches were suggested to be able to continue SMD estimations. The results showed that:

- the estimated ET_a from STSEB enhance the spatial resolution (500 m) of both indices compared to traditional interpolation techniques,
- the crop coefficient approaches allowed the continuous estimation of drought indexes for cloudy days without satellite observations at the pixel level,
- it showed that the DC is more sensitive to changes in ET_a than the KBDI,
- and to estimate ET_a , $K_{c,adj}$ should be preferred to K_{cb} as the value of K_{cb} only obtains ET_a , when K_e is zero, and K_s is one.

Our study allowed to obtain spatial information of soil moisture variations on a pixel level of 500 m. These variations were, especially at the beginning of the season very small, but persisted as the year progressed. It showed that a relationship between areas that dried out earlier and burnt areas existed. This is valuable information can help to adapt forest and fire management by identifying areas with less soil moisture holding capacity, where dense vegetation should be avoided and where fire fighting measures should be prioritized.

To sum up, traditional fire danger rating is useful, but must be improved by the state of the technology to reduce wildfire events and ensure people's safety. Different problems need different solutions. With our contribution, we show a new aspect to fire danger rating in terms of spatial resolution and variation of SMD. In a future work, we will focus on creating a map of Portugal, pointing out potential “hot spots” and extend the application to other regions (Table 5).

Funding

This study was financially supported by the R&D project [grant number UID/AGR/00239/2013] within the research activities of the Forest Research Centre, at the School of Agriculture, University of Lisbon. M. Häusler, João M.N. Silva, J.J. Keizer, and J.P. Nunes were funded by the Foundation for Science and Technology [FCT, Portugal; grant numbers PD/BD/52698/2014, SFRH/BPD/109535/2015, IF/01465/2015, and IF/00586/2015, respectively]; co-funded by the European Social Fund within the Operational Program Human Potential.

Table 5
Acronyms and variables used in this article.

Abbreviation	Definition
CFFWI	Canadian Forest Fire Weather Index
DC	Drought Code
FC	Field Capacity
KBDI	Keetch-Byram Drought Index
MODIS	MODerate-resolution Imaging Spectroradiometer
PWP	Permanent Wilting Point
SMOS	Soil Moisture Ocean Salinity product
SMD	Soil Moisture Deficit
STSEB	Simplified Two-Source Energy Balance model
γ	Psychrometric constant, kPa, °C
Δ	Slope of the vapour pressure curve, kPa, °C
δQ	Change of soil water content during a certain time of δt
θ_{FC}	Water content at field capacity, $m^3 m^{-3}$
θ_{WP}	Water content at wilting point, $m^3 m^{-3}$
ρ	Air density, $kg m^{-3}$
C_p	Air specific heat at constant pressure, $kJ kg^{-1} K^{-1}$
DP	Deep percolation, $mm day^{-1}$
e_a	Actual vapour pressure, kPa
e_s	Saturation vapour pressure, kPa
ET_a	Actual evapotranspiration for individual crops, $mm day^{-1}$
ET_c	Crop evapotranspiration under standard conditions, $mm day^{-1}$
ET_0	Daily reference evapotranspiration, $mm day^{-1}$
ET_p	Daily potential evapotranspiration, $mm day^{-1}$
H	Sensible heat flux density, $W m^{-2}$
G_d	Daily soil heat flux density, $W m^{-2} day^{-1}$
G	Soil heat flux density, $W m^{-2}$
K_c	Dual crop coefficient, adim.
$K_{c,adj}$	Adjusted crop coefficient, adim.
K_{cb}	Basal crop coefficient, adim.
K_e	Soil evaporation coefficient, adim.
K_s	Water stress coefficient, adim.
LE	Latent heat flux density, $W m^{-2}$
L_f	Seasonal correction factor for day length, adim.
MAR	Mean annual rainfall, $mm y^{-1}$
$NDVI$	Normalized Difference Vegetation Index, adim.
$NDVI_s$	Normalized Difference Vegetation Index of the soil, adim.
pF-curve	The relation between soil moisture suction and soil moisture content, pF
P_{daily}	Actual measured rainfall in the open of one day (24 h)
P_{eff}	Effective rainfall that is the actual water reaching and infiltrating the soil depths without interception, $mm day^{-1}$
S_i	Initial threshold, separating a value range into two classes
R_n	Net radiation, $W m^{-2}$
RO	Runoff, $mm day^{-1}$
RP	Moisture equivalent after rain, % of dry soil
TAW	Total available soil water in the root zone, mm
T_{max}	Maximum daily air temperature, °C, or K
T_{mean}	Mean daily air temperature, °C, or K
T_{min}	Minimum daily air temperature, °C, or K
T_v	Temperature of the vegetation, K
T_s	Temperature of the soil, K
u_2	Wind speed at 2 m height, $m s^{-1}$

Conflicts of interest

The authors declare no conflict of interest.

Appendix

For drought indices, a negative exponential relationship for the reduction of the soil water content caused by evapotranspiration over time is assumed. The time to deplete the water reservoir, if the evapotranspiration proceeded at the “max. potential rate” (Van Wagner, 1985), was called the evapotranspiration time-lag (t , Fig. 8), being the most important measure of a drought index (Keetch and Byram, 1968; Van Wagner, 1985). By linking the aforementioned assumptions to expressions used in water use and irrigation management, the total available water is:

$$TAW = 1000(\theta_{FC} - \theta_{WP})Z_r \quad (21)$$

where 1000 is a scaling factor, θ_{FC} is the water content at FC ($m^3 m^{-3}$), θ_{WP} is the water content at PWP ($m^3 m^{-3}$), and Z_r is the soil depth (m).

The water, which is available without reduction in ET_a , is called “readily available water” (RAW) and is determined as follows:

$$RAW = p \times TAW \quad (22)$$

where p is the average fraction of TAW (Eq. (21)) and often assumed to be a value between 0.6 and 0.8 (Allen et al., 1998), but according to recent

Acknowledgments

The authors are grateful to all the scientists, engineers, and students who contributed to this project, especially to Dr. Paula Soares, Dr. Francisco Goes (CELPA, Associação da Indústria Papeleira), Tomás Calheiros, and Martinho Martins, and for the provision of data, concerning stand properties and meteorological data. Special thanks goes to Dr. Alberto Garcia Prats, who provided the code to retrieve the KBDI and Dr. Andreas Häusler, who helped with the implementation of KBDI and DC to the existing STSEB code. We are also grateful to Prof. Isabel Ferreira for the fruitful discussions and her explanation of concepts, concerning water use and irrigation management. The surface reflectance and brightness temperature data were provided by the U.S. Geological Survey Earth Resources Observation and Science (EROS) Data Centre.

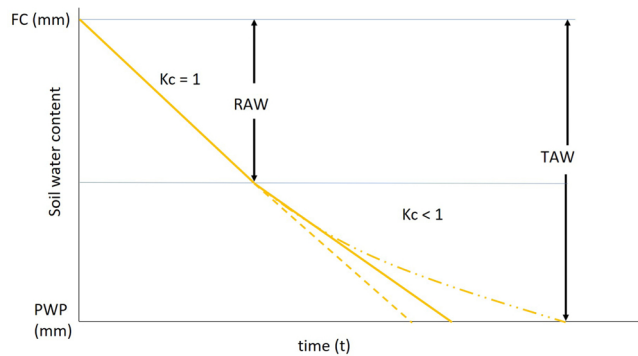


Fig. 7. Scheme of soil water depletion over time, where FC is the field capacity, PWP the permanent wilting point, RAW the readily available water and TAW the total available water content of the soil.

studies (Ferreira, 2017), this parameter can be as low as 0.5 for some Mediterranean species.

In water use science, it is assumed that ET_a is equal to ET_0 over grassland as long as there is no restriction to water, meaning that soil water content is above a threshold, which is the lower limit of RAW (Eq. (22)). When the soil water is below RAW, the vegetation starts to suffer from water stress. The effects of soil water depletion depend on the vegetation as described by Ferreira (2017), and a general scheme how soil water is depleted is demonstrated in Fig. 7.

This can be different for drought indices, as the process of water content reduction is expressed by a negative exponential relationship (Fig. 8a). Any factor that effects the evapotranspiration rate, e.g. T_a , day length, will also have an effect on the time-lag. Keetch and Byram (1968) further limited the evapotranspiration rate by including the mean annual rainfall (MAR). They claim that the vegetation density is a function of MAR and consequently of the vegetation capacity to transpire water, when the weather variables are constant. These authors claim that the vegetation-rainfall relationship is described by an exponential curve, where the rate of moisture removal increases with increasing vegetation density, and because of that, with increasing MAR (Fig. 8b).

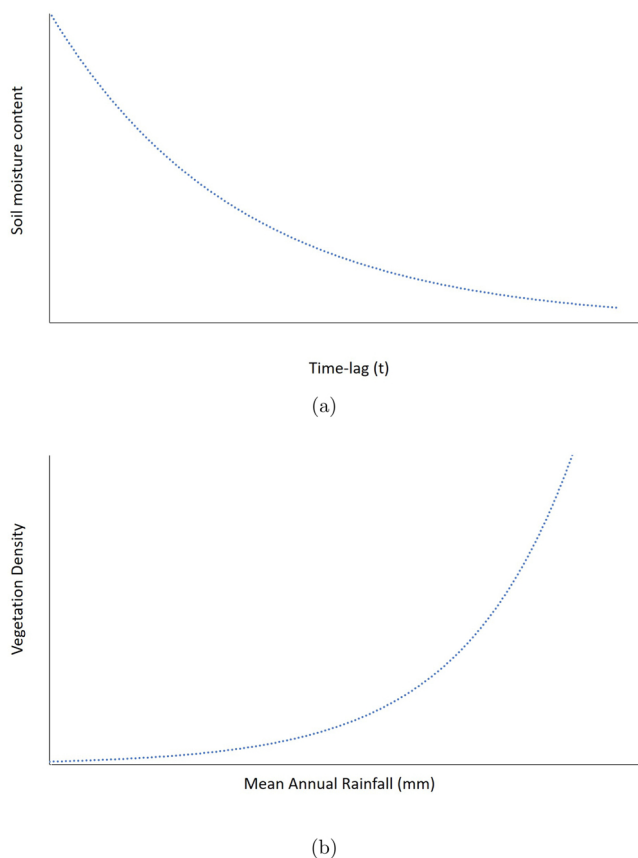


Fig. 8. The water content reduction by evapotranspiration over time (also called evapotranspiration time-lag t) is given by (a), and the relationship between vegetation density and mean annual rainfall (MAR) by (b).

References

- Aguado, I., Chuvieco, E., Martín, P., Salas, J., 2003. Assessment of forest fire danger conditions in southern Spain from NOAA images and meteorological indices. *Int. J. Remote Sens.* 24, 1653–1668.
- Allen, R.G., Pereira, L.S., Raes, D., Smith, M., 1998. FAO Irrigation and Drainage Paper No. 56, Crop Evapotranspiration (guidelines for computing crop water requirements). *Geophysics* 156, 1–178.
- Alves, M.E.B., Mantovani, E.C., Sedyama, G.C., Neves, J.C.L., 2013. Estimate of the crop coefficient for Eucalyptus cultivated under irrigation during initial growth. *Cerne* 19, 247–253.
- Anderson, M.C., Allen, R.G., Morse, A., Kustas, W.P., 2012. Use of Landsat thermal imagery in monitoring evapotranspiration and managing water resources. *Remote Sens. Environ.* 122, 50–65.
- Belda, M., Holtanová, E., Halenka, T., Kalvová, J., 2014. Climate classification revisited: from Köppen to Trewartha. *Clim. Res.* 59, 1–13.
- Bisquert, M.M., Sánchez, J.M., Caselles, V., 2011. Fire danger estimation from MODIS Enhanced Vegetation Index data: application to Galicia region (north-west Spain). *Int. J. Wildland Fire* 20, 465–473.
- Boulet, A.K., Prats, S.A., Malvar, M.C., González-Pelayo, O., Coelho, C.O., Ferreira, A.J., Keizer, J.J., 2015. Surface and subsurface flow in eucalyptus plantations in north-central Portugal. *J. Hydrol. Hydromech.* 63, 193–200.
- Burgan, R.E., 1988. 1988 Revisions to the 1978 National Fire-Danger Rating System, Technical Report. U.S. Department of Agriculture, Ashville.
- Carlson, J.D., Burgan, R.E., 2003. Review of users' needs in operational fire danger estimation: the Oklahoma example. *Int. J. Remote Sens.* 24, 1601–1620.
- Chuvieco, E., Aguado, I., Dimitrakopoulos, A.P., 2004. Conversion of fuel moisture content values to ignition potential for integrated fire danger assessment. *Can. J. For. Res.* 34, 2284–2293.
- Conceição, N., Tezza, L., Häusler, M., Lourenço, S., Pacheco, C.A., Ferreira, M.I., 2017. Three years of monitoring evapotranspiration components and crop and stress coefficients in a deficit irrigated intensive olive orchard. *Agric. Water Manage.* 191, 138–152.
- DaCamara, C., Calado, T., Nunes, S., Rosa, T., 2015. Product User Manual for Fire Risk Map (FRM). Technical Report 2.0. The EUMETSAT Network of Satellite Application Facilities. Land Surface Analysis. SAF.
- David, T.S., Ferreira, M.I., David, J.S., Pereira, J.S., 1997. Transpiration from a mature *Eucalyptus globulus* plantation in Portugal during a spring-summer period of progressively higher water deficit. *Oecologia* 110, 153–159.
- Doorenbos, J., Kassam, A.H., 1979. FAO Irrigation and Drainage Paper No. 33. In: Smith, M., Steduto, P. (Eds.), *Yield Response to Water: The Original FAO Water Production Function*. Rome, Italy, pp. 193.
- Ferreira, M.I., 2017. Stress coefficients for soil water balance combined with water stress indicators for irrigation scheduling of woody crops. *Horticulturae* 3, 38.
- Ferreira, M.I., Valancogne, C., Daudet, F.A., Ameglio, T., Pacheco, C.A., Michaelsen, J., 1996. Evapotranspiration and crop-water relations in a peach orchard. In: *Proceed. of Int. Conf. on Evapotranspiration and Irrigation Scheduling*. San Antonio, TX. pp. 61–68.
- Gamon, J.A., Field, C.B., Goulden, M.L., Griffin, K.L., Hartley, A.E., Joel, G., Penuelas, J., Valentini, R., 1995. Relationships between NDVI, canopy structure, and photosynthesis in three Californian vegetation types. *Ecol. Appl.* 5, 28–41.
- Ganatsas, P., Antonis, M., Marianthi, T., 2011. Development of an adapted empirical drought index to the Mediterranean conditions for use in forestry. *Agric. For. Manage.* 151, 241–250.
- García-Prats, A., Antonio, D.C., Tarcísio, F.J., Antonio, M.J., 2015. Development of a Keetch and Byram-based drought index sensitive to forest management in Mediterranean conditions. *Agric. For. Manage.* 205, 40–50.
- Girardin, M.P., Tardif, J., Flannigan, M.D., Wotton, B.M., Bergeron, Y., 2004. Trends and periodicities in the Canadian Drought Code and their relationships with atmospheric circulation for the southern Canadian boreal forest. *Can. J. For. Res.* 34, 103–119.
- Granier, A., 1985. Une nouvelle méthode pour la mesure du flux de sève brute dans le tronc des arbres. *Ann. Sci. For.* 42, 193–200.
- Hargreaves, G.H., Samani, Z.A., 1985. Reference crop evapotranspiration from temperature. *Appl. Eng. Agric.* 1, 96–99.
- Häusler, M., Conceição, N., Tezza, L., Sánchez, J.M., Campagnolo, M.L., Häusler, A.J., Silva, J.M., Warneke, T., Heygster, G., Ferreira, M.I., 2018a. Estimation and partitioning of actual daily evapotranspiration at an intensive olive grove using the STSEB model based on remote sensing. *Agric. Water Manage.* 201, 188–198.
- Häusler, M., Nunes, J.P., Soares, P., Sánchez, J.M., Silva, J.M.N., Warneke, T., Keizer, J.J., Pereira, J.M.C., 2018b. Assessment of the indirect impact of wildfire (severity) on actual evapotranspiration in eucalyptus forest based on the surface energy balance estimated from remote-sensing techniques. *Int. J. Remote Sens.* 1–26.
- Häusler, M., Silva, J.M.N., Cerasoli, S., López-Saldaña, G., Pereira, J.M.C., 2016. Modelling spectral reflectance of open cork oak woodland: a simulation analysis of the effects of vegetation structure and background. *Int. J. Remote Sens.* 37, 492–515.
- Hengl, T., Heuvelink, G.B.M., Tadić, M.P., Pebesma, E.J., 2012. Spatio-temporal prediction of daily temperatures using time-series of MODIS LST images. *Theor. Appl. Climatol.* 107, 265–277.
- Holgate, C.M., van Dijk, A.I.J.M., Cary, G.J., Yebra, M., 2017. Using alternative soil moisture estimates in the McArthur Forest Fire Danger Index. *Int. J. Wildland Fire* 26, 806.
- Humes, K., Hardy, R., Kustas, W., Prueger, J., Starks, P., 2004. High spatial resolution mapping of surface energy balance components with remotely sensed data. *Therm. Rem. Sen. in Land Surf. Process*. CRC Press, New York, pp. 110–132 (chapter 3). ICNF, 2018. Instituto da Conservação da Natureza e das Florestas.
- Irmak, S., Haman, D.Z., 2003. Evapotranspiration: Potential or Reference? Technical Report. University of Florida, Gainesville, FL.
- Keetch, J.J., Byram, G.M., 1968. A Drought Index for Forest Fire Control. Technical Report. U.S. Department of Agriculture - Forest Service, Asheville, North Carolina.
- Kerr, Y.H., Waldeufel, P., Wigneron, J.P., Delwart, S., Cabot, F., Boutin, J., Escorihuela, M.J., Font, J., Reul, N., Gruhier, C., Juglea, S.E., Drinkwater, M.R., Hahne, A., Martín-Neira, M., Mecklenburg, S., 2010. The SMOS Mission: new tool for monitoring key elements of the global water cycle. *Proc. IEEE* 98, 666–687.
- Krueger, E.S., Ochsner, T.E., Engle, D.M., Carlson, J., Twidwell, D., Fuhlendorf, S.D., 2015. Soil moisture affects growing-season wildfire size in the Southern Great Plains. *Soil Sci. Soc. Am. J.* 79, 1567.
- Kumar, V., Dharsli, I., 2017. Evaluation of daily soil moisture deficit used in Australian forest fire danger rating system. Technical Report. Australian Government: Bureau of Meteorology.
- Kustas, W.P., Daughtry, C.S.T., 1990. Estimation of the soil heat flux/net radiation ratio from spectral data. *Agric. For. Meteorol.* 49, 205–223.
- Lazzara, P., Rana, G., 2010. The crop coefficient (Kc) values of the major crops grown under Mediterranean climate. *Ital. J. Agrometeorol.* 15, 25–40.
- Liu, H., Shi, J., Erdem, E., 2010. Prediction of wind speed time series using modified Taylor Kriging method. *Energy* 35, 4870–4879.
- McArthur, A.G., 1967. Fire behaviour in eucalypt forests. Department of National Development, Forestry and Timber Bureau, Canberra, Australia (leaflet no edition).
- Mukhopadhyaya, S., 2016. Rainfall mapping using ordinary Kriging technique: case study: Tunisia. *J. Basic Appl. Eng. Res.* 3, 1–5.
- Nunes, J.P., Bernard-Jannin, L., Rodríguez Blanco, M.L., Santos, J.M., Coelho, C.d.O.A., Keizer, J.J., 2018. Hydrological and erosion processes in terraced fields: observations from a humid Mediterranean region in northern Portugal. *Land Degrad. Dev.* 29, 596–606.
- Nunes, J.P., Malvar, M., Benali, A.A., Rial Rivas, M.E., Keizer, J.J., 2016. A simple water balance model adapted for soil water repellency: application on Portuguese burned and unburned eucalypt stands. *Hydrol. Processes* 30, 463–478.
- Paço, T.A., Pôças, I., Cunha, M., Silvestre, J.C., Santos, F.L., Paredes, P., Pereira, L.S., 2014. Evapotranspiration and crop coefficients for a super intensive olive orchard. An application of SIMDualKc and METRIC models using ground and satellite observations. *J. Hydrol.* 519, 2067–2080.
- Palma, J.H.N., 2013. Web-Globulus 3.0.
- Palmer, W.C., 1965. Meteorological Drought. Technical Report. U.S. Department of Commerce, Washington, D.C.
- Parente, J., Pereira, M., Amraoui, M., Fischer, E., 2018. Heat waves in Portugal: current regime, changes in future climate and impacts on extreme wildfires. *Sci. Total Environ.* 631–632, 534–549.
- Raju, P.D., Neelima, G., 2012. Image segmentation by using histogram thresholding. *IJCSET* 2, 776–779.
- Rehman, S., Ghorri, S.G., 2000. Spatial estimation of global solar radiation using geostatistics. *Renew. Energy* 21, 583–605.
- Sánchez, J., López-Urrea, R., Rubio, E., González-Piqueras, J., Caselles, V., 2014. Assessing crop coefficients of sunflower and canola using two-source energy balance and thermal radiometry. *Agric. Water Manage.* 137, 23–29.
- Sánchez, J.M., Kustas, W.P., Caselles, V., Anderson, M.C., 2008. Modelling surface energy fluxes over maize using a two-source patch model and radiometric soil and canopy temperature observations. *Remote Sens. Environ.* 112, 1130–1143.
- Santos, J.M., Verheijen, F.G.A., Tavares Wahren, F., Wahren, A., Feger, K.H., Bernard-Jannin, L., Rial-Rivas, M.E., Keizer, J.J., Nunes, J.P., 2016. Soil water repellency dynamics in pine and eucalypt plantations in Portugal – a high-resolution time series. *Land Degrad. Dev.* 27, 1334–1343.
- Seguin, B., Itier, B., 1983. Using midday surface temperature to estimate daily evaporation from satellite thermal IR data. *Int. J. Remote Sens.* 4, 371–383.
- Shakesby, R.A., Coelho, C.D.O.A., Ferreira, A.D., Terry, J.P., Walsh, R.P.D., 1993. Wildfire impacts on soil erosion and hydrology in wet Mediterranean forest, Portugal. *Int. J. Wildland Fire* 3, 95–110.
- Sharples, J., McRae, R., Weber, R., Gill, A., 2009. A simple index for assessing fuel moisture content. *Environ. Model. Software* 24, 637–646.
- Snyder, R.L., Spano, D., Duce, P., Baldocchi, D., Xu, L., Paw, U.K.T., 2006. A fuel dryness index for grassland fire-danger assessment. *Agric. For. Meteorol.* 139, 1–11.
- Testi, L., Villalobos, F., Orgaz, F., 2004. Evapotranspiration of a young irrigated olive orchard in southern Spain. *Agric. For. Manage.* 121, 1–18.
- Thornthwaite, C.W., 1948. An approach toward a rational classification of climate. *Geogr. Rev.* 38, 55–94.
- Thornthwaite, C.W., Mather, J.R., 1955. The water balance. *Publications in Climatology* 8, 1–104.
- Trigo, I.F., Dacamara, C.C., Viterbo, P., Roujean, J.L., Olesen, F., Barroso, C., Camacho-de Coca, F., Carrer, D., Freitas, S.C., García-Haro, J., Geiger, B., Gellens-Meulenberghs, F., Ghilain, N., Meliá, J., Pessanha, L., Siljamo, N., Arboleda, A., 2011. The satellite application facility for land surface analysis. *Int. J. Remote Sens.* 32, 2725–2744.
- Turner, J.A., 1966. The stored moisture index: a guide to slash burning. Technical Report. Brit. Columbia Forest Serv.
- Turner, J.A., 1972. The drought code component of the Canadian forest fire behavior system. Technical Report 1316. Canadian Forestry Service, Department of the Environment, Ottawa, USA.
- Valor, E., Caselles, V., 1996. Mapping land surface emissivity from NDVI. Application to European, African and South-American areas. *Remote Sens. Environ.* 57, 167–184.
- Van Wagner, C.E., 1974. Structure of the Canadian Forest Fire Weather Index. Technical Report. Department of the Environment, Ottawa, USA.
- Van Wagner, C.E., 1985. Drought, timelag, and fire danger rating. In: *Eighth Conference on Fire and Forest Meteorology*. Society of American Foresters, Detroit, Michigan. pp. 178–185.

- Van Wagner, C.E., 1987. Development and structure of the Canadian forest fire weather index system. Technical Report. Canadian Forestry Service, Ottawa, USA.
- Viegas, D.X., Bovio, G., Ferreira, A., Nosenzo, A., Sol, B., 1999. Comparative study of various methods of fire danger evaluation in southern Europe. *Int. J. Wildland Fire* 9, 235.
- Vinodkumar, Dharssi, I., Bally, J., Steinle, P., McJannet, D., Walker, J., 2017. Comparison of soil wetness from multiple models over Australia with observations. *Water Resour. Res.* 53, 633–646.
- Wahren, F.T., Julich, S., Nunes, J.P., Gonzalez-Pelayo, O., Hawtree, D., Feger, K.H., Keizer, J.J., 2016. Combining digital soil mapping and hydrological modeling in a data scarce watershed in north-central Portugal. *Geoderma* 264, 350–362.
- Wang, Y., Anderson, K., Suddaby, R., 2015. Updated source code for calculating fire danger indices in the Canadian Forest Fire Weather Index System. Technical Report. Canadian Forest Service. Northern Forestry Center 2015, Edmonton.
- Watanabe, K., Yamamoto, T., Yamada, T., Sakuratani, T., Nawata, E., Noichana, C., Sributta, A., Higuchi, H., 2004. Changes in seasonal evapotranspiration, soil water content, and crop coefficients in sugarcane, cassava, and maize fields in Northeast Thailand. *Agric. Water Manage.* 67, 133–143.
- Zhang, B., Liu, Y., Xu, D., Zhao, N., Lei, B., Rosa, R.D., Paredes, P., Paço, T.a., Pereira, L.S., 2013. The dual crop coefficient approach to estimate and partitioning evapotranspiration of the winter wheat-summer maize crop sequence in North China Plain. *Irrig. Sci.* 31, 1303–1316.

This research provides an understanding of changes in the energy balance and ET_a , with its components over an extended region in the north-central part of Portugal. An existing STSEB model was successfully applied for partitioning ET_a into transpiration and evaporation. To my knowledge, in Häusler et al. (2018) (Chapter 3) it was the first time that the remote sensing based STSEB model was tested for partitioning ET_a , using medium-spatial resolution satellite imagery (e.g. in contrast Ortega-Farías et al. (2016) used remote sensing data from drone overflights for partitioning). A good agreement between model estimates and measured energy heat fluxes (R_n , G , H , LE), and accordingly daily ET_a were obtained. Sánchez et al. (2016) applied the STSEB model with a set of three thermal-infrared radiometers at a vineyard, but obtained rather large underestimations for transpiration. In Häusler et al. (2018) the model was improved implementing the use of the beta-factor correction presented by Van Niel et al. (2011) with a RMSE of $< 1.5 \text{ mm day}^{-1}$ for both evaporation and transpiration. Furthermore, the STSEB model was able to obtain refined estimates for stress conditions that fit the estimates from on-site measurements. To date, the bias of ET_a , and its components between measured and estimated values are suitable for environmental studies, but are still too large for irrigation scheduling. This might be corrected by improving the retrieval for soil and vegetation temperatures and the use of new satellite products with higher spatial and temporal resolution e.g. Sentinel 2 with a spatial resolution of 10 m and a temporal coverage of about three days.

By applying an energy balance model combined with satellite observations, new insights about the energy balance fluxes over extended forested areas in Portugal, were given. The partitioning of ET_a showed that evaporation and transpiration from unburnt areas contributed with 20% and 80%, respectively. These results extend and improve previous ones that investigated the water cycle after disturbances of forest plantations. It showed that the effect of fire events on ET_a in eucalypt stands was rather small in the north-central part of Portugal and that it depended on fire severity (e.g. eucalypt stands in Australia, Nolan et al., 2015). While disturbances to the water cycle result in a change of the micro-climate and the stream-flow, this study suggests no significant changes in daily ET_a after the second year of the fire event, regardless of the burn severity. Thus, the return to the previous ET_a of water is completed after a few years, which has a corresponding influence to the groundwater and the water flow of rivers. In the scope of this work at the Caramulo mountain range the STSEB model additionally gave evidence of continuous transpiration of the eucalypt trees along the year despite the shallow soil depth. It suggests that the trees are able to penetrate "cracks" of the bedrock that give access to further water sources. However, other authors assumed that the eucalypt tree, after depleting the soil moisture, has no access to possible groundwater, reasoned by the relatively impermeable bedrock of the study area (Nunes et al., 2016). In order to consolidate the results of a fast recovery to pre-fire conditions in terms of ET_a , it would be necessary to observe a longer time-series. In addition, to retrieve absolute values instead of making a comparison between burnt and unburnt stand, on-site measurements of ET_a and its components with e.g. mini-lysimeters, sap-flow measurements should be carried out in a future work. The assumption that the eucalypt trees at the Caramulo mountain range have access to water sources other than the soil water

content, will be investigated in a follow-up study. For that, the K_s of eucalypt trees at the study site will be obtained to estimate when the soil water content should be depleted. By reaching the PWP the trees should have no further access to water, starting to wilt and die.

Observing the estimated daily ET_a before fire outbreaks did not provide predictive ability regarding wildfires occurrences by itself, but was successfully implemented into drought indices that were useful to identify areas that showed higher proneness to fires. The drought indices, KBDI and DC, are based on a simple water balance where the only water loss is evapotranspiration estimated from empirical equations of ET_o . By replacing the evapotranspiration with the estimated ET_a from STSEB, the water balance estimation improved in terms of absolute values for KBDI and DC. Both indices improved in terms of their spatial resolution of SMD estimation by using MODIS satellite imagery derived from the STSEB ET_a . In addition, with the coefficient approaches (K_{cb} and $K_{c,adj}$), it was possible to continue ET_a estimation for days without satellite data on a pixel-by-pixel scale.

Within the framework of this thesis, the application of the STSEB model to improve fire danger rating by implementing ET_a into the simple water balance assumptions of KBDI and DC, was most promising. The modified drought indices will be tested for other regions and climates. First encouraging results were achieved for the Palangkaraya drained forest in Indonesia. Areas which burned in September 2015 demonstrated to dry up faster than the surrounding areas with higher KBDI and DC values already in August 2015 (see Appendix D.2). The estimate of SMD from KBDI and DC can be further improved by applying a more sophisticated technique to obtain a threshold to identify fire-prone areas with higher accuracy. With the development of computing power and the emergence of new satellites with higher spatial and temporal resolution, the application of remote sensing based models is becoming increasingly attractive. In a future work the incorporation of rainfall products with a pixel-wise resolution instead of interpolation techniques over large areas will be tested. Image classification methods might also be helpful for better vegetation height estimations. The implementation of the STSEB model for ET_a estimation into fire danger rating routines would help to adapt forest and fire management, support fire fighters to prioritize certain areas, and prepare the population that lives in endangered areas.

References

- Allen, R. G., Pereira, L. S., Raes, D., and Smith, M. (1998). FAO Irrigation and Drainage Paper No. 56, Crop Evapotranspiration (guidelines for computing crop water requirements). *Geophysics*, 156:1–178.
- Amazirh, A., Merlin, O., Er-Raki, S., Gao, Q., Rivalland, V., Malbeteau, Y., Khabba, S., and Escorihuela, M. J. (2018). Retrieving surface soil moisture at high spatio-temporal resolution from a synergy between Sentinel-1 radar and Landsat thermal data: A study case over bare soil. *Rem. Sen. Environ.*, 211(March):321–337.
- Baldocchi, D. D. and Ryu, Y. (2011). A Synthesis of Forest Evaporation Fluxes - from Days to Years - as Measured with Eddy Covariance. In Levia, D., Carlyle-Moses, D., and T., T., editors, *Forest Hydrology and Biogeochemistry*, chapter 5, pages 101–116. Springer Science and Business Media B. V.
- Benyon, R. G. and Doody, T. M. (2015). Comparison of interception, forest floor evaporation and transpiration in *Pinus radiata* and *Eucalyptus globulus* plantations. *Hydrol. Proc.*, 29(6):1173–1187.
- Bisquert, M., Sánchez, J., and Caselles, V. (2014). Modeling Fire Danger in Galicia and Asturias (Spain) from MODIS Images. *Rem. Sen.*, 6(1):540–554.
- Bond-Lamberty, B., Peckham, S. D., Gower, S. T., and Ewers, B. E. (2009). Effects of fire on regional evapotranspiration in the central Canadian boreal forest. *Glob. Chang. Biol.*, 15(5):1242–1254.
- Brocca, L., Morbidelli, R., Melone, F., and Moramarco, T. (2007). Soil moisture spatial variability in experimental areas of central Italy. *J. Hydrol.*, 333(2-4):356–373.
- Carlson, T. T. N., Riziley, D. A., and Ji, J. (2007). An Overview of the "Triangle Method" for Estimating Surface Evapotranspiration and Soil Moisture from Satellite Imagery. *Sensors*, 7(8):1612–1629.
- Choudhury, B. J., Idso, S. B., and Reginato, R. J. (1987). Analysis of an empirical model for soil heat flux under a growing wheat crop for estimating evaporation by an infrared-temperature based energy balance equation. *Agr. For. Meteorol.*, 39(4):283–297.
- Chuvieco, E., Cocero, D., Riaño, D., Martín, P., Martínez-Vega, J., de la Riva, J., and Pérez, F. (2004). Combining NDVI and surface temperature for the estimation of live fuel moisture content in forest fire danger rating. *Rem. Sen. Environ.*, 92(3):322–331.
- Colaizzi, P. D., Agam, N., Tolk, J. A., Evett, S. R., Howell, T. A., Gowda, P. H., O’Shaughnessy, S. A., Kustas, W. P., and Anderson, M. C. (2014). Two-Source Energy Balance Model to Calculate E, T, and ET: Comparison of Priestley-Taylor and Penman-Monteith Formulations and Two Time Scaling Methods. *Trans. ASABE*, 57(2):479–498.

- Colaizzi, P. D., Agam, N., Tolk, J. A., Evett, S. R., Howell, T. A., O’Shaughnessy, S. A., Gowda, P. H., Kustas, W. P., and Anderson, M. C. (2016). Advances in a Two-Source Energy Balance Model: Partitioning of Evaporation and Transpiration for Cotton. *Trans. ASABE*, 59(1):181–197.
- Conceição, N., Tezza, L., Häusler, M., Lourenço, S., Pacheco, C. A., and Ferreira, M. I. (2017). Three years of monitoring evapotranspiration components and crop and stress coefficients in a deficit irrigated intensive olive orchard. *Agric. Water Manage.*, 191:138–152.
- Cristóbal, J., Prakash, A., Anderson, M. C., Kustas, W. P., Euskirchen, E. S., and Kane, D. L. (2017). Estimation of surface energy fluxes in the Arctic tundra using the remote sensing thermal-based Two-Source Energy Balance model. *Hydrol. Earth Syst. Sci.*, 21(June):1339–1358.
- David, J. S., Henriques, M. O., David, T. S., Tomé, J., and Ledger, D. C. (1994). Clearcutting effects on streamflow in coppiced Eucalyptus globulus stands in Portugal. *J. Hydrol.*, 162(1-2):143–154.
- David, T. S., Ferreira, M. I., David, J. S., and Pereira, J. S. (1997). Transpiration from a mature Eucalyptus globulus plantation in Portugal during a spring-summer period of progressively higher water deficit. *Oecologia*, 110(2):153–159.
- Ferreira, M. I., Valancogne, C., Daudet, F. a., Ameglio, T., Pacheco, C. a., and Michaelsen, J. (1996). Evapotranspiration and crop-water relations in a peach orchard. In *Evapotranspiration and irrigation scheduling*, pages 61–68, San Antonio, Texas. Proceed. of Int. Conf.
- Foken, T., Aubinet, M., and Leuning, R. (2012). The Eddy Covariance Method. In Aubinet, M., Vesala, T., and Papale, D., editors, *Eddy Covariance: A Practical Guide to Measurement and Data Analysis*, chapter 1, pages 1–19. Springer Science and Business Media B. V.
- Gentine, P., Entekhabi, D., Chehbouni, A., Boulet, G., and Duchemin, B. (2007). Analysis of evaporative fraction diurnal behaviour. *Agric. For. Manage.*, 143(1-2):13–29.
- Granier, A. (1985). Une nouvelle méthode pour la mesure du flux de sève brute dans le tronc des arbres. *Annales des Sciences Forestières*, 42(2):193–200.
- Green, S., McNaughton, K., and Clothier, B. (1989). Observations of night-time water use in kiwifruit vines and apple trees. *Agr. For. Meteorol.*, 48(3-4):251–261.
- Häusler, M., Conceição, N., Tezza, L., Sánchez, J. M., Campagnolo, M. L., Häusler, A. J., Silva, J. M., Warneke, T., Heygster, G., and Ferreira, M. I. (2018). Estimation and partitioning of actual daily evapotranspiration at an intensive olive grove using the STSEB model based on remote sensing. *Agr. Water Manage.*, 201:188–198.
- Hawtree, D., Nunes, J. P., Keizer, J. J., Jacinto, R., Santos, J., Rial-Rivas, M. E., Boulet, A. K., Tavares-Wahren, F., and Feger, K. H. (2015). Time series analysis of the long-term hydrologic impacts of afforestation in the Águeda watershed of north-central Portugal. *Hydrol. Earth Syst. Sci.*, 19(7):3033–3045.
- Hitt, N. P. (2003). Immediate Effects of Wildfire on Stream Temperature. *J. of Freshwater Ecology*, 18(1):171–173.
- Hugalde, I. P. and Vila, H. (2014). Isohydic or Anisohydic Behaviour in Grapevine. . . a Never-Ending Controversy? *Revista de Investigaciones Agropecuarias*, 40(1):4–10.

- Kalma, J. D., McVicar, T. R., and McCabe, M. F. (2008). Estimating Land Surface Evaporation: A Review of Methods Using Remotely Sensed Surface Temperature Data. *Surveys in Geophysics*, 29(4-5):421–469.
- Kang, S., Kimball, J. S., and Running, S. W. (2006). Simulating effects of fire disturbance and climate change on boreal forest productivity and evapotranspiration. *Sci. Total Environ.*, 362(1-3):85–102.
- Kasim, A. A. and Usman, A. A. (2016). Triangle Method for Estimating Soil Surface Wetness from Satellite Imagery in Allahabad District, Uttar Pradesh, India. *J. Geosci. and Environ. Prot.*, 04(01):84–92.
- Keetch, J. J. and Byram, G. M. (1968). A Drought Index for Forest Fire Control. Technical report, U.S. Department of Agriculture - Forest Service, Asheville, North Carolina.
- Kustas, W. P. and Norman, J. M. (1999). Evaluation of soil and vegetation heat flux predictions using a simple two-source model with radiometric temperatures for partial canopy cover. *Agr. For. Meteorol.*, 94:13–29.
- Langford, K. J. (1976). Change in yield of water following a bushfire in a forest of eucalyptus regnans. *J. Hydrol.*, 29(1-2):87–114.
- Mitchell, P. J., Veneklaas, E., Lambers, H., and Burgess, S. S. (2009). Partitioning of evapotranspiration in a semi-arid eucalypt woodland in south-western Australia. *Agr. For. Meteorol.*, 149(1):25–37.
- Mohanty, B. P., Cosh, M. H., Lakshmi, V., and Montzka, C. (2017). Soil Moisture Remote Sensing: State-of-the-Science. *Vadose Zone Journal*, 16(1):0.
- Monteith, J. (1994). The Balance of Water - Present and Future. In Keane, T., Daly, E., editor, *Proc. AGMET Group (Ireland) and Agric. Group of the Royal Meteorol. Soc. (UK)*, pages 29–45, Dublin. Trinity College Dublin.
- Monteith, J. L. (1965). Evaporation and environment. In *The state and movement of water in living organisms*, volume 19, pages 205–234. Cambridge University Press.
- Monteith, J. L. (1981). Evaporation and surface temperature. *Quart. J. R. Met. Soc.*, 107:1–27.
- Montes-Helu, M. C., Kolb, T., Dore, S., Sullivan, B., Hart, S. C., Koch, G., and Hungate, B. A. (2009). Persistent effects of fire-induced vegetation change on energy partitioning and evapotranspiration in ponderosa pine forests. *Agr. For. Meteorol.*, 149(3-4):491–500.
- Nolan, R. H., Lane, P. N. J., Benyon, R. G., Bradstock, R. a., and Mitchell, P. J. (2014). Changes in evapotranspiration following wildfire in resprouting eucalypt forests. *Ecohydrol.*, 7(5):1363–1377.
- Nolan, R. H., Lane, P. N. J., Benyon, R. G., Bradstock, R. A., and Mitchell, P. J. (2015). Trends in evapotranspiration and streamflow following wildfire in resprouting eucalypt forests. *J. Hydrol.*, 524:614–624.
- Norman, J. M., Kustas, W., and Humes, K. (1995). A two-source approach for estimating soil and vegetation energy fluxes from observations of directional radiometric surface temperature. *Agr. For. Meteorol.*, 77:263–293.

- Nunes, J. P., Malvar, M., Benali, A. A., Rial Rivas, M. E., and Keizer, J. J. (2016). A simple water balance model adapted for soil water repellency: Application on Portuguese burned and unburned eucalypt stands. *Hydrol. Processes*, 30(3):463–478.
- Ortega-Farías, S., Ortega-Salazar, S., Poblete, T., Kilic, A., Allen, R., Poblete-Echeverría, C., Ahumada-Orellana, L., Zuñiga, M., and Sepúlveda, D. (2016). Estimation of Energy Balance Components over a Drip-Irrigated Olive Orchard Using Thermal and Multispectral Cameras Placed on a Helicopter-Based Unmanned Aerial Vehicle (UAV). *Rem. Sen.*, 8(8):638.
- Pereira de Almeida, A. and Riekerk, H. (1990). Water balance of Eucalyptus globulus and Quercus suber forest stands in south Portugal. *For. Ecol. Manage.*, 38(1-2):55–64.
- Prats, S. A., Malvar, M. C., Vieira, D. C. S., MacDonald, L., and Keizer, J. J. (2013). Effectiveness of Hydromulching to Reduce Runoff and Erosion in a Recently Burnt Pine Plantation in Central Portugal. *Land Degradation & Development*, 27(5):1319–1333.
- Qi, Y., Dennison, P. E., Spencer, J., and Riano, D. (2012). Monitoring Live Fuel Moisture Using Soil Moisture and Remote Sensing Proxies. *Fire Ecology*, 8(3):71–87.
- Raju, P. D. and Neelima, G. (2012). Image Segmentation by using Histogram Thresholding. *IJCSET*, 2(1):776–779.
- Roberts, J. (1983). Forest transpiration: A conservative hydrological process? *J. Hydrol.*, 66(1-4):133–141.
- Sanchez (2008). Merging micro-meteorology and Landsat imagery to monitor daily evapotranspiration at a regional scale. *Tethys, Journal of Weather and Climate of the Western Mediterranean*, 5:37–46.
- Sánchez, J., de la Cruz, F., Martínez, L., Montoro, A., and López-Urrea, R. (2016). Testing the potential of two-source surface energy balance to monitor plant transpiration in vineyards. *Acta Hort.*, 1112(1112):187–192.
- Sánchez, J., Scavone, G., Caselles, V., Valor, E., Copertino, V., and Telesca, V. (2008a). Monitoring daily evapotranspiration at a regional scale from Landsat-TM and ETM+ data: Application to the Basilicata region. *J. Hydrol.*, 351(1-2):58–70.
- Sánchez, J. M., Bisquert, M., Rubio, E., and Caselles, V. (2015). Impact of Land Cover Change Induced by a Fire Event on the Surface Energy Fluxes Derived from Remote Sensing. *Rem. Sen.*, 7(11):14899–14915.
- Sánchez, J. M., Caselles, V., Niclòs, R., Coll, C., and Kustas, W. P. (2009). Estimating energy balance fluxes above a boreal forest from radiometric temperature observations. *Agr. For. Meteorol.*, 149(6-7):1037–1049.
- Sánchez, J. M., Kustas, W. P., Caselles, V., and Anderson, M. C. (2008b). Modelling surface energy fluxes over maize using a two-source patch model and radiometric soil and canopy temperature observations. *Rem. Sen. Env.*, 112(3):1130–1143.
- Sánchez, J. M., López-Urrea, R., Rubio, E., and Caselles, V. (2011). Determining water use of sorghum from two-source energy balance and radiometric temperatures. *Hydrol. Earth Syst. Sci.*, 15(10):3061–3070.

- Scotland, R. M. (1955). The Measurement of Wind Velocity by Sonic Means. *J. Meteorol.*, 12(4):386–390.
- Scott, R. L., James Shuttleworth, W., Goodrich, D. C., and Maddock, T. (2000). The water use of two dominant vegetation communities in a semiarid riparian ecosystem. *Agr. For. Meteorol.*, 105(1-3):241–256.
- Seguin, B., Becker, F., Phulpin, T., Gu, X., Guyot, G., Kerr, Y., King, C., Lagouarde, J., Ottlé, C., Stoll, M., Tabbagh, A., and Vidal, A. (1999). IRSUTE: A Minisatellite Project for Land Surface Heat Flux Estimation from Field to Regional Scale. *Rem. Sen. Env.*, 68(3):357–369.
- Shakesby, R. A., Coelho, C. D. O. A., Ferreira, A. D., Terry, J. P., and Walsh, R. P. D. (1993). Wildfire Impacts on Soil Erosion and Hydrology in Wet Mediterranean Forest, Portugal. *Int. J. Wildland Fire*, 3(2):95–110.
- Shuttleworth, W. J. and Wallace, J. S. (1985). Evaporation from sparse crops-an energy combination theory. *The Quarterly J. of the Royal Meteorol. Soc.*, 111(465):839–855.
- Silva, J. M., Feith, H., and Pereira, J. (2007). Exploração e silvicultura pós-fogo em eucaliptais. In Alves, A. M., Pereira, J. S., Silva, J. M. N., editor, *O Eucaliptal em Portugal: Impactes Ambientais e Investigação Científica*, chapter 9, pages 285–312. ISAPress, Lisbon, Portugal.
- Spracklen, D. V., Arnold, S. R., and Taylor, C. M. (2012). Observations of increased tropical rainfall preceded by air passage over forests. *Nature*, 489(7415):282–285.
- Staley, D. M., Negri, J. A., Kean, J. W., Laber, J. L., Tillery, A. C., and Youberg, A. M. (2017). Prediction of spatially explicit rainfall intensity–duration thresholds for post-fire debris-flow generation in the western United States. *Geomorphology*, 278:149–162.
- Sun, X., Onda, Y., Otsuki, K., Kato, H., Gomi, T., and Liu, X. (2017). Change in evapotranspiration partitioning after thinning in a Japanese cypress plantation. *Trees*, 31(5):1411–1421.
- Suomi, V. (1957). Sonic Anemometer Measurement of Atmospheric Turbulence. In Lettau, H. H. and Davidson, B., editors, *Exploring the atmosphere's first mile*, pages 256–266. Pergamon Press, London, New York.
- Testi, L. and Villalobos, F. J. (2009). New approach for measuring low sap velocities in trees. *Agric. For. Meteorol.*, 149(3-4):730–734.
- Thornthwaite, C. W. (1948). An Approach toward a Rational Classification of Climate. *Geographical Review*, 38(1):55–94.
- Torres, F. T. P., Romeiro, J. M. N., Santos, A. C. d. A., de Oliveira Neto, R. R., Lima, G. S., and Zanuncio, J. C. (2018). Fire danger index efficiency as a function of fuel moisture and fire behavior. *Sci. Total Environ.*, 631-632:1304–1310.
- Van der Ent, R. J., Savenije, H. H. G., Schaeffli, B., and Steele-Dunne, S. C. (2010). Origin and fate of atmospheric moisture over continents. *Water Resour. Res.*, 46(9):1–12.
- Van Niel, T. G., McVicar, T. R., Roderick, M. L., van Dijk, A. I. J. M., Renzullo, L. J., and van Gorsel, E. (2011). Correcting for systematic error in satellite-derived latent heat flux due to assumptions in temporal scaling: Assessment from flux tower observations. *J. Hydrol.*, 409(1-2):140–148.

- Van Wagner, C. E. (1974). Structure of the Canadian Forest Fire Weather Index. Technical report, Department of the Environment, Ottawa, USA.
- Watson, F. G. R., Vertessy, R. A., McMahon, T. A., Rhodes, B. G., and Watson, I. S. (1999). The hydrologic impacts of forestry on the Maroondah catchments. Technical Report 99/1, Cooperative Research Centre For Catchment Hydrology, Clayton, Vic.
- Whelan, A., Starr, G., Staudhammer, C. L., Loescher, H. W., and Mitchell, R. J. (2015). Effects of drought and prescribed fire on energy exchange in longleaf pine ecosystems. *Ecosphere*, 6(7):art128–art128.
- Wilson, K. B., Hanson, P. J., Mulholland, P. J., Baldocchi, D. D., and Wullschleger, S. D. (2001). A comparison of methods for determining forest evapotranspiration and its components : sap-flow , soil water budget , eddy covariance and catchment water balance. *Agr. For. Meteorol.*, 106:153–168.
- Yang, Y., Guan, H., Long, D., Liu, B., Qin, G., Qin, J., and Batelaan, O. (2015). Estimation of surface soil moisture from thermal infrared remote sensing using an improved trapezoid method. *Rem. Sen.*, 7(7):8250–8270.
- Zhan, X., Kustas, W. P., and Humes, K. S. (1996). An Intercomparison Study on Models of Sensible Heat Flux over Partial Canopy Surfaces with Remotely Sensed Surface Temperature. *Rem. Sen. Environ.*, 58(3):242–256.

Model assessment over grassland

Since April 2014, an eddy covariance (EC) system over grassland is operating, which consists of a 12 m tall tower, located at the sub-urban area of Aveiro, Portugal (40°36'51.07"N, -8°39'05.90"W, Datum WGS84). A three dimensional sonic anemometer (Windmaster Pro, Gill Instruments, Lymington, UK) was installed, directly measuring the three components of wind speed and virtual temperature. The instrument allows to calculate beside T_a and u , also the energy heat flux densities of H and LE . For the instrumentation details please consider Chapter 4.

Measurements of H and LE taken at the eddy covariance tower were also compared to the estimates from the STSEB model during satellite overpass. H and LE were determined with R^2 of 0.80 and 0.61, respectively. Generally, H was mostly underestimated with RMSE of ± 50 and MAE of 40 W m^{-2} , and LE was rather overestimated as the residual of the energy balance equation. The RMSE and MAE resulted in $\pm 90 \text{ W m}^{-2}$ in both cases. The EC measurements also provided daily values for H , LE , and ET_a , which were compared to the estimates given by the model (Table A.1). For H_d , the RSME was ± 40 and the MAE 30 W m^{-2} , being mostly underestimated, while a RSME of ± 50 and a MAE of 50 W m^{-2} for daily LE_d was obtained. Comparing observations with the estimations of ET_a , the RSME was ± 1.4 , and the MAE 1.2 mm d^{-1} . Differences between measured and estimated daily ET_a ranged between 0.1 and 1.5 mm d^{-1} , with the exception of 29 August 2015 with an overestimation of 2.5 mm d^{-1} . The absolute values are given in Table A.1.

Table A.1: Operability test of the STSEB model by comparing estimates with measurements of daily H , LE and ET_a at the EC tower. The left columns show the measured values; the right columns show the estimated ones from the STSEB model. EC measurements have only been available since the year 2014. All Landsat 8 images were acquired for satellite path 204 and row 34 for only cloudless days.

Date	H_d		LE_d		ET_a	
	(W m ⁻²)		(W m ⁻²)		(mm d ⁻¹)	
9 July 2014	70	50	77	105	2.7	3.7
29 October 2014	9	3	-	50	-	1.8
6 March 2015	17	6	40	64	1.4	2.2
25 May 2015	58	43	70	104	2.5	3.7
28 July 2015	115	87	30	76	1.1	2.6
29 August 2015	98	40	24	90	0.9	3.2
30 September 2015	40	13	40	48	1.6	1.7
MAE	24		36		1.2	
RMSE	28		41		1.4	

Note that the estimates of ET_a over grassland served to test the operability of the STSEB model, but cannot account for a robust validation since no on-site measurements over eucalypt stands were available. The STSEB model has already been successfully tested over different types of vegetation (Sanchez (2008); Sánchez et al. (2011)) in combination with remotely sensed data and an accuracy of

$\pm 1.0 \text{ mm d}^{-1}$. In our study the differences between measured and estimated ET_a over grassland were within an acceptable range (between 0.1 to 1.5 mm d^{-1} ; Table A.1), with the exception of one observation day (29 August 2015, 2.3 mm d^{-1}). To partly account for this uncertainty no absolute values of ET_a over *Eucalyptus* were evaluated, but only the difference between burnt and unburnt sites. Generally, surface energy flux models, yielding around 50 W m^{-2} , are considered to be acceptable for surface energy modelling according to Seguin et al. (1999) and Kalma et al. (2008). This statement is also conform with our results for instantaneous and daily energy heat fluxes, with the exception of LE at the time of satellite overpass. The discrepancy between observed and estimated values was larger compared to other studies. In Cristóbal et al. (2017) H and LE showed RMSE values between $\pm 38 \text{ W m}^{-2}$ to $\pm 46 \text{ W m}^{-2}$. They recently applied a two-source energy balance model over Arctic tundra in Alaska, comparing model results to EC measurements. Ortega-Farías et al. (2016) used a two-source algorithm to estimate the components of the energy balance over a drip-irrigated olive orchard. LE and H were estimated with a RMSE of $\pm 50 \text{ W m}^{-2}$ and $\pm 56 \text{ W m}^{-2}$, and a MAE of 43 W m^{-2} and 46 W m^{-2} , respectively. Two different versions of the TSEB model were applied to a heterogeneous advective environment in China by Song et al. (2016). Their findings coincide with ours, showing larger discrepancies between observed EC measurements and estimated values. For H the RMSE was between $\pm 56 \text{ W m}^{-2}$ and $\pm 79 \text{ W m}^{-2}$, while the RMSE for LE ranged from $\pm 52 \text{ W m}^{-2}$ and $\pm 87 \text{ W m}^{-2}$, depending on the version of the model. In this study H was mostly underestimated, leading to an overestimation of LE as the residual of the energy balance equation. This was also observed by (Sanchez, 2008), who applied the STSEB model over corn, resulting in a RMSE of $\pm 24 \text{ W m}^{-2}$ for H and $\pm 48 \text{ W m}^{-2}$ for LE .

Influence of tree height

The impact of average tree (th) and shrub height (sh), being input variables for the STSEB model to estimate ET_a , was tested as there was no information of follow-up treatments after fire events e.g. forest clearing that would have altered the average heights.

Thus, a sensitivity analysis at burnt and unburnt eucalypt stands close to Aveiro at the Caramulo mountain range was applied, using Landsat data (Chapter 4) and MODIS data (Chapter 5). All variables used for the STSEB model were fixed. Only the tree heights changed from 0.1 m to 18.0 m with small steps at the beginning (0.01 to 2.0 m with a step-size of about 30 cm), followed by one meter steps up to 5.0 m tree height, and after that alterations of two meters from 10.0 to 18.0 m. All tree heights were simulated with shrub heights of 0.01, 0.1, 0.3, 0.7 and 1.0 m.

The absolute percentage error (PE) for different scenarios for one to four years after the fire and also for the different fire severity degrees (moderate and high severity burns) was obtained, where PE is given in Equation B.1, taking the average for the specific year and fire severity.

The Percentage Error was calculated as:

$$PE(\%) = 100 \times \frac{ET_{a,small} - ET_{a,tall}}{ET_{a,small}} \quad (B.1)$$

where $ET_{a,small}$ is the lower vegetation height (small = smaller height) and $ET_{a,tall}$ is the upper canopy height (tall = taller height) different (i.e. taller) to $ET_{a,small}$.

For each step in shrub height at the unburnt areas, the changes in ET_a are smaller than 0.1 mm d^{-1} , when tree height is smaller than 1 m, on average. With increasing tree height, the influence of shrub height converges to zero (regularly less than 0.04 mm d^{-1} in ET_a , with trees taller than 5 m, on average). Evaluating the influence of the vegetation height for moderate and high severity fire event cases, the impact is much higher (Table B.1). Nevertheless, one should keep in mind that the increase of average canopy height of several meters was most probably not the case of high severity cases at the study site, and can be excluded for the moderate to low severity cases.

Table B.1: Example of worst case scenario about one month after the fire event. Here, a control area with tree height of 14.0 m and a shrub height of 1.0 m was assumed. The burnt sites' average tree height was proposed to be 1.0 m with a ground cover of 0.1 m.

Year	Burn severity	PE (%)
2012	moderate	12.6
2012	high	22.5
2013	moderate	18.0
2013	high	22.4

Generally, the sensitivity analysis showed that the largest differences occur for small trees (<1 m) with short ground-cover, and shortly after the fire up to one year. With increasing tree height (taller than

2 m) the difference becomes $<5\%$ for each step of 1 m, when shrub height does not change (e.g. shrub height is 0.3 m for 2 and 3 m height trees), and becomes insignificantly low when trees are higher than 5 m, on average (e.g. shrub height 0.1 and 0.7 m for tree heights of 5 m and 10 m, respectively result in an absolute difference of ET_a of less than 5%).

Additionally, the influence of different tree and shrub heights was also tested, using MODIS satellite data. In Table B.2 different scenarios are given, supporting the findings for the burnt stands. The worst scenario (Comb.1) gives an PE of 22%; the greater the difference between the tree and/or the shrub heights the larger the error. Nevertheless, the PE is only about 10% for large differences between average canopy and ground cover heights, and about 1-2% for 1-2 m differences in tree height, regardless of the shrub height.

Table B.2: Different combinations (Comb.) of tree (ht) and shrub heights (hs) and their absolute difference in Percentage Error (PE)

Scenario	ht1	sh1	th2	sh2	PE (%)
Comb. 1	0.0	0.01	18.0	0.3	22.0
Comb. 2	0.3	0.01	5.0	0.3	13.2
Comb. 3	0.3	0.01	14.0	0.3	18.1
Comb. 4	1.0	0.10	14.0	0.7	12.6
Comb. 5	1.0	0.10	18.0	1.0	12.9

In Silva et al. (2007) an extensive evaluation of tree mortality after fires is given, concerning eucalypt stands in Portugal, which would also alter the average canopy height. Generally, tree mortality after wildfires is dependent on tree age and rotation. Trees older than 5 years have a survival of more than 50% and trees older than 10 years more than 60%. Tree mortality increases with the rotation of the forest stand (second and third rotation up to 80%; Silva et al., 2007). In the case of the eucalypt tree, the bark usually protects the wood from the impact of the flames. After wildfires the burnt stands are usually exploited by the forest owners, as the logs might be still of economic interest after removing the bark of the burnt trees. In Portugal there are no selective cuts, leaving the trees that were unaffected by the fire, as the forest became irregular and for this reason more complicated to manage.

In our study (Chapter 4 and Chapter 5) the eucalypt trees were older than 8 years, where most stands were affected by low to moderate-low fire severity burns, indicating a rather high survival of the trees. However, tree stands were all in their second and third rotation, increasing the mortality of the trees. For this study it was assumed that the average tree height of most stands was probably unaffected, as the probability of mortality of the trees was rather small, concerning the burn severity classifications and the tree age of the stands. In 2016, all stands, inclusively reference forest stands were burned, leaving no opportunity for on-site exploration. Nevertheless, the sensitivity analysis concerning tree height indicated a rather small influence to the output (i.e. ET_a) in case of a change in average canopy height.

Estimation of the water stress coefficient of *E. globulus*

In literature there was no water stress coefficient (K_s) for eucalypt stands found. The K_s describes the effect of soil water stress. In dry soils the water is strongly bound by capillary and absorptive forces, which means that the potential energy of the water drops below a certain threshold. Thus, the water extraction becomes more difficult for the plant and results in water stress. To estimate ET_a under non-standard conditions the K_s is multiplied by the K_c and ET_o (Eq. C.1; Allen et al., 1998):

$$ET_a = K_c K_s ET_o \quad (C.1)$$

Several authors that investigated the water balance at the Caramulo mountain range assume no access to water resources after soil water depletion. This assumption was investigated by determining the possible period of time, in which the soil water content would be exhausted, which would have the wilting of the plant as consequence. Using the average field capacity (FC), permanent wilting point (PWP) and soil depth (Z_r) from on-site measurements, the total available soil water (TAW) in the rooting zone was obtained by:

$$TAW = 1000(\theta_{FC} - \theta_{WP})Z_r \quad (C.2)$$

where θ_{FC} is the water content at field capacity ($m^3 m^{-3}$), θ_{WP} is the water content at wilting point ($m^3 m^{-3}$), and Z_r is the soil depth (m). The absolute values are reported in Chapter 5.

The water, which is available without reduction in ET_a , is called readily available water (RAW) and is determined as follows:

$$RAW = p \times TAW \quad (C.3)$$

where p is the average fraction of TAW . Here, we assumed p to be 0.7 (see also fruit trees in Allen et al., 1998). The average measured values for TAW (60.8 mm) and RAW (42.6 mm) at the Caramulo mountain range were used.

Example 1: As a first approach to estimate K_s we assumed following conditions: the daily ET_o is 6 mm d^{-1} , the K_c is 1, resulting in a daily ET_c of 6 mm d^{-1} (see Table C.1). The K_s was obtained by:

$$K_s = \frac{TAW - \sum ET_a}{TAW - RAW}; \text{ for } ET_a > RAW \quad (C.4)$$

Applying Eq. C.4 with the upper assumptions given in Table C.1, the trees start to suffer from water stress on the 8th day, when the sum of the soil water consumption is higher than RAW ($>42.6 \text{ mm}$). In this example for the Caramulo mountain range the soil water content would be depleted after 19 days, when the water consumption is equal or higher than TAW (60.8 mm). Then, the permanent wilting point would have been reached, meaning the plant/tree is starting to dry up and die.

Table C.1:

Day	ET_o mm d ⁻¹	K_c	ET_c mm d ⁻¹	$\sum ET_a$ mm d ⁻¹	ET_a mm d ⁻¹	K_s	$\sum ET_a (K_s)$ mm d ⁻¹
1	6	1	6	6	6	1.0	6
2	6	1	6	12	6	1.0	12
3	6	1	6	18	6	1.0	18
4	6	1	6	24	6	1.0	24
5	6	1	6	30	6	1.0	30
6	6	1	6	36	6	1.0	36
7	6	1	6	42	6	1.0	42
8	6	1	6	48	4.2	0.7	46.2
9	6	1	6	50.4	3.6	0.6	49.8
10	6	1	6	53.4	2.4	0.4	52.2
11	6	1	6	54.7	2.0	0.3	54.2
12	6	1	6	56.2	1.5	0.3	55.7
13	6	1	6	57.2	1.2	0.2	56.9
14	6	1	6	58.1	0.9	0.2	57.8
15	6	1	6	58.7	0.7	0.1	58.5
16	6	1	6	59.2	0.5	0.1	59.0
17	6	1	6	59.5	0.4	0.1	59.4
18	6	1	6	59.8	0.3	0.1	59.7
19	6	1	6	60.1	0.2	0.0	60.0

Example 2: In David et al. (1997) the stomatal conductance (g_s) and transpiration in eucalypt stands were measured, which can also be used to obtain the water stress coefficient (K_s) as follows:

$$K_s = \frac{Tr}{Tr_{\max}} \quad (C.5)$$

where Tr is the transpiration of a certain day (mm d⁻¹) and Tr_{\max} is the maximum transpiration (mm d⁻¹) under standard conditions e.g. no water stress.

Table C.2: Transpiration and stomatal conductance are closely related to each other; therefore stomata closure is also related to the available soil water content. DoY stands for Day of the Year, g_s is the stomatal conductance, Tr is the measured transpiration at the forest stand, Tr_{rel} is the relative transpiration.

DoY	g_s	Tr (mm d ⁻¹)	Tr_{rel} (mm d ⁻¹)
146	0.35	3.1	1.00
159	0.27	3.2	1.03
167	0.19	2.2	0.69
181	0.14	2.0	0.63
188	0.12	1.5	0.47
208	0.09	1.3	0.41
216	0.07	0.8	0.25
Min	-	0.5	0.16

The Figures C.1a, C1.b, and C1.c show the relationships between Tr and g_s , Tr_{rel} and g_s , and K_s with Day of the Year (DoY), respectively, retrieved from on-site measurements at eucalypt stands taken by David et al. (1997). These relationships are dependent on the biophysical properties of the plant species and the local meteorological conditions.

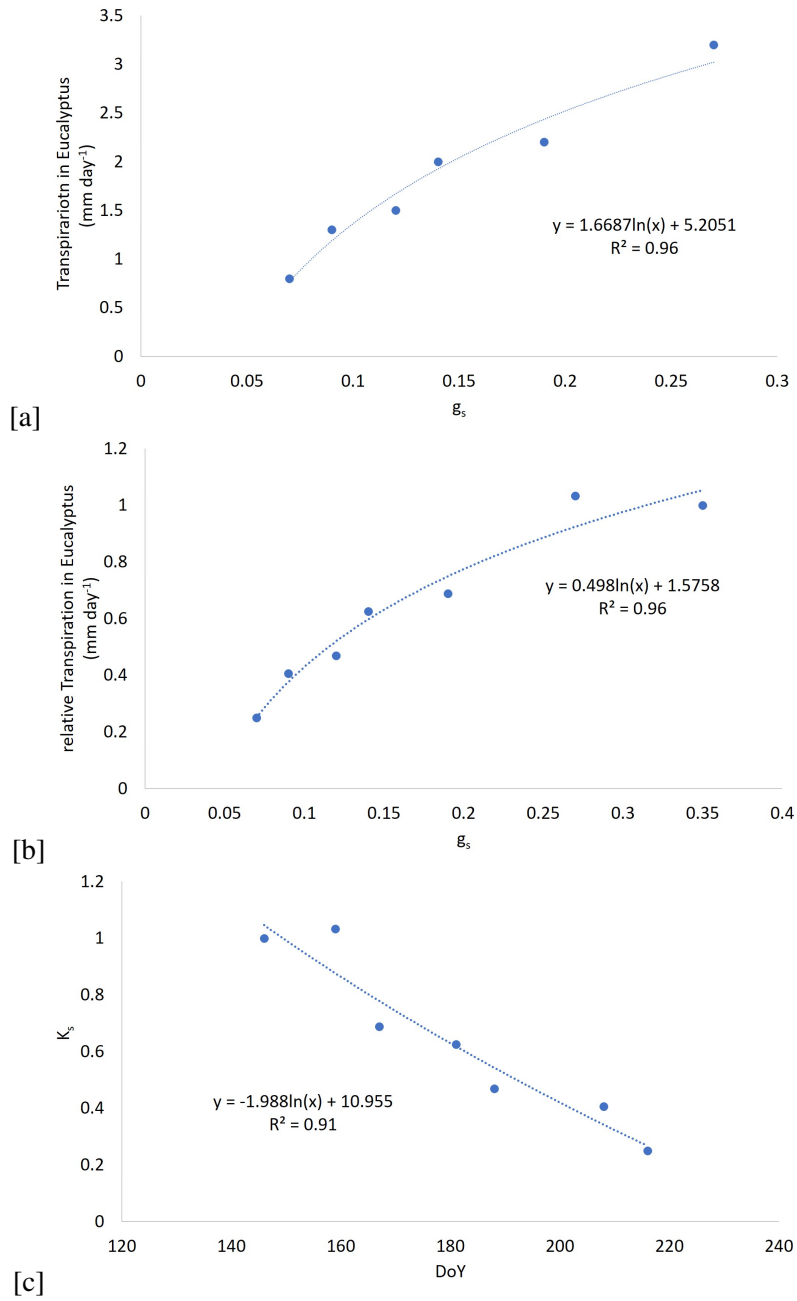


Figure C.1: Fig. C.1a shows the relationship between transpiration and stomatal conductance, Fig. C.1b demonstrates the relationship between relative transpiration and stomatal conductance and Fig. C.1c gives the relationship between K_s and the Day of the Year (DoY).

At the end of the cycle, when the soil is dry, it is assumed that transpiration is basically equal to ET_a . In this special case, the relative transpiration is the reduction in ET_a of the vegetation, and can be treated as equivalent of K_s . Having a good relationship between K_s and DoY ($R^2 = 0.91$) we suggest, in absence of on-site measurements that for similar local conditions this relationship is useful as an operational tool to estimate the K_s for *Eucalyptus* at other locations.

Classifier retrieval at the example of Indonesia

Classifier retrieval for the case study in Portugal:

In Chapter 5, a segmented histogram approach (Raju and Neelima, 2012) was applied to delimit fire-prone areas from areas with less fire danger. Hereby, an initial threshold S_i (here mean value) was selected, segmenting the image into two groups. Group 1 included all pixels defined as fire-prone $>S_i$ and group 2 incorporated the ones classified as fire-save $\leq S_i$. Then, the mean values of group 1 and 2 were computed and a new threshold found by:

$$S_i = \frac{Mean1 + Mean2}{2} \quad (D.1)$$

The new threshold from Eq. D.1 was applied and the procedure iterated till the difference of S_i was insignificant small (e.g. variation smaller than 0.1 for the fire danger index). This procedure is called basic global thresholding and results in a bimodal histogram that partitions the image into two groups.

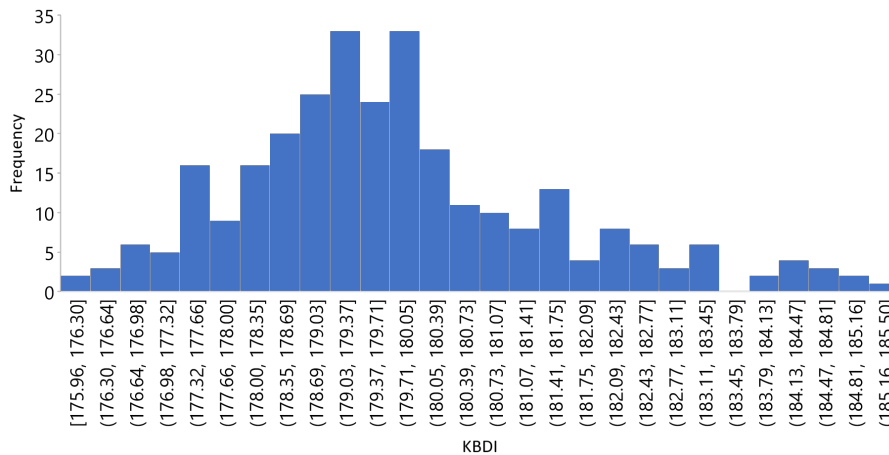


Figure D.1: Example of segmented bimodal histogram to classify the areas into their proneness to fire. Here 3 July 2015 is given, where the minimum between the two maximums represents the initial threshold. Five images were classified and the average taken to obtain the average threshold of 60.6%.

As the value ranges differ for each day, the threshold was expressed in percentage. In total, five images were used to obtain an average threshold of 60.6% and applied for the other days. The result for KBDI and DC in Portugal are reported in Chapter 5.

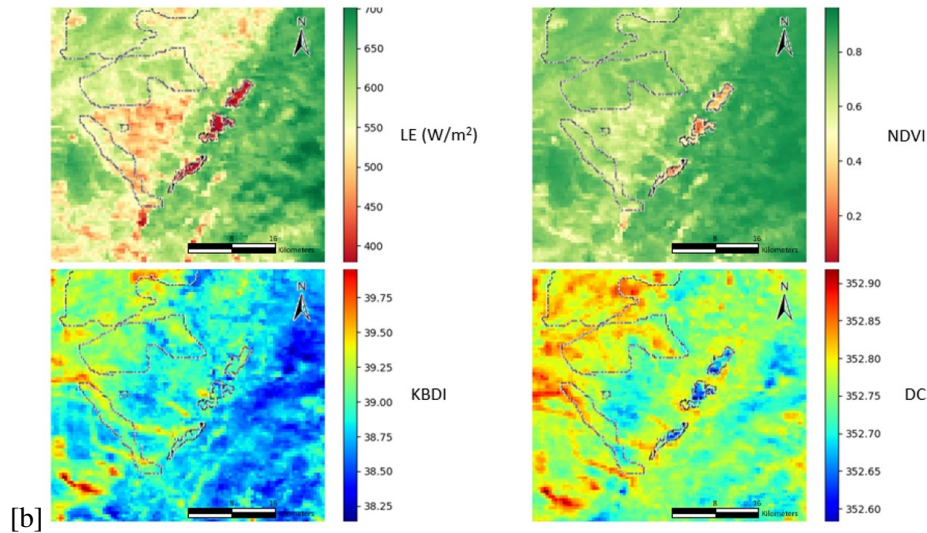
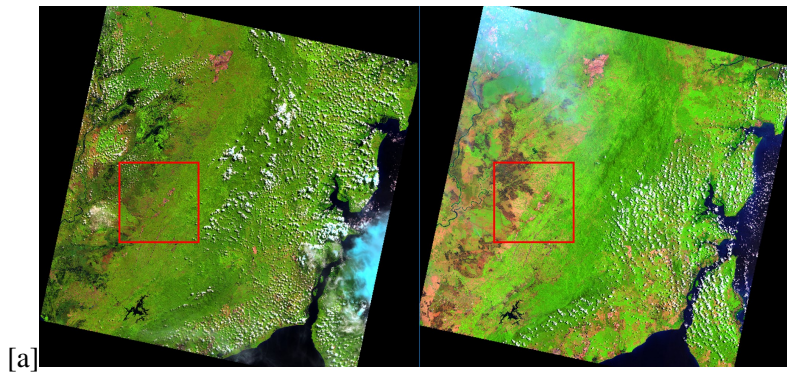


Figure D.2: Image (a) shows false color images (Landsat 8) from before (24 May 2015) and after (16 September 2015) the fire over Central Kalimantan, Indonesia. Image (b) compares the Latent heat (LE), $NDVI$, $KBDI$ and DC with each other from the 16 August 2015 (one months before the wildfires) with the borders of the fire scars later in the year.

Example Indonesia:

The same approach was applied for the Palangkaraya drained forest, Indonesia. Meteorological data was provided by Takashi Hirano (Hokkaido University, Japan) from the station at Palangkaraya listed at the Asia Flux Net with the following results.

Figure D.2a shows false color images from MODIS satellite data taken over Central Kalimantan, Indonesia on the 16 September 2015. In Figure D.2b a comparison between LE , $NDVI$, $KBDI$ and DC is given for the 16 August 2015, one month before the actual wildfires occurred, where fire scars are represented by dashed lines. The areas which were later affected by fires demonstrated lower values for $KBDI$ and DC , indicating a higher SMD. As mentioned in Chapter 5 the SMD is related to fuel moisture, thus, to fire danger. In the cases of LE and $NDVI$ the higher SMD did not show significant changes around this area.